ANA SOFIA DOS SANTOS CONCEIÇÃO

STUDY AND DEVELOPMENT OF A NEW ELECTRON MULTIPLIER: GEM-MIGAS

UNIVERSITY OF COIMBRA

2012

ANA SOFIA DOS SANTOS CONCEIÇÃO

Study and Development of a new electron multiplier: GEM-MIGAS

Dissertation submitted to
Faculdade de Ciências e Tecnologia da Universidade de Coimbra for the degree of Phylosophiae Doctor in Technological Physics

under the supervision of

Prof. Dr. Joaquim Marques Ferreira dos Santos and Dr. Jamil A. Mir

in collaboration with

Rutherford Appleton Laboratory, United Kingdom

UNIVERSITY OF COIMBRA

2012

This PhD work was supported by Fundação para a Ciência e Tecnologia, trough the grant SFRH/BD/ 42195/2007.

Acknowledgements

The pathway is travelled in the presence of several people, which in one way or another, are very important to its accomplishment.

I would like to thanks Professor Joaquim for the supervisor of this work and all the support along this year.

I am also special grateful to Doctor Jamil A. Mir for the timely supply of experimental material as well as the availability along the last four years on discussion of several questions.

To Professor Jorge Maia I want to acknowledge the scientific and experimental background exchanged during this work.

I would like to thanks Doctor Luis Panchorrinha for the revision of this thesis as well as the support demonstrating along this period.

I could not forget the support of all the people from the laboratory, particularly Liliana Carita, Andrea Gouvea, Alexandre Trindade, Augusto Cordeiro, Artur Coimbra, Carlos Carvalho, Fernando Amaro Pedro Neves, Sergio do Carmo, for the good moments spent specially at the cards break.

Finally, my recognitions go to my family which was always there for me. A great part of this achievement is product of them.

Aos meus Pais

Study and development of a new Electron Multiplier: GEM-MIGAS.

Ana Sofia dos Santos Conceição

Abstract

The concept of gas counter was introduced by Geiger in 1908. The first prototypes used wires to define the electrical field in the different detector regions, trough the application of voltage gradients.

Over the years a lot of effort was put in the development of gas detectors in order to overcome some of the wire limitations. In 1988 the microstrip gas chamber was introduced and has shown a better performance than precedent detectors: high rate capability, excellent localization and good granularity. These are some of the characteristics that make them attractive for applications such as charged particle tracking at high luminosity colliders.

The use of printed circuit board technology made possible the development of microstructures, avoiding the subtract degradation under continued irradiation. The microstructures turned out to be a more reliable and cheaper solution, an advantage to exploit new applications.

The Gas Electron Multiplier (GEM) and Micromegas are promising examples developed under the microstructure concept. They have been extensively studied over the years for many applications. The Gas Electron Multiplier with a Micro–Induction Gap Amplifying Structure (GEM-MIGAS), recently proposed by J. A. Mir, is a hybrid structure of a GEM coupled to a Micromegas induction gap, i.e. a GEM having a short induction gap from few tens to 300 μm.

The development study and investigation of the GEM-MIGAS microstructure is the objective of this dissertation. As starting point, a three-dimensional electric field simulation based on the element finite method was performed for the GEM-MIGAS detector, in order to determine the electric field profile in the different regions. The GEM-MIGAS performance, concerning charge gain and energy resolution, was investigated for an Ar/CH_4 (90%/10%) gas mixture, pure CH_4 and pure Ar using a 5.9 keV X-rays. This study was done for a conventional GEM-MIGAS with the induction gap set to 50 μm.

In further studies the gap thickness was extended to values between 50 and 300 μm. Using the single electron response method, the GEM-MIGAS charge gain was determined for a He/iso-C_4H_{10} (85/15%) mixture, as a function of the induction region thickness.

The ion back-flow was evaluated for the GEM-MIGAS microstructure with induction regions in the range 50-300 μm. For this study the GEM-MIGAS was coupled to a semitransparent CsI-photocathode and operated in Ar/5%CH4 gas mixture at atmospheric pressure.

Finally, the GEM-MIGAS viability to neutron detection was investigated by determining its gain capability at elevated gas pressures using pure CF_4 and He/ CF_4 mixtures. The gain was determined as a function of the induction region thickness (20 to 300 μm) using a standard GEM (50 μm hole diameter) for several CF_4 pressures. Being also investigated the influence of the GEM hole diameter on gain at various CF_4 pressures. Then the best configuration concerning the GEM hole diameter and the induction region thickness was used for the charge gain measurements in a He/ CF_4 mixture.

Estudo e desenvolvimento de um novo multiplicador de electrões: GEM-MIGAS

Ana Sofia dos Santos Conceição

Resumo

O conceito de detector gasoso foi introduzido por Geiger em 1908. O primeiro protótipo foi desenvolvido com base na aplicação de uma diferença de potencial a um fio metálico, permitindo definir o campo eléctrico nas diferentes regiões do detector.

Ao longo dos anos houve grande investimento no desenvolvimento de detectores gasosos de modo a ultrapassar as limitações apresentadas pelos modelos baseados em fios. Em 1988 surge a camara gasosa de microfitas evidenciando melhor performance que os detectores precedentes, como por exemplo alta taxa de contagem e excelente capacidade de localização.

No entanto, a camara gasosa de microfitas revelou problemas de degradação do substrato aquando exposição prolongada à radiação. A utilização da tecnologia de placa de circuito impresso possibilitou o desenvolvimento das microestruturas, evitando o problema de degradação do substrato. Assim, as microestruturas tornaram-se uma solução mais fiável e economicamente viável, permitindo explorar novas áreas de aplicação.

O *Gas Electron Multiplier* (GEM) e a *Micromegas* são exemplos de microestruturas, bastante utilizadas ao longo dos anos em diversas aplicações. O Gas Electron Multiplier with a Micro–Induction Gap Amplifying Structure (GEM-MIGAS) proposto por J. A. Mir apresenta-se como uma estrutura hibrida que resulta da combinação de um GEM com uma Micromegas através de uma região de indução que varia entre 20 a 300μm

O objectivo desta dissertação baseia-se no estudo e desenvolvimento da microestrutura GEM-MIGAS. Nesse sentido, foi inicialmente desenvolvido um modelo electromagnético 3D utilizando o método de elementos finitos para estudar o perfil do campo eléctrico nas diferentes regiões da estrutura. A performance do ganho e resolução em energia da estrutura GEM-MIGAS foi avaliada em CH_4 e Ar puros e numa mistura gasosa Ar/CH_4 (90%/10%) usando raios X de 5.9keV. Este estudo foi realizado para a estrutura convencional, caracterizada por uma região de indução de 50 μm

A seguinte etapa passou pela avaliação da espessura da região de indução para valores entre 50 e 300 μm. Nesse sentido foi utilizado o método de resposta por electrão único para a determinação do ganho em carga em função da espessura numa mistura He/iso-C_4H_{10} (85/15%).

O fenómeno de refluxo de iões da estrutura GEM-MIGAS foi estudado para regiões de indução entre 50 e 300 μm, utilizando um fotocátodo semitransparente de iodeto de césio a operar em Ar/5%CH4 à pressão atmosférica.

Por último, foi analisada a possibilidade de aplicação da estrutura GEM-MIGAS na detecção de neutrões, determinando para o efeito as características do ganho em carga para diferentes pressões de CF_4 puro e para uma mistura de He/CF_4. O ganho foi determinado em função da região de indução (20 a 300 μm) usando um GEM convencional (50 μm de diâmetro do orifício). Sendo também investigada a influencia do diâmetro do orifício no ganho para diferentes pressões de CF_4.

Contents

Abstract I
Resumo III
Micropatern Gas Detectors 1
1.1 Brief History of Gaseous Detectors 1
1.2 Multi-Wire Proportional Chamber 2
1.3 Microstrip Gas Counter 4
1.4 Micromegas 5
1.4.1 Bulk Micromegas 7
1.5 Gas Electron Multiplier 9
1.5.1 Structure 9
1.5.2 GEM performance 12
1.5.3 Aplications 17
1.6 GEM-MIGAS 17
1.6.1 Origin & Structure 18
1.6.2 Preliminary studies 19
1.6.3 Road Map 24
Gas Detector Physics 25
2.1 Interaction of ionising radiation with matter 25
2.1.1 Interaction of charged particles with matter 26
2.1.3 Interaction of Neutrons with matter 35
2.2 Charge Transport in Gases 36
2.2.1 Filling Gas 37
2.2.2 Diffusion 39
2.2.3 Drift 41
2.3 Gas Amplification 45
2.3.1 Operation Regimes 47
Electric Field Simulation 50
3.1 The Model 50
3.2 Electric field strength 51
3.2.1 50 μm Induction region gap 51
3.2.2 100 μm Induction region gap 53
3.2.3 200 μm Induction region gap 54
3.2.4 250 μm Induction region gap 55
3.2.5 300 μm Induction region gap 56
3.2.6 Synthesis 57
3.3 Electric Field Map 58
3.4 Conclusions 62
GEM-MIGAS operation in Argon-Methane mixtures 63

4.1 Introduction 63
4.2 Experimental Setup 64
4.2.1 Electronic Calibration 66
4.3 Experimental Results 68
4.3.1 Charge Gain 68
4.2.2 Energy Resolution 72
4.4 Conclusions 75
GEM-MIGAS with different gaps 76
5.1 Introduction 76
5.2 Experimental Setup 77
5.3 Results 78
5.4 Summary 82
The Ion Back-Flow Measurements 83
6.1 Introduction 83
6.2 Experimental Setup 84
6.3 Charge Gain 86
6.3.1. 50 μm Induction region Gap 86
6.3.2 100 μm Induction region Gap 87
6.3.3 200 μm Induction region Gap 89
6.3.4. 250 μm Induction region Gap 90
6.3.5. 300 μm Induction region Gap 90
6.3.6 Summary 91
6.4 Ion back-flow results 93
6.4.1 50 μm Induction region Gap 93
6.4.2 100 μm Induction region Gap 94
6.4.3 200 μm Induction region Gap 95
6.4.4 250 μm Induction region Gap 97
6.4.6 Summary 98
6.5 Conclusions 102
GEM-MIGAS for Neutron Detection 103
7.1 Introduction 103
7.2 Experimental Setup 108
7.3 Optimization of GEM-MIGAS induction region gap 109
7.3.1 250 μm Induction region Gap 109
7.3.2 150 μm Induction region Gap 112
7.3.3 50 μm Induction region Gap 114
7.3.4 30 μm Induction region Gap 117
7.3.5 20 μm Induction region Gap 119
7.4 Influence of the GEM Parameters 123

7.4.1 GEM 40 123
7.5 Measurements with He-CF_4 mixtures 128
7.6 Conclusions 130
THICKGEM-MIGAS 131
8.1 Introduction 131
8.2 Experimental Setup 133
8.3 Results 134
8.3.1 50 μm Induction region Gap 134
8.3.2 250 μm Induction region Gap 135
8.4 Conclusions 136
Conclusions 137
9. References 139

Chapter 1

Micropatern Gas Detectors

The use of gas counters for radiation detection was introduced in 1908 by Geiger in Rutherford's laboratory. Geiger found out that, when radiation was stopped in the counter a current flowed through the electrodes and could be detectable with an electrometer of moderate sensibility.

The classic gas counter consists of two electrodes, cathode and anode, between which a potential difference is applied. When the ionizing radiation interacts with the gas, a part or the full amount of its energy is dissipated by generating electron-ion pairs. The electrons and ions created by the radiation interaction move under the influence of the electric field in opposite directions, electrons go to the anode while ions move to the cathode. The charge flow induces a current that can be measured and, through appropriate electronics, a pulse can be obtained and the interactions counted individually.

Gas detectors were subject of many research studies leading to considerable progress and improvement on this field. A brief description about gas detector development will be done.

1.1 Brief History of Gaseous Detectors

The first gas counter prototypes were based on wires, for example the Proportional Counter (PC) and Multi-Wire Proportion Chamber (MWPC). In these types of detectors the charge multiplication take place near the wires, were the electric field is very strong. The PC was introduced in the late 1940s and has been widely used for measurements of energy loss by radiation. However, the PC space localization capability is limited to the information of particle passing through the counter volume or not. To overcome this limitation a stack of many independent counters was implemented, which resulted in the Multi Wire Proportional Chambers (MWPC) development.

A second generation of gas detectors emerged after a few years, where the wires were replaced by strips, the Microstrip Chamber [4]. The new devices are produced by means of the photolithography technique, a procedure commonly used to fabricate masks for integrated circuits, enabling the production of very precise thin strip structures, in the micrometer range. In this type of devices, the gas amplification takes place at a low voltage difference compared to wire based detectors.

Innovative detector designs have been developed, with encouraging performances and higher reliability, and gave origin to a new family of gas detectors: Micro Pattern Gas Detectors [6]. Their name is due to the fact that the elementary cells are at least one order of magnitude smaller than the ones of the precedent detectors. Examples of this kind of detectors are the Micro-Dot Avalanche Chamber, Micro-Groove Detector, Micro-Wire Detector and Micro-Gap Chamber. The most advanced micro pattern detectors are the MicroMegas and the Gas Electron Multiplier (GEM), which are the subject of research for this thesis.

The micropattern gaseous detectors have a better performance than the classic MWPC. The combination of excellent position resolution, high counting rate capability and good granularity make them very attractive detectors for particle tracking in high luminosity colliders, as well as in other fields, like medical x-ray imaging applications, neutron imaging, x-ray polarimetry, UV and single photon detection.

All the micropattern detectors suffer from the appearance of discharges during their operation when the total avalanche charge exceeds the Rather limit, which is between 10^7 and 10^8 electron-ion pairs [66]. The electric field in front and behind the avalanche is increased locally and this induces the fast growth of a filament like streamer.

Recently, a millimetre-size pixilation detector was developed, Thick GEM-like (TGEM) [58], based on the GEM concept. The TGEM is manufactured with standard PCB technology by precise drilling and Cu etching, of double-face Cu-clad G-10 plate.

A description of the Multi-wire Proportional Chamber, Microstrip Gas Counter, Micromegas and GEM will be done in this chapter, discussing with more detail the GEM and Micromegas properties, since those are the base of the device proposed for investigation in this thesis.

1.2 Multi-Wire Proportional Chamber

The Multi-Wire Proportional Chamber was introduced in 1968 by Charpak [3]. It's composed by a set of anode wires closely spaced, all at the same poten-

tial, and each wire acts as an independent proportional counter. For his invention Charpak was awarded the 1992 Nobel Prize in Physics. Figure 1. 1 shows a schematic of a MWPC. The MWPC consists essentially of a set of thin, parallel and equally spaced anode wires, symmetrically sandwiched between two cathode planes. For proper operation the gap, L, should be three or four times larger than the wire spacing, d. A negative voltage is applied to the cathodes, while the anodes are grounded. The electrons produced in the gas volume, by radiation or charged particles, drift towards the anode wires due to the electric field. A gas avalanche amplification takes place in the high electric field around the wires. The ions generated in this avalanche drift towards the cathodes. Unfortunately, the ions limit the counting rate capability of MWPC. For rates above~10^4/(s mm^2) the ions produce a high space charge around the wires reducing the electric field-strength and consequently the gain [6].

The position accuracy in a multi wire proportional chamber is determined by the anode wire spacing: less than 1 mm is difficult to operate [5]. The spatial resolution, σ_x, can be calculated as $\sigma_x = d/\sqrt{12}$, where d is the distance between two wires. The typical spatial resolution is about 300 μm for a spacing of 1mm. The upper limit for the resolution is given by the wire spacing, which cannot be reduced arbitrarily, due to the electrostatic repulsion of the wires. As result, the chamber has limitations in granularity.

The possibility to determine the position of an incoming particle using only one detector instead of arrays of proportional counters is the main objective of technologic development.

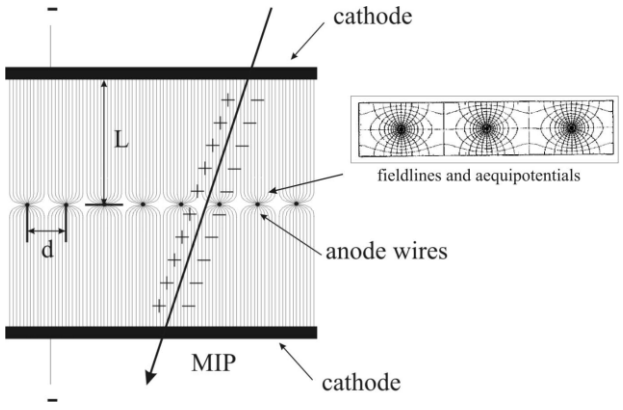

Figure 1. 1- Multi-wire Proportional Chamber and the field map around the wires [5].

The MWPC has undergone continuous improvements over the years, where different prototypes of MWPC have been developed, such as the drift chamber, time projection chamber, time expansion chamber and ring imaging chambers. Multi-wire devices of various designs remain a major task in high energy physics.

1.3 Microstrip Gas Counter

The Microstrip Gas Counter (MSGC) was introduced by Oed in 1988 as a first approach to the Micro Pattern Detectors [4], the wires being replaced by small metal strips engraved on a thin isolating substrate. The MSGC is produced trough photolithography technology. The anodes, smaller strips with a width of some microns, are located between the cathodes, larger strips, with a typical pitch of 100 µm. This corresponds to a reduction on the electrode thickness by one order of magnitude when compared to the MWPC. The insulating substrate is usually made of glass with a diamond coating and the strips are made of gold or chromium. A schematic view of MSGC is depicted in Figure 1. 2.

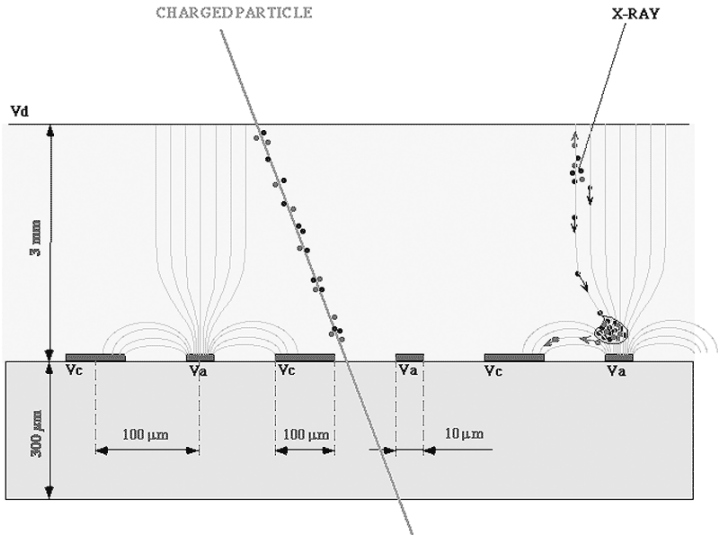

Figure 1. 2 - Schematic view of the Microstrip Gas Counter. Typical dimensions are indicated together with the electric field lines [5].

The electrons resulting from radiation interactions with the gas drift to the microstrip plane experiencing avalanche amplification due to the strong electric field around the anodes. The electrons are collected on the anodes while the ions are collected by the cathodes. However, the ions can reach the substrate surface during their flow, being practically fixed there due to the extremely reduced ion mobility on insulators. As a consequence the insulator surface will be charged until the applied electric field redress it.

The MSGC was presented as an alternative to the MWPC in order to overcome some of its limitations. In a MWPC the ions from the avalanche multiplication have to drift a long way to the cathode, typically a few mm. In the MSGC they drift to the closest cathode, typically 50µm. Therefore, the MSGC can reach higher count rates before the detector performance starts to suffer from space

charge effects. This also results in faster signals and a better time resolution. The spatial resolution is also better, since the strips are at a smaller distance compared to the wires. The electric field configuration of a MSGC is also advantageous for the energy resolution, having a better performance compared to the MWP C.

One of the disadvantages of the MSGC is the difficulty to cover large areas, which can be overcame using several microstrip planes together, as was done in physic experiments like HERMES[7] and HERA-B [7].

One limitation of the MSGC is the fact that the avalanche multiplication does not exceed 10^4, due to breakdown of the insulator surface. The positive ions created during the avalanche process and accumulated on the insulator, modify locally the electric field and cause a drop of the gain in the irradiated area of the detector. The poor stability resulting from the surface charge caused by stucked ions can be minimized using a conducting substrate or special treatment of the surface. However, the conductivity can not be very high otherwise there will be currents flowing from the anode to the cathode, which can compromise the detector operation. The development of a glass with the right electronic conductivity, good mechanical and chemical properties, was studied by several groups.

Systematic laboratory research revealed two fundamental degradation sources that affect the MSGC performance, polymer growth and discharges [7]. The polymer growth in the gas, under sustained avalanches, results in insulating layers deposited on electrodes, which affect the gain. From previous experience with wire chambers, this effect was expected to occur, but not with the swiftness and the degree of sensitivity to residual organic pollutants experimentally found. The occurrence of discharges during the operation is more crucial, often fatal for the structures. The discharge probability is voltage-dependent and largely enhanced by the exposure to high fluxes and heavy ionizing particles.

In order to overcome these problems and satisfy scientific needs a new generation of Micro Pattern Gas Detectors emerged, based on the working principles of the MSGC. Examples of this kind of detectors are the MicroMegas and the Gas Electron Multiplier (GEM), which have been the most successful.

1.4 Micromegas

The Micromegas, Micro Mesh Gaseous Structure, was introduced by Giomataris in 1996 [8]. It operates as a two stage parallel plate avalanche chamber, with a narrow amplification gap, defined between the anode and cathode

planes. The cathode is thin metallic micromesh made of Nickel, with a thickness of a few microns. The anode microelements (strips or pads) are printed on an insulator board. The cathode-anode distance, about 100 μm, is kept via small insulating pillars deposited by standard photographic methods on the anodes, covering a small part (~1%) of the surface. The amplification occurs between the mesh plane and the microstrip plane. Figure 1. 3 show a schematic view of the Micromegas. A study to optimize the detector geometrical parameters has shown the virtue of using narrow amplification gaps below 100 μm [9].

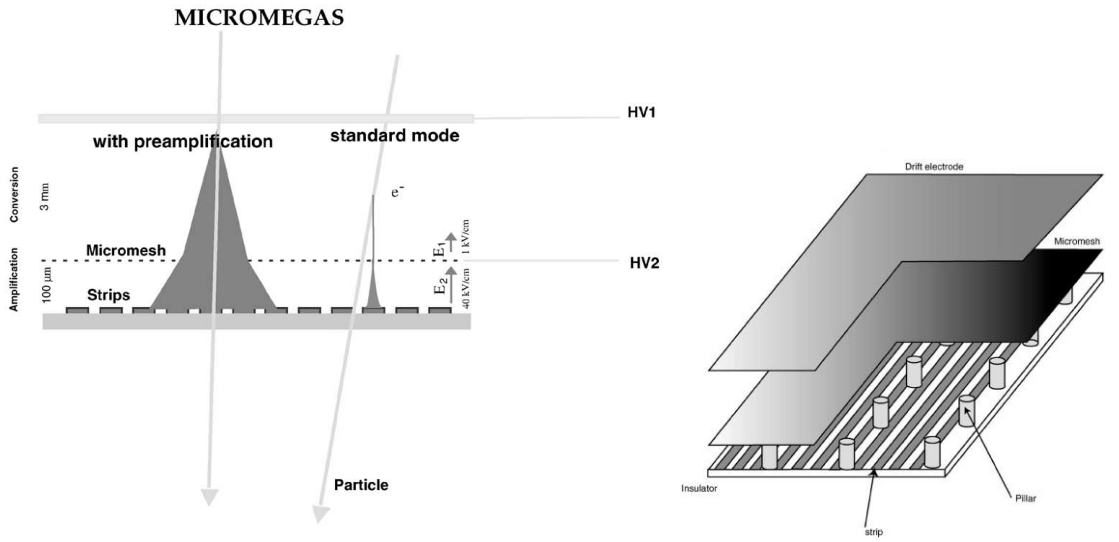

Figure 1. 3 - Micromegas [10].

In the majority of the applications, a third electrode is placed parallel to the mesh defining the drift region. The ionization electrons, created by energy deposition of an incident charged particle or radiation in the conversion gap, drift towards the cathode micromesh. The electrons reaching the mesh are then transferred to the amplification gap, between anodes and cathode, being multiplied through an avalanche process due to the high electric field in this region. The amplification inside the mesh holes is negligible. The electron cloud is collected by the anode microstrips, while the positive ions drift in the opposite direction and are collected by the micromesh. The charge signal is mainly due to positive ions drifting towards the micromesh electrode, which takes place typically within 100 ns, depending on the thickness of the amplification gap and on the gas mixture. However, the fast current signal is mainly due to the electrons given their high mobility, about 100 times faster than the ions [10].

The electric field has to be uniform in the conversion and amplification regions. However, the electric field shape is disturbed near the micromesh holes. The knowledge of the field lines near the micromesh is essential for the detector operation, concerning the efficiency of the electrons passage through the mi-

cromesh and the fast evacuation of the positive-ion. The Micromegas configuration is an advantage for the electric field ratio between the drift and the amplification region, which can be adjust to large values, as required for an optimal operation device. Such a high ratio is also required in order to capture the ions produced in the small amplification gap, reducing the fraction that escapes to the conversion region.

The Micromegas is a high gain gaseous detector, which can stand up alone without additional pre-amplification. As a result of the small gap and therefore high electric field, there is a fast collection time of ions, typically less than 100 ns [9]. This is an advantage to reduce the space charge effect that limits the gain at high counting rates, being measured high charge gain values, at rates beyond 10^6 particles/mm^2/s [8]. Studies in Ar-CH_4 (90/10%)at atmospheric pressure have shown gains close to 10^5, allowing single electron detection [8]. The Micromegas has been used in a large number of research experiments, as the COMPASS experiment, where the Micromegas was used for the up-stream tracking system [68].

1.4.1 Bulk Micromegas

The manufacture techniques used for the first generation of Micromegas impose some limitations to the size and shape of the detector. A collaboration between CERN and IRFU (Institute of Research into the Fundamental Laws of the Universe - CEA) developed new methods to simplify the production and thereby enlarge the scope of possible applications [67]. The effort was focused on producing an amplification region as a single piece, using the newly developed bulk and microbulk methods.

In bulk Micromegas a woven wire mesh is used instead of the usual electroformed micromesh. The anode plane carrying the copper strips, a photo resistive film having the right thickness and the cloth mesh, are laminated together at a high temperature, forming a single object. The photo resistive material is subsequently etched by photolithograph method, producing the pillars. In Figure 1. 4 a scheme of the fabrication procedure is show.

The pillars have a cylindrical shape of 300 μm diameter printed with a distance of 2 mm, as shown in Figure 1. 5. The first prototypes were characterized by an active area of 9x9 cm^2.

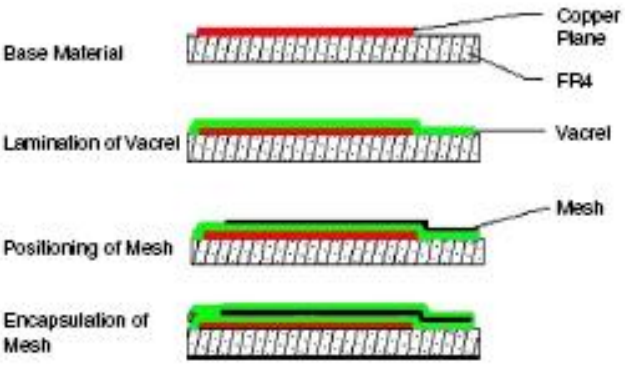

Figure 1. 4- Schematic of the fabrication procedure of the bulk Micromegas.

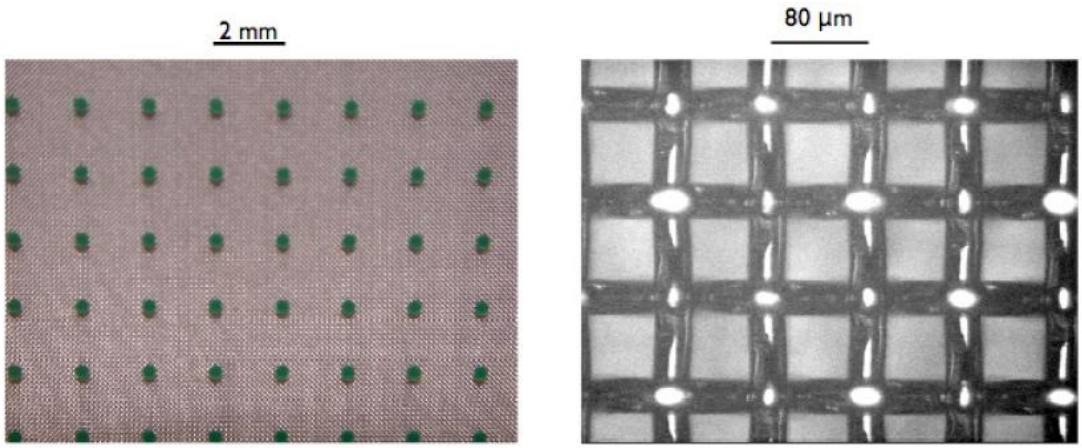

Figure 1. 5- Photographs of the bulk detector elements. The picture at left shows a small area of the detector; the 400 µm in diameter pillars every 2 mm are visible. On the right side is a microscopic view showing details of the woven wire mesh [67].

With this technique the micromesh can have a wide border at the edge, of a few milimiters, avoiding the need of an additional frame to support the micromesh. This semi-industrial assembly process allows the regular production of large, stable and inexpensive detector modules, in thin and flexible configurations. Such a bulk Micromegas is robust and can be made in a large single piece, up to areas of 50x50 cm^2.

Several applications have recently benefited from this technological development, such as the CAST (Cern Axion Solar Telescop) experiment where the two TPC detectors were replaced by two Micromegas detectors, obtaining remarkable results, excellent stability and an unprecedented background level («10^{-5}/keV/cm^2/s).

1.5 Gas Electron Multiplier

The Gas Electron Multiplier (GEM) was introduced by Sauli in 1996 as a charge pre-amplification structure in gas detectors [11]. The GEM consists of a kapton foil, metal-coated on each side and perforated by a high density of holes, typically 50 to 100 per mm^2 [19]. Under the application of a suitable voltage difference, each hole acts as an independent proportional counter. The electrons released in the gas, by ionizing radiation, drift into the holes where charge multiplication occurs in the high field inside the channels. Most of the electrons generated in the avalanches are collected in a passive electrode or are transferred to another amplifying device, a cascade configuration, where higher gains can be achieved.

1.5.1 Structure

The GEM is produced through conventional photo-lithographic methods used on multi-layer printed circuits [11]. The basic element is a 50 μm thick kapton foil, metal-clad on both sides with a 5 μm copper layer and perforated in a regular matrix of holes. The kapton foil is passivated with photoresist and exposed to light through a mask. After curing, the metal is patterned on both sides by wet etching, which serves as a self-alignment mask for the etching of the insulator in the open channels. The chemical etching produces double-conical shape holes with wider diameter in the entry sides, which improves the dielectric rigidity. The manufacture technology, developed by the CERN Surface Treatment Service can be easily extended to larger areas.

The GEM is characterized by the distance between the centers of two consecutive holes, the pitch, the hole diameter in the metal and the hole diameter in the kapton. The upper face is designed top and the down face is the bottom.

Figure 1. 6 shows an image of a typical GEM geometry: 5 μm thickness copper on a 50 μm kapton foil, 70 μm diameter holes in the metal, 55 μm diameter holes in the kapton and a pitch of 140 μm. A cut view obtained with an electronic microscope is shown in Figure 1. 7, illustrating the conical shape of the holes.

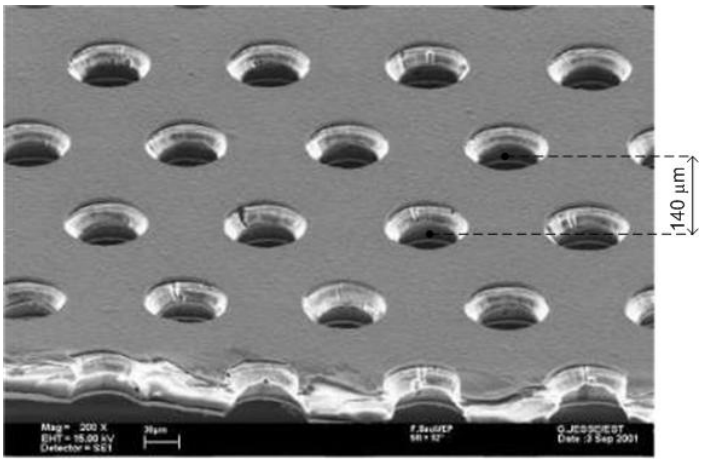

Figure 1. 6 – Image of a GEM electrode, etched on a metal-clad, 50 µm thick polymer foil. The hole's diameter and spacing distance are 70 µm and 140 µm, respectively [17].

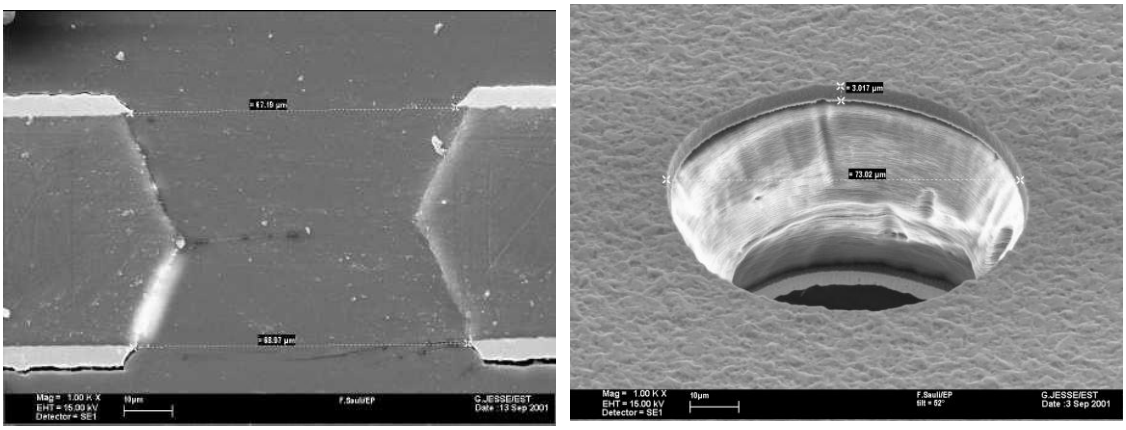

Figure 1. 7 - Cut view of a GEM obtained with an electronic microscope [17].

Several GEM grids, with different designs and geometries, were manufactured and tested [18] . Studies of gain for different geometries have shown that the maximum gain increases for narrower holes, as can be seen in the compilation of Figure 1. 8 [18], were different GEM geometries are characterized for a gas mixture of argon and carbon dioxide. The different geometries are indicated in the picture legend; for example the code A19 (140/95/60), A19 refers to the GEM model, 140 is the pitch, 95 the hole diameter in the metal and 60 the hole diameter in kapton, values in µm. Figure 1. 9 depicts the electric field profile for different hole diameters, where an electric field increase for narrower holes is evident [21]. Owing to the exponential dependence of the Townsend coefficient on the electric field, the proportional gain increases considerably as the hole size is reduced. However, for very narrow holes, a saturation effect appears, probably due to the loss of charges by diffusion.

The pitch does not influence the gain characteristics, but limits the drift field values and consequently the electron collection efficiency into the holes. The

hole diameter also affects the electron collection efficiency. The maximum voltage that can be safety reached is determined essentially by local defects and by the gas mixture, the geometry does not have a big influence.

In summary, the maximum achievable gain depends essentially on the kapton thickness, the hole diameter, the gas mixture and the applied voltage.

An important characteristic of the GEM is the optical transparency (OT), defined as the ratio between the open area (hole diameter in the kapton, D_k) and the total area of the GEM. OT can be calculated from Dk and Pitch (P) dimensions:

$$O.T = \frac{open\_area}{total\_area} = \frac{\pi}{2\sqrt{3}}\left(\frac{D_k}{P}\right)^2 \qquad (1.1)$$

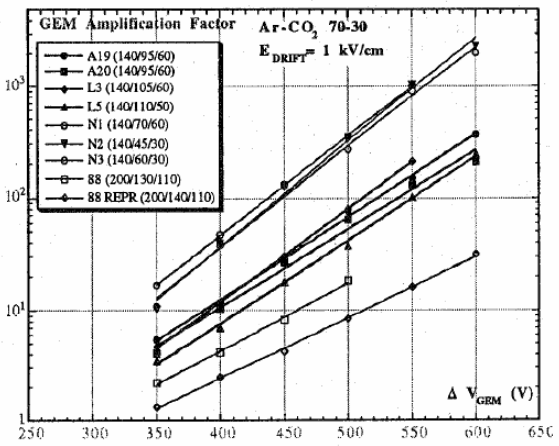

Figure 1.8- Compilation of gains factors for several GEM geometries [18].

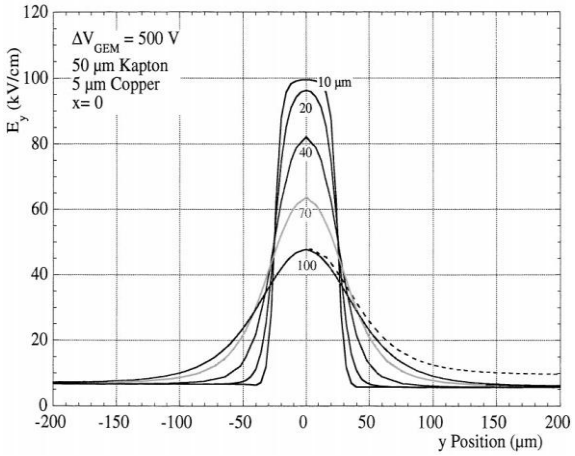

Figure 1.9 - Electric field computed along a line through the center of the holes, for different hole diameters [21].

1.5.2 GEM performance

The GEM is an amplification detector where the charge multiplication occurs inside the holes. Upon the application of a suitable voltage difference between the two copper electrodes, an electric field develops inside the GEM holes. The profile of the electric field and equipotential lines in the GEM holes is depicted in Figure 1. 10 [17]. The huge concentration of lines in the centre of the hole means that the electric field is very high there. The drift and the induction field transport the electrons trough and out of the holes, respectively.

The electrons released in drift region by ionizing radiation move along the field lines into the GEM-holes. Due to the high electric field the electrons acquire enough energy to ionize the gas thereby resulting in an avalanche of electrons. The majority of the avalanche electrons proceed to the lower region where they can be collected on a passive electrode or carry on to another multiplier device. Some of the avalanche electrons are lost to the GEM bottom electrode consequently the effective gain of the multiplier is lower than the total number of ions produced by a single electron.

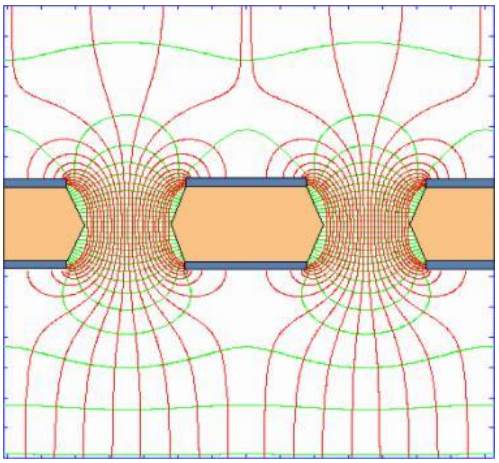

Figure 1. 10- Scheme of the electric field and equipotentials lines in the GEM upon application of a voltage difference between the two metal sides. [17].

The GEM can be operated in single mode or in a multiple configuration with several elements in cascade, Figure 1. 11 . In a single GEM configuration two different regions are identified, the drift and the induction regions. In the double-GEM configuration there is also the region between the two GEMs, called transfer region. The cascade configuration allows higher gain performance compared to the single GEM, the gain enhancement is related with the number of multiplier elements.

A unique feature of GEM detectors is that charge multiplication and charge collection take place in separate electrodes, which is an advantage to prevent

the propagation of accidental discharges to the sensitive electronics. The signal induced on the readout board are only due to electron collection, without tails due to the slow component of ions, as in other gas detectors, and therefore are very fast.

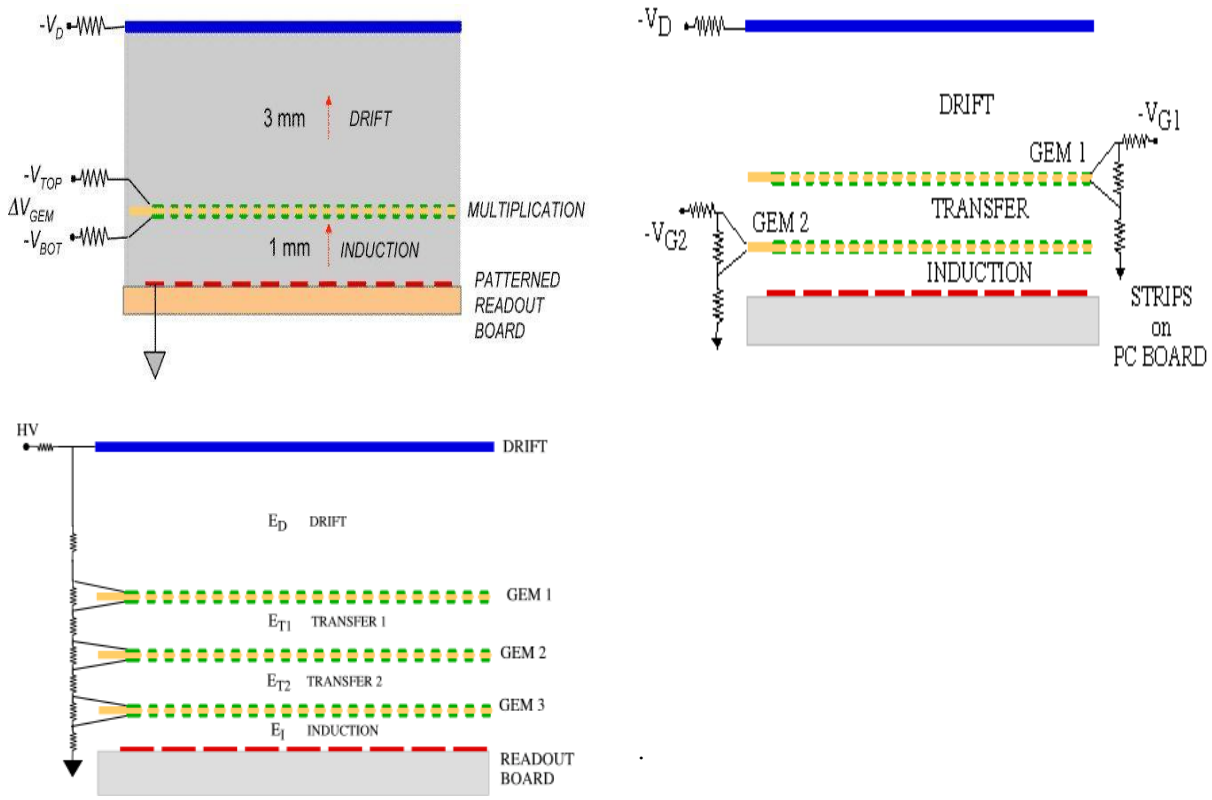

Figure 1. 11- Different GEM operating modes a) Single GEM configuration b) Double-GEM detector, c) Triple-GEM detector [17]

The multiplication process in the GEM can be described, approximately, using the parallel-plate approach:

$$M \approx e^{(\alpha d)} \Rightarrow \alpha / P \approx \ln M / Pd \qquad (1.2)$$
$$E / P \approx V_{GEM} / Pd$$

Where M is the GEM multiplication factor, d the inter electrode distance, α first Townsend coefficient, the number of secondary electrons produced per centimetre on the free electron path, P is the gas pressure, E the electric field inside the GEM hole and V_{GEM} the voltage applied across the GEM electrodes. This simplified approach considers the avalanche development in uniform electric field inside the hole over a distance of 50 μm, the typical GEM thickness.

The GEM gain is defined by the ratio between the number of electrons produced in the GEM holes and the number of primary electrons focused into the holes. This value is usually defined as the real GEM gain. The gain increases exponential with the applied voltage and the maximum gain corresponds to the

value achieved just before the onset of discharges or significant leakage current. The discharge probability depends on the gas used, being lower for gases operating at lower voltages or having higher diffusion coefficients. There is also dependence on the radiation energy and on the irradiation flux. Imperfections in the geometry or impurities also contribute to increase the discharge probability. A leakage current may appear in the electrodes due to the infinite resistance of the insulator.

Figure 1. 12 depict the charge gain as a function of the voltage applied to the GEM, obtained for several Xe pressures [59]. It is evident the exponential dependence of the gain with V_{GEM}. The decrease of the gain for increasing pressures is caused by a drop of the reduced electric field value (E/p) in the GEM holes, were the multiplication occurs. The increase of pressure should be followed by a proportional increase on the GEM voltage, to keep E/p constant. However, that is not possible due to intrinsic GEM properties; witch limits the maximum applied voltage before the onset of discharges.

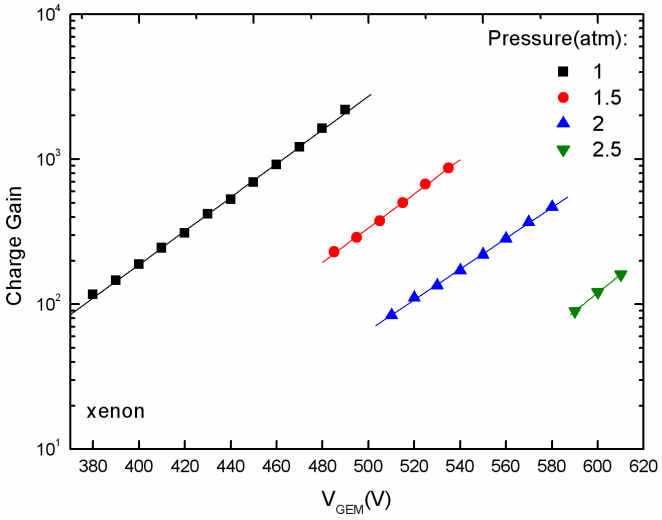

Figure 1. 12- Charge gain as a function of the voltage applied to the GEM for different xenon pressures [59].

Different gas mixtures may achieve higher gains, for example, as shown in Figure 1. 13, gain values of the order of 10^4 were achieved for argon based mixtures.

Figure 1. 14 depict a graph with the gain performance of single, double and triple-GEM configurations, where it is evident that multiple GEM configurations can achieve higher gain values. The voltage applied to the GEM in the different configurations is however lower for multi-GEM configurations. Figure 1. 14 also indicate the discharge probability for the different configurations.

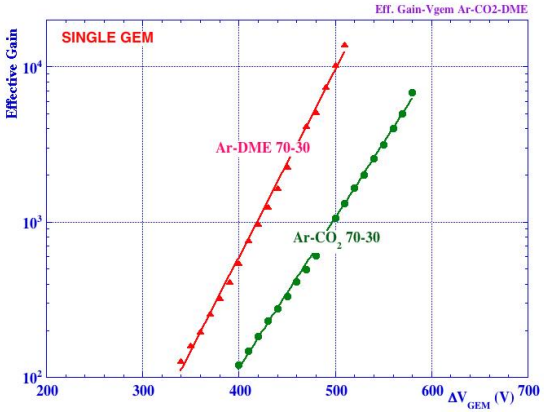

Figure 1. 13- Effective gain dependence on GEM voltage for two gas mixtures [17].

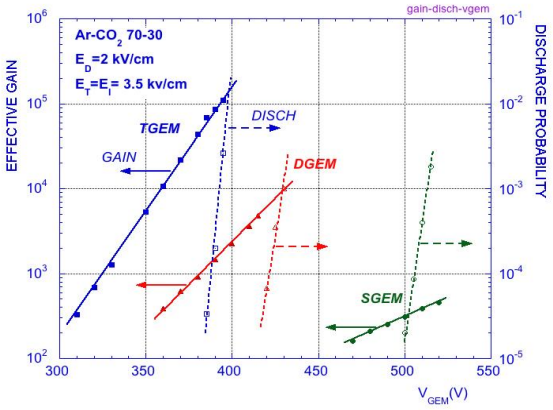

Figure 1. 14-Gain and discharge probability for irradiation with alpha particles in single, double and triple GEM configuration [17].

The electric field values in the drift and induction regions, as well as the transfer field for multiple GEM configurations, influence the charge transfer mechanism of the GEM and consequently the gain performance. The collection efficiency (*C*) is the fraction of electrons collected into the GEM holes per number of electrons (ions) arriving in the drift volume. The extraction efficiency (X) is the fraction of electrons (ions) extracted from the GEM holes to the induction volume per number of electrons produced in the holes. The effective gain measured in a separated electrode, G_{eff}, is related to the real GEM gain, G_{real}, by [22]:

$$Geff = C Greal\ X \qquad (1.3)$$

The optimization of the transfer coefficients, collection and extraction, is essential to improve the performance of the GEM. In Figure 1. 15 it is plotted the dependence of the collection and extraction efficiencies with the electric field proportion E_{ext}/E_{hole}. E_{ext} is the external field strengh, given by the relation between the flux onto an external electrode and it size. The E_{hole} can be parameterized by [22]:

$$E_{hole} = a\ V_{GEM} + b\ (E_{drift} + E_{ind}) \qquad (1.4)$$

where E_{drift} is the drift field, E_{ind} the induction field, V_{GEM} the GEM voltage and a and b parameters depending on the GEM geometry. From Figure 1. 15 it can be concluded that the collection efficiency is better for low drift field values, a field augment will cause a decrease in the fraction of electrons that go into the GEM holes. The extraction efficiency is better for higher E_{ext}/E_{hole} values, more electrons are extracted from the GEM holes as the external field increases. Thus,

the drift field should be kept at low values while the induction field should have high values.

A proper choice of the applied potentials is also important to reduce the ion re-injection in the drift volume, the ion back flow, which affects the detector performance.

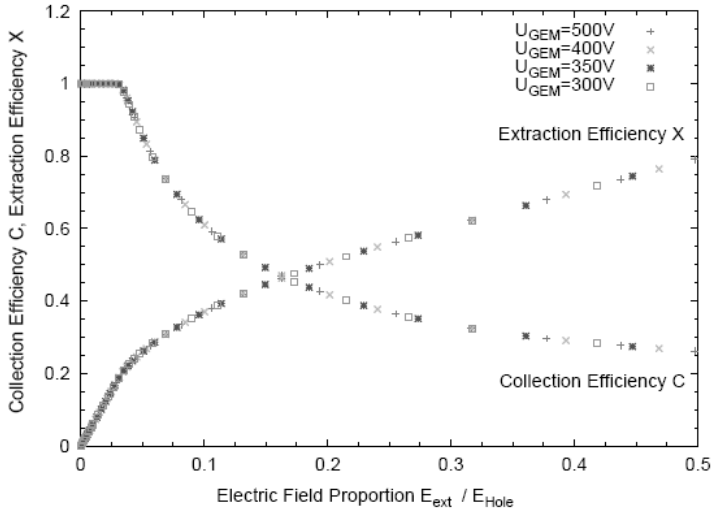

Figure 1. 15- Simulation of the extraction efficiency X and collection efficiency C for several GEM voltages, V_{GEM}, as a function of the ratio between external and hole fields [22].

The occurrence of discharges is one of the main problems of the GEM operation, which in certain situations can be irreversible. The sequence of events leading to a discharge is initiated when the avalanche size (product of ionizations and gain) exceeds a critical value, the Rather limit [69], of a few10^7 ion–electron pairs. When a particle crossing the detector releases an exceptionally high number of electron-ion pairs in the active gas volume of the detector, the total charge created in the subsequent amplification process may exceed a certain value, corresponding to the Rather limit, for the development of a stream in the avalanche. The stream produces an ionized and therefore conductive channel between the anode and the cathode where the discharge takes place. Some studies, [70][71], suggest that the absolute charge value that corresponds to the Raether limit is not fixed, but depends on the specific operating conditions, like the voltage applied to the GEM.

An advantage of GEM configurations relies in the fact that the charge readout electrode is independent, therefore a GEM discharge will not affect directly the sensitive electronics.

The photon and ion feedback, release further electrons from the detector surfaces by photoelectric effect or ion collisions, respectively, also limiting the GEM operation. The electrons released from the surfaces drift to the GEM holes

resulting in an augment of the original signal amplitude, limiting also the maximum achievable gain.

1.5.3 Aplications

The Gas Electron Multiplier was subject of considerable progress in the last years motivated by the growing interest in their potential applications. The advanced features of GEM based detectors like high counting rate, excellent spatial resolution, good imaging capability, operation in magnetic fields, large sensitive area, flexible geometry, capability to operate in cascade and low cost [2] make them attractive to applications in high-energy physics, like TOTEM (Total Cross Section, Elastic Scattering and Diffraction Dissociation) at the Large Hadron Collider [72] and COMPASS (COmmon Muon Proton Apparatus for Structure and Spectroscopy) [73].

GEM detectors have shown a good capability to provide X-ray absorption radiographies of small mammals. The spatial resolution obtained with the GEM is 0,1 - 0,2 mm. Figure 1. 16 a) shows an X-ray absorption radiography of a bat obtained with an X-ray tube of 8 keV [23].

Studies regarding the scintillation in GEM-based detectors show that, with appropriate gas mixtures the avalanche emits a large number of photons, in the UV, visible and/or NIR bands. Using CCDs as readout, imaging detectors can be developed to be used with X-rays, alpha particles and neutrons. Figure 1. 16 b) is an image of alpha particle tracks obtained with a triple GEM configuration using a CCD for the readout of the light emitted in the avalanches [74].

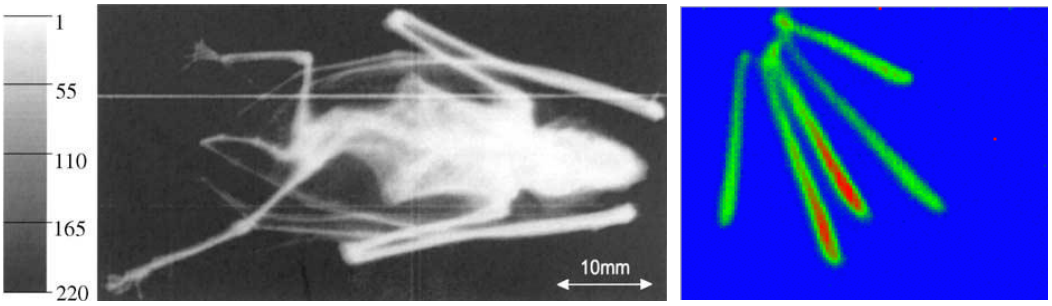

Figure 1. 16- a) X-ray absorption radiography of a small mammal. The grey scale indicates the number of photons counted in the pixels [23]. b) Individual alpha particle tracks visualized with the imaging triple- GEM detector coupled to a CCD camera [74].

1.6 GEM-MIGAS

The Gas Electron Multiplier with a Micro–Induction Gap Amplifying Structure (GEM-MIGAS) was recently proposed by J. A. Mir as an alternative elec-

tron multiplier configuration [25]. The GEM-MIGAS is a hybrid structure based on the GEM coupled to a Micromegas induction gap, i.e. a GEM having a short induction gap of few tens of microns, where additional charge multiplication take place.

1.6.1 Origin & Structure

A typical GEM configuration sets the induction region gap, distance between the bottom and the readout plane, at 1 mm or more. Kapton GEMs are susceptible to absorption by water vapour and other counter gases, which origin the sag of the GEM foil and thereby modify the initial induction gap value. As observed in Figure 1. 15 the effective GEM gain is strongly dependent on the induction field, therefore GEM sagging leads to effective gain instability. One way to circumvent this is to introduce dielectric pillars between the GEM foil and the readout plane at regular intervals. Studies with a standard GEM coupled to a micromesh plane with Kapton pillars of 50 μm were carried out by J. A. Mir at the Rutherford Appleton Laboratory, that was the origin of the GEM-MIGAS device [25].

The GEM-MIGAS operation principle is based on electron multiplication in GEM holes as well as in the induction gap, thus combining the charge amplification properties of a GEM and a Micromegas in a single device. This results in elevated charge gains, more efficient charge extraction from the GEM-holes and charge collection by the anode readout. The lower operational voltages in the GEM, with minimum sparks rate, make the device lifetime longer. Due to the existence of higher induction fields, GEM-MIGAS also exhibits a better gain stability when compared with the conventional GEM, operated with induction fields of about 1kV/cm [26].

In the first GEM-MIGAS prototype, the gap thickness was 50 μm and kapton pillars ensure the parallelism between the GEM and the induction plane. The induction electrode is a micromesh manufactured at CERN TS-DEM workshop, made of a 5 μm thick copper foil with 25 μm diameter holes etched with a pitch of 50 μm. The kapton pillars are 50 μm tall and 150 μm in diameter, distributed at 2 mm intervals. The micromesh was glued to a 10×10 mm^2 anode readout (G-10 board) and stacked together with the GEM frame. A schematic view of the GEM-MIGAS is shown in Figure 1. 17 a, while in Figure 1. 17 b is a photomicrograph of the micromesh, where the Kapton pillars are seen in detail.

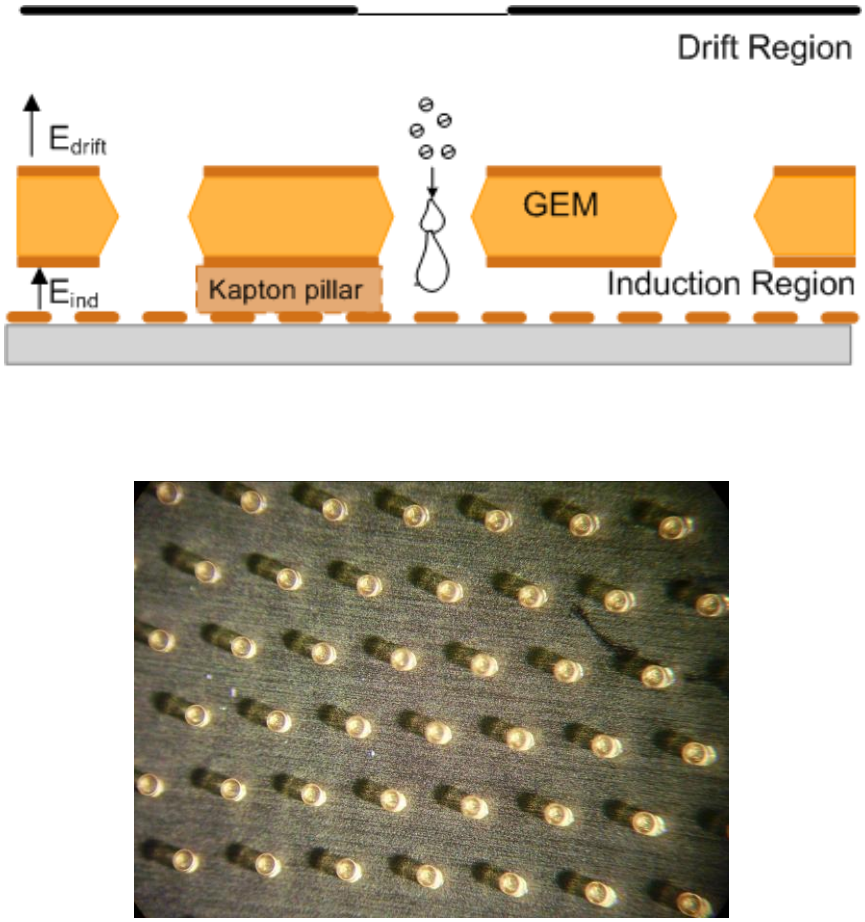

Figure 1. 17- Schematic view of GEM-MIGAS detector.

A few improvements have been done in the induction electrode in order to increase the gap thickness. The second GEM-MIGAS model was also manufactured at CERN TS-DEM workshop. It consists of a 10x10 mm^2 copper anode where insulating pillars of height ranging from 50 to 300 μm were placed at 1 mm intervals. In order to construct the GEM-MIGAS, the anode readout was coupled to the GEM frame, the pillars being in direct contact with the GEM.

1.6.2 Preliminary studies

The first studies carried out with a GEM operated with a micromesh readout plane were performed with argon-isobutane and helium-isobutane gas mixtures [25] [26], at Rutherford Appleton laboratory by J. A. Mir.

The experimental work carried out with Ar/iso-C_4H_{10} (75/25%) evaluates the performance of GEM-MIGAS, measuring the essential operational parameters of this detecting system using a 5.9 keV X-ray source [25]. The characteristics investigated include the effective gain, the gain stability and the energy resolution. These studies demonstrated several advantages of this detector configura-

tion when compared with the standard GEM operation, such as lower operational voltages, higher effective gains and effective gain stability. The highest effective gain was approximately 27000 when the voltage across the GEM holes (V_{GEM}) was set at 500V and the induction field (E_{ind}) at 30 kV/cm. The best energy resolution obtained for 5.9 kev X-ray was 15.2% (FWHM) for V_{GEM}= 470V (effective gain 1900) and E_{ind}= 6kV/cm.

The GEM-MIGAS effective gain is depicted in Figure 1. 18 as a function of E_{ind} for different V_{GEM} values and as a function of V_{GEM} for several E_{ind} values. The highest effective gain at the lowest induction field of 6kV/cm was around 6000. Increasing the induction field the gain improves up to about 27000 when the induction field is 30kV/cm. The effective gain increases almost linearly with the induction field, given that further electron multiplication begins in the induction region (parallel plate amplification mode).

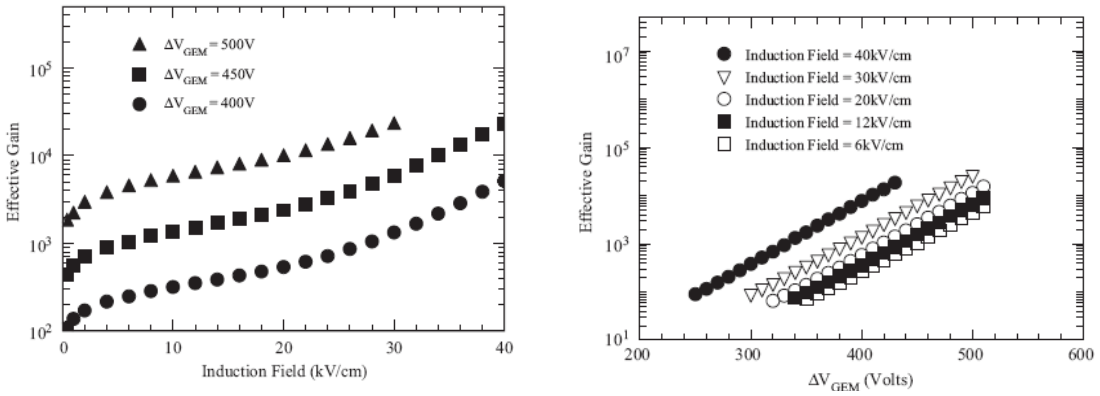

Figure 1. 18- a) GEM-MIGAS effective gain using Ar(75%)-isobutane(25%) gas mixture: a) as a function of the induction field for V_{GEM}=400, 450 and 500V; b) as a function of the V_{GEM} for different induction fields. The drift field was 3.5 kV/cm in both cases [25].

The energy resolution is depicted in Figure 1. 19 as a function of E_{ind} (a) and the effective gain (b). The optimum X-ray energy resolution was observed for E_{ind} values between 2and 15 kV/cm, beyond which a fast deterioration is observed as a result of the gain augment. An optimum pulse height spectrum for 5.9 keV X-ray was achieved for a gain of 1900 (V_{GEM}= 470 V, E_{ind}=6kV/cm) with an energy resolution of 15.2%.

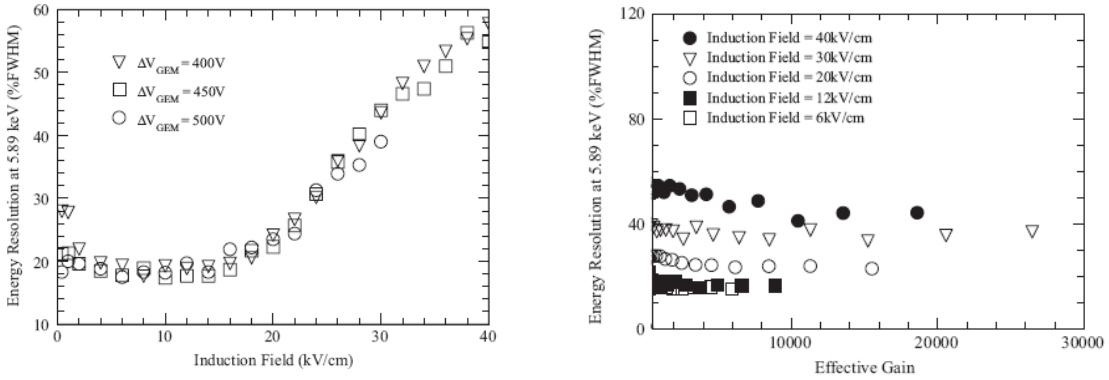

Figure 1. 19- a) Energy resolution of 5.9 keV X-rays in Ar(75%)-isobutane(25%) as a function of E_{ind} for a V_{GEM}= 400, 450 and 500V (a) and as a function of the effective gain for several E_{ind} values (b). The drift field was -3.5kK/cm in both cases [25].

Further studies of GEM-MIGAS operation evaluate the gain properties at 6 keV X-rays using argon-isobutane (IB) and helium-isobutane gas mixtures [26]. For the argon-based mixture, the highest effective gain was approximately $2x10^4$ as seen in Figure 1. 20 a). No further gain enhancement was observed by increasing the induction field up to 100kV/cm. Higher gains were obtained for a He(75%)-IB(25%) gas mixture as seen in Figure 1. 20 b). In this case the increase of E_{ind} up to 100kV/cm leads to a significant gain enhancement. In general, the highest effective gains of about 10^5 were obtained when using lower voltages across the GEM holes, between 100 and 300V, and highest induction fields. The gain values obtained with He(75%)-IB(25%) are high enough to use the GEM-MIGAS as a single-electron counting device.

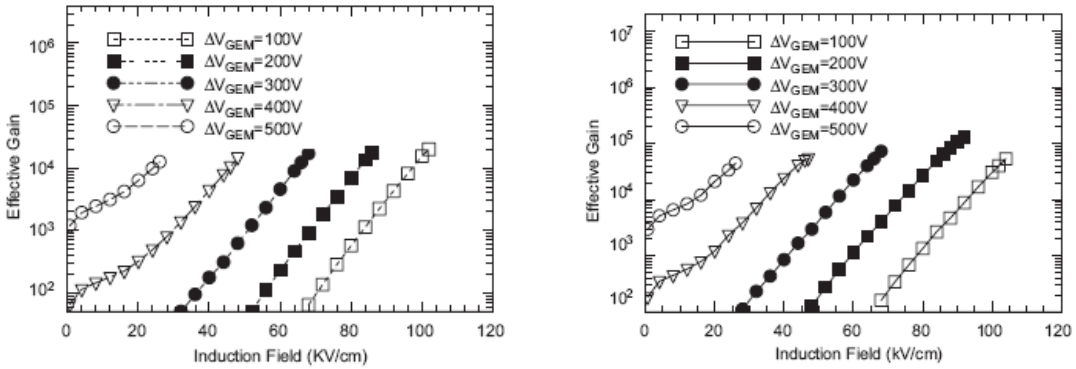

Figure 1. 20- Effective charge gain as a function of the E_{ind} for several ΔV_{GEM} values, for a) Ar(75%)-IB(25%) mixture and b) He(75%)-IB(25%) mixture . E_{drift}=0.25kV/cm in both cases[26].

The best energy resolution (Figure 1. 21) was approximately 18% and 32%, (FWHM), for Ar(75%)-IB(25%) and He(75%)-IB(25%), respectively. The optimum resolution for each curve occurred when the effective gain exceeded 10^3.

The energy resolution is optimum for voltages across the GEM holes between 300 and 500 V.

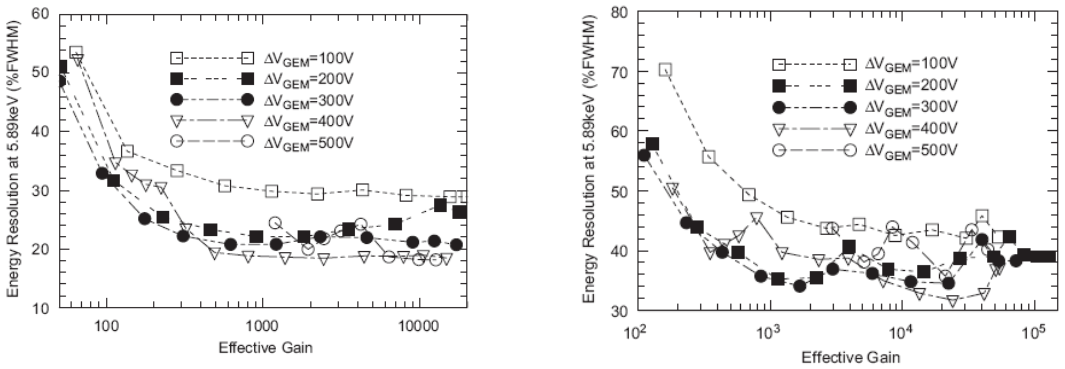

Figure 1. 21-Energy resolution for 5.9 keV X-rays as a function of the effective charge gain for different V_{GEM} values in Ar (75%)-IB(25%) mixture (a) and He(75%)-IB(25%) mixture (b). E_{drift}=0.25kV/cm, in both cases [26].

The GEM-MIGAS response to single electrons was investigated for He/iso-C_4H_{10} (85/15%) mixtures [27]. The single-electron pulse height distributions, Figure 1. 22 a), obtained for the GEM-MIGAS operated in GEM mode, i.e low induction field values, were fitted to a Polya distribution in order to determine the average charge gain. The average gain determined, Figure 1. 22 b), reaches a maximum value about 7x10^4. A good agreement was found between the gain values obtained with two different sources, the UV and the X-ray source.

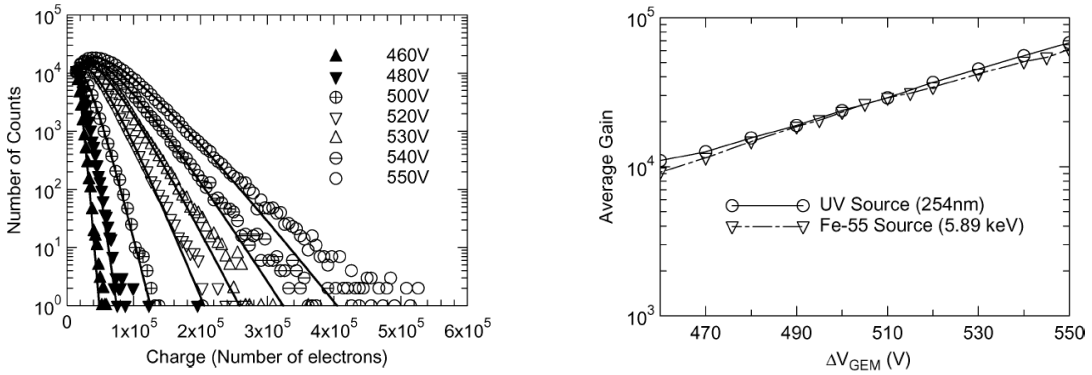

Figure 1. 22- a) Single-electron pulse-height distributions measured with the GEM-MIGAS detector operated in GEM mode, in He/iso-C_4H_{10} (85/15%) gas mixture for V_{GEM} in the range of 460–550 V. The induction field was 6 kV/cm and the drift field 0,25 kV/cm. b) the average charge gain as a function of GEM. Obtain with UV and X-ray sources.

Extending the induction field range applied to the GEM-MIGAS, Figure 1. 23 a), a better Polya fit to the single-electron pulses is observed, when compared to the GEM-mode operation. The electron multiplication within the GEM holes as well as in the induction gap results in higher average charge gain of about

7x10^5, which is a 10 times improvement over the GEM mode operation, Figure 1. 23 b).

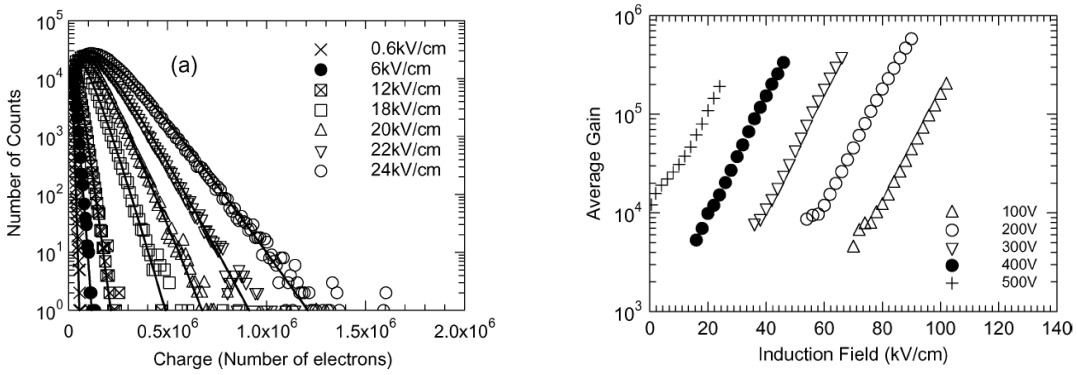

Figure 1. 23- a) Single-electron pulse-height distributions obtained with the GEM-MIGAS detector in He/iso-C_4H_{10} (85/15%) gas mixture, for several values of induction field with ΔV_{GEM} = 500 V. The drift field was 0,25 kV/cm. b) Average charge gain as a function of the induction field measured with the GEM-MIGAS detector in He/iso-C_4H_{10} (85/15%) gas mixture for single-electrons, E, and for voltages across the GEM, ΔV , in the range of 100–500 V. In all cases E = 0,25 kV/cm.

In GEM mode operation, a detection efficiency of about 95% was obtained for a charge gain of 7x10^4, Figure 1. 24 (a). For the GEM-MIGAS mode operation, detection efficiencies over 98% are possible when the average gain exceeds a few 10^5 Figure 1. 24 (b)

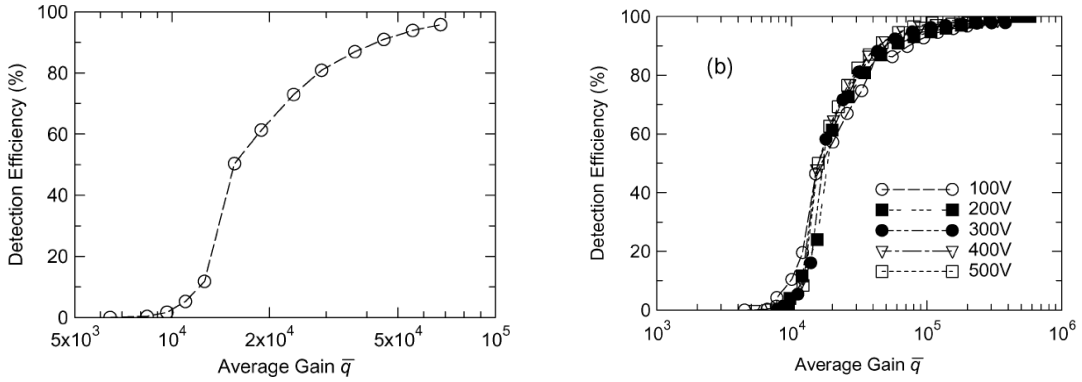

Figure 1. 24- Single-electron detection efficiency as a function of the average gain q. for a) GEM mode operation with E_{ind} = 6kV/cm and E_{drift}= 0,25 kV/cm; b)GEM-MIGAS operation mode for several GEM voltages with E_{drift}= 0,25 kV/cm.

In summary, charge gains above 10^5 and well above 10^4 were obtained for the He-based and Ar-based mixtures, respectively, with GEM voltages as low as 200 V, ensuring GEM operation conditions well below the GEM discharge limit. These gains present a factor of about 5 times higher than to those obtained in the GEM-mode operation. The GEM-MIGAS response to single electrons, in He/iso-C_4H_{10} (85/15%) mixtures, reaches charge gains as high as 7×10^5, one

order of magnitude above the GEM-mode values. The detection efficiency for the GEM-MIGAS configuration is also higher compared to single GEM configuration.

1.6.3 Road Map

The good performances obtained in the previous studies motivate a deeper investigation of GEM-MIGAS operation, resulting in the subject of this PhD programme work. The investigation work is focused essentially in four aspects:

- Electric field simulations using Maxwell 3D field simulator from Ansoft in order to evaluate the electric field profile within GEM holes and in the induction region.
- GEM-MIGAS operation in Argon-Methane based mixtures: studies in the standard quenched gas mixture Ar/CH4 (90/10%) and in pure CH_4 and pure Ar. CH4 has the advantage of presenting one of the highest photoelectron extraction efficiency, important for gaseous photomultipliers (GPMs), while Ar is useful in sealed chambers, e.g. for rare-event detection .
- GEM-MIGAS single-electron response for different induction Gap thicknesses. Larger induction gap thicknesses may sustain larger voltage differences, which may lead to higher effective gains. In this work, is investigated the average charge gain derived from the induction gap for several gap thicknesses, d, of 50,100, 150, 200, 250 and 300 μm.
- GEM-MIGAS ion back-flow suppression capability, the fraction of total avalanche-ions that reach the semi-transparent photocathode, for induction gap thicknesses in the range of 50–300 μm.
- Viability of GEM-MIGAS as a neutron gaseous detector. This study includes optimization of the GEM-MIGAS gaps in the 20-250 μm range whilst operating in pure CF_4. Study of the influence of the GEM hole diameter whilst keeping the induction gap fixed in pure CF_4 and finally, the optimum GEM-MIGAS configuration (induction region gap and GEM hole diameter) in He/CF_4 based mixtures.

Chapter 2

Gas Detector Physics

This chapter gives a brief summary about the most relevant processes in gaseous detectors. The knowledge of the mechanisms by which radiation interacts and loses energy in its interaction with matter is essential. The interaction processes depends on the type of particle interacting in the medium and the gas mixture.

2.1 Interaction of ionising radiation with matter

The radiation can be classified in two different type, ionising and non-ionising radiation (Figure 2. 1). Non-ionizing radiation refers to electromagnetic radiation with a wavelength longer than 10 nm which does not have enough energy to ionize an atom or molecule, i.e. remove an electron from an atom or molecule. This part of the electromagnetic spectrum includes radio waves, microwaves, visible light (770 to 390 nm), and ultraviolet light (390 to 10 nm). Instead of producing charged particles when passing through the matter, the electromagnetic radiation has sufficient energy only for excitation, the shift of an electron to a higher energy state. Nevertheless, different biological effects are observed for each type of non-ionizing radiation, the most common are effects in the skin and eyes. The extension of the effects depends on the radiation energy.

The ionizing radiation consists of highly-energetic particles or waves that can remove at least one electron from an atom or molecule, corresponding in the electromagnetic spectrum to X-rays (from 0.01 to 10 nm) and γ-rays, with shorter wavelength. It also includes all the atomic and subatomic particles, such as electrons, positrons, protons, alphas, neutrons, heavy ions and mesons. Exposure to ionizing radiation can cause damage to living tissue, like mutation and cancer. The severity of the effects is related to the radiation exposure dose and

time. Nevertheless, there are many practical uses of ionizing radiation, such as radiotherapy, medical radiography and also sterilization tools and equipment in medicine and biology fields. In biology and agriculture, radiation is used to induce mutations to produce new or improved species.

The detection of radiation is based on the interaction processes and on the energy deposited by the radiation in the matter. In this chapter is presented a brief summary about the interaction mechanisms of ionizing radiation, including charged particles, photons and neutrons.

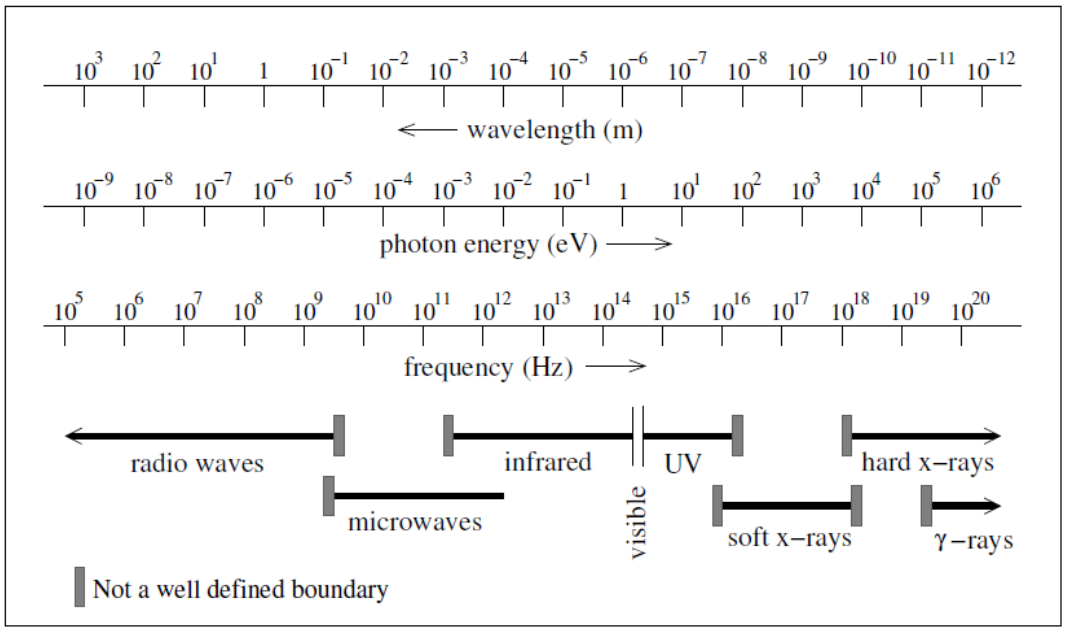

Figure 2. 1- Electromagnetic spectrum.

2.1.1 Interaction of charged particles with matter

The interaction mechanisms of charged particles when they pass through the matter can be classified as:

- Coulomb interactions with electrons and nuclei:
  - Inelastic collisions, responsible for Ionization and Excitation
  - Elastic scattering by cloud electrons
- Bremsstrahlung(electromagnetic radiation produced by radiative losses)
- Emission of Cherenkov radiation
- Nuclear interactions

When fast electrons cross matter, part of their energy is converted into electromagnetic radiation in the form of Bremsstrahlung, which in German means braking radiation. The energy lost by the electron in this interaction appears in the form of an x-ray photon with energy equal to the change in the kinetic ener-

gy of the electron. The fraction of electron energy converted into Bremsstrahlung increases with the augment of the electron energy and is larger for materials of high atomic number. This process is important in the production of X-rays in conventional X-ray tubes. The energy loss due Bremsstrahlung is negligible in gaseous detectors, it is only important for particles with energy above 511 keV.

Cherenkov radiation is visible electromagnetic radiation emitted by particles travelling in a medium with a speed greater than the speed of light. It is important for particle physics applications in Cherenkov counters. However, it is negligible in gaseous detectors given the small energy fraction loss.

The nuclear interactions only occur for higher energies, above a few MeV. A charged particle travelling through the detector medium can interact with the atomic electrons or the nucleus of the atom. Given that the nucleus radius is approximately 10^{-14} m and the atom radius is approximately 10^{-10} m, the collisions with atomic electrons are more relevant than the ones with atomic nuclei [12]. Therefore, the nuclear collisions will not be considered here.

The interaction processes relevant for this research work are the Coulomb interactions.

The Coulomb interactions between electrically charged particles and the detector medium, inelastic or elastic collisions, result in energy loss. The major contribution comes from the inelastic collisions, originating excitation and ionizing.

Inelastic collisions occur when the interaction between a free charged particle and atomic electrons results in atomic ionization or excitation. The collision can be considered as inelastic whenever a conversion from kinetic to potential energy occurs.

The following relation gives the Coulomb force:

$$F = k\left(\frac{ze^2}{r^2}\right) \quad (2.1)$$

being *ze* the charge of the free particle, k the dielectric constant and r distance between the charged particle and the atomic electron. The action of the Coulomb force over a period can result in energy transference from the moving electron to the atomic electrons. Since a bound atomic electron is in a quantized state, the passage of the free electron can lead to ionization or excitation of the atom.

The ionization occurs when the electron obtains enough energy to leave the atom, i.e. the energy deposited is larger than the binding energy of the atomic electron. As a result, the electron becomes a free particle with kinetic energy, E_{e^-}, given by

the difference between a fraction of the energy of the free particle and the biding energy (ionization potential).

The released electron will behave as a free charged particle, and can cause further ionizations if its energy is high enough. Fast electrons produced by ionizing collisions are called δ rays. The ionization leaves behind a positive ion, a massive particle compared to an electron. The ion has the tendency to recombine with a free electron, becoming a neutral atom again.

The excitation occurs when the atomic electron gets enough energy to move to an empty state with higher energy. The atomic electron jumps from a state with energy E_1 to one with energy $E_2 > E_1$ producing an excited atom. In a short period of time (10^{-8} to 10^{-10} s) the electron will move again to a lower energy state. If the electron falls from E_2 to E_1, the energy E_2-E_1 is emitted in the form of an X-ray.

The elastic collisions occur when free charged particles do not have enough energy to originate atomic ionization or excitation. In this interaction, the incident particle loses the energy required for conservation of the kinetic energy and the linear momentum. The free electron is deviated from its original trajectory. Elastic collisions are not very important for the energy loss and detection of charged particles.

Stopping power

The linear stopping power (S) of a charged particle in a given material is defined as the differential energy loss, dE, within the material divided by the corresponding differential path length, dx :

$$S = -\frac{dE}{dx} \quad (2.\ 2)$$

The value dE/dx is also called specific energy loss and can be described by the Beth-Block formula:

$$\frac{dE}{dx} = \frac{4\pi r e^4 z^2}{m_0 v^2} NZ\left[\ln\frac{2m_0 v^2}{I} - \ln(1-\beta^2) - \beta^2\right] \quad (2.\ 3)$$

being v and ze the velocity and charge of the primary particle, N and Z the density and atomic number of the absorber atoms, m_0 the electron rest mass, e the electron charge and c the speed of light. The parameter I represents the average excitation and ionization potential of the absorber and is normally treated as an experimental parameter for each element. Figure 2. 2 represents the specific energy loss in air for different particles as a function of their energy.

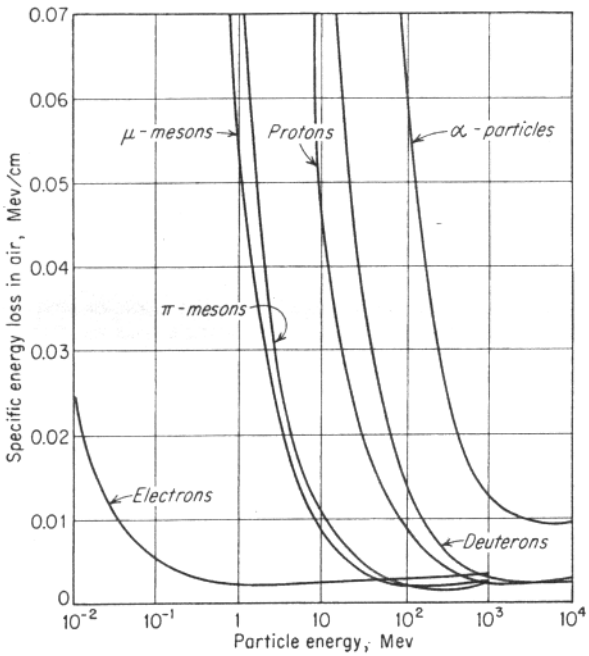

Figure 2. 2- Specific energy loss in air as a function of energy for different charged particles [2].

The interaction of each particle has its own probability, therefore Beth-Block formula is slightly different for electrons, positrons and heavier charged particles like protons, deuterons and α-particles.

For electrons, assuming that all the atoms and their atomic electrons act independently, the specific energy loss due to ionization and excitation, i.e. the energy lost by collision interactions, per unit of distance travelled by an electron, is:

$$-\left(\frac{dE}{dx}\right)_e = \frac{2\pi e^4 NZ}{m_0 v^2}\left[\ln\frac{m_0 v^2 E}{2I^2(1-\beta^2)} - \ln 2\left(\sqrt{1-\beta^2}-1+\beta^2\right) + (1-\beta^2) + \frac{1}{8}\left(1-\sqrt{1-\beta^2}\right)^2\right] \quad (2.4)$$

The electrons can also lose energy by radiative processes, like Bremsstrahlung. The total linear stopping power for electrons will be the sum of both components, collisional and radiative. Since Bremsstrahlung process is negligible in gaseous detectors, this effect will not be considered.

For low energetic electrons, $\beta << 1$, the Beth-Block formula is not valid anymore because the charge exchanged between the particle and the absorber becomes significant, so the equation can be re-written as:

$$\frac{dE}{dx} \approx 4\pi r_0^2 \frac{mc^2}{\beta^2} NZ \ln\left(\frac{mc^2\beta^2}{I}\sqrt{\frac{2.7182}{8}}\right) \quad (2.5)$$

As a conclusion, the stopping power is:

- proportional to z^2 particle,
- dependent on the speed of the particle, increasing as velocity decreases,
- proportional to the density of the material.

Range

A charged particle moving through a certain material loses its kinetic energy through the interactions with the material. For electrons the energy loss is essentially due to the slowing down in the penetration through the matter. The material thickness necessary to stop a particle with kinetic energy T, mass M, and charge z is the particle range in the material. For electrons, which have a crisscross path, the range is lower than the path length. The path length is the distance travelled by a particle until it stops.

The electron range can be calculated using a semi empirical equation developed by Tabata, Ito and Okabe, for electrons with energy in the range of 0.3keV to 30 MeV [12].

$$R(kg/m^2) = a_1\left(\frac{\ln\left[1+a_2(\gamma-1)\right]}{a_2} - \frac{a_3(\gamma-1)}{1+a_4(\gamma-1)^{a_5}}\right) \quad (2.6)$$

$$a_1 = \frac{2.335A}{Z^{1.209}},\ a_2 = 1.78\times10^{-4}Z,\ a_3 = 0.9891 - (3.01\times10^{-4}Z)$$

$$a_4 = 1.468 - (1.180\times10^{-2}Z),\ a_5 = \frac{1.232}{Z^{0.109}},\ \gamma = \frac{1}{\sqrt{1-\beta^2}},\ \beta = \frac{v}{c}$$

Where A is the atomic weight and Z the atomic number of the material. From the particle range the time required to stop a particle in the absorber can be calculated knowing its average velocity. For a non-relativistic particle, with a mass m_A and energy E, the average velocity can be obtained from:

$$\upsilon = c\sqrt{\frac{2E}{931m_A}} \quad (2.7)$$

with E in MeV and m_A in *amu*.

Interaction of photons with matter

A photon represents one quantum of electromagnetic energy and is treated as a fundamental particle in the Standard Model of particle physics. In this model the photon is assumed to have no rest mass (although it is never at rest). When

the photon is traveling in a medium, it slows down due to interaction with the medium and acquires an effective mass. In vacuum, however, it is considered to be massless.

The relation between the photon energy, E, wavelength, λ, and frequency, υ, is:

$$E = h\upsilon = h\frac{c}{\lambda} \quad (2.\ 8)$$

where h is the Planck constant and c the speed of light.

Another important property is that they carry momentum even though they have no rest mass, which can be expressed by:

$$p = \frac{E}{c} = \frac{h\nu}{c} = \frac{h}{\lambda} \quad (2.\ 9)$$

X-rays are photons, typically produced by atomic transitions such as excitation and ionization, while γ-rays are emitted in nuclear transitions.

The most relevant interaction processes of photons with matter are the photoelectric effect, Compton scattering, pair production and Rayleigh scattering, represented in

Figure 2. 3.

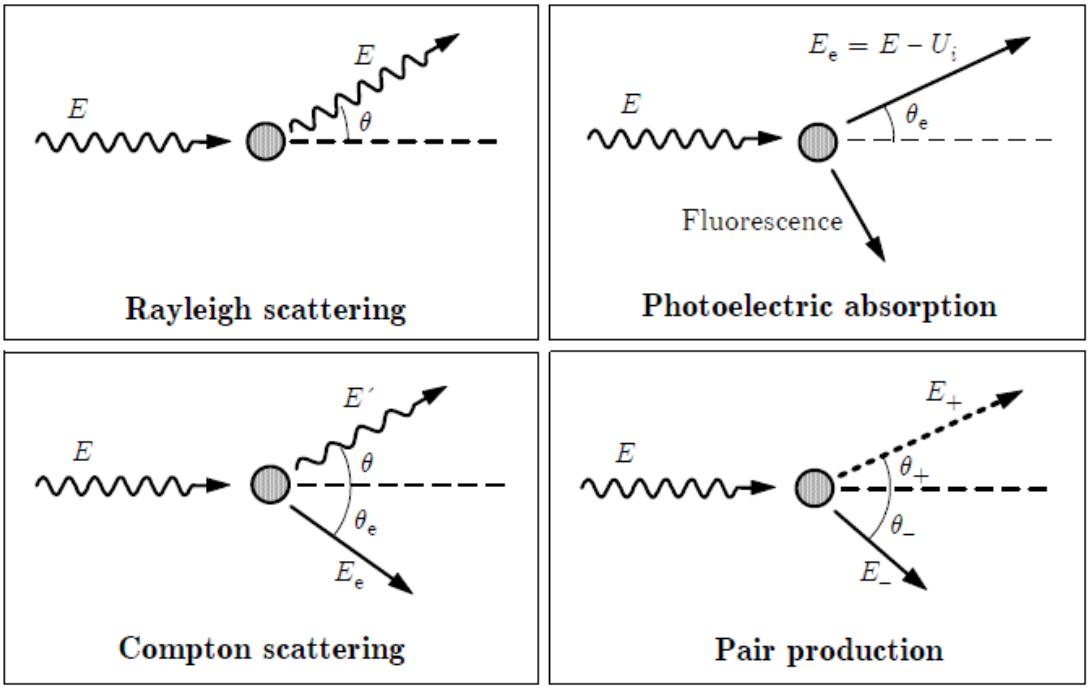

Figure 2. 3- Basic interactions of photons with matter [75].

The probability of each process is related to the energy of the incident photon and the atomic number of the absorber material. Figure 2. 4 shows the predominant regions for each effect as a function of the photon energy and the atomic

number of the absorber. The Rayleigh scattering is not represented since it is negligible when compared to the other effects.

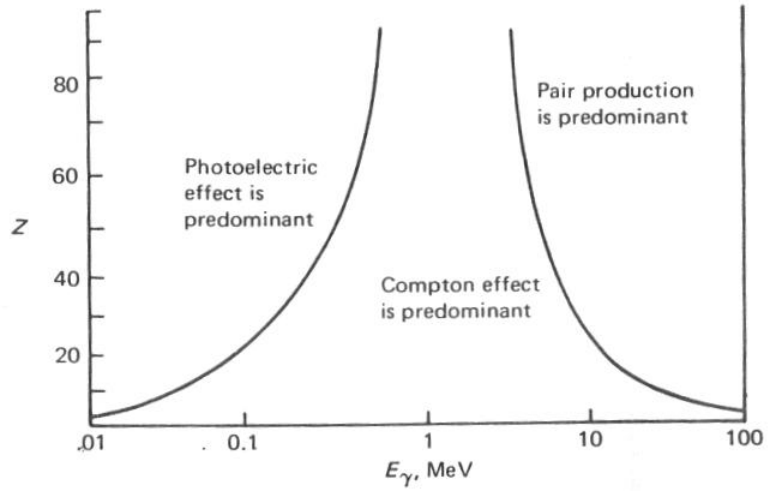

Figure 2. 4- Regions of predominance of the effect as a function of the energy. The lines show the values of Z and E for which the two neighboring effects are just equal. [2].

The attenuation of a photon beam when passing through a medium with thickness d, is [2] given by:

$$I = I_0 e^{-\mu d} \quad (2.\ 10)$$

were I_0 is the initial intensity of the beam and μ is the linear attenuation coefficient in the medium, which is given by the sum of the individual attenuation coefficients for each interaction process in the medium:

$$\mu = \tau(photoelectric) + \sigma(Compton) + \kappa(pair) \quad (2.\ 11)$$

PHOTOELECTRIC EFFECT

The photoelectric effect is a quantum process that occurs when the energy of the incident photon, E_γ, exceeds the biding energy of the electron in the shell, E_b. The photon energy and momentum are transferred to the interaction atom/molecule originating ionization. Therefore, the bond electron is ejected from the atom, creating a photoelectron. The photoelectron energy is equal to the difference between the energy of the incident photon and the bind energy of the shell from which the electron is liberated:

$$E_e = E_\gamma - E_b \quad (2.\ 12)$$

The photon disappears after a photoelectric interaction with an atom/molecule.

The interaction leaves the atom in an ionized state, with a vacancy in one of its bound shells. This vacancy is quickly filled by an electron, leading to the emission of characteristic X-ray or an Auger electron. The emission of an Auger electron is higher for low Z elements, for which electron biding energies are small. For example in Argon, about 15% of the photoelectric absorptions are followed by the emission of characteristic X-rays, while in 85% an Auger electron is produced. Auger electrons have a very short range due to the low energy, on the other hand X-ray photons can travel a distance around millimeters.

The characteristic X-ray cab be reabsorbed close to the original site through photoelectric effect, or they can also escape from the sensitive volume of the detector and influence their response, giving origin to Escape Peaks. The fraction of de-excitation that gives origin to photon emission is called fluorescence yield.

The momentum conservation leads to a recoil of the nucleus. Therefore, only electrons close to the nucleus contribute to the photoelectric absorption cross section, τ. There is not a single analytic expression valid for the probability of photon electric absorption per atom, over all ranges of photon energy and Z, but an approximation can be made [2]:

$$\tau \cong \text{constant} \times \frac{Z^n}{E_\gamma^{3.5}} \quad (2.\ 13)$$

The photoelectric effect is predominant for lower energies, below 0.5 Mev, and absorber materials with high atomic number.

COMPTON SCATTERING

The Compton scattering is a collision between a photon and a quasi-free electron. This effect is dominant when the photon energy is higher then the binding energy of the innermost electron in the target atom.

The initial photon collides with the electron, resulting in a recoil of the electron and the deflection of the photon with a certain angle, θ. The scattering angle, which can change between 0 to π. For θ=0, the scattered photon has almost the total amount of energy of the initial photon and the energy of the recoil electron is approximately zero. For $\theta=\pi$, the initial photon transfers the maximum energy to the recoil electron. This behaviour leads to a continuum energy spectrum for Compton effect.

The recoil electron is quickly absorbed by the matter, but the Compton photon can have new interactions according to is energy. In the case of small vol-

ume detectors, the scattered photon can escape to the exterior without being detected, so only the recoil electron is detected. If the scattered photon is absorbed in the detector (by photoelectric or Compton effect) its energy will be deposited in the detector adding up to the energy of the recoil electron, if both primary electron clouds are collected simultaneously.

The energy of the recoil electron, E_{e^-}, and the energy of the scattered photon, $h\nu'$, can be calculated using the follow equations[2]:

$$E_{e^-} = h\nu - h\nu' = h\nu\left(\frac{(h\nu/m_0c^2)(1-\cos\theta)}{1+(h\nu/m_oc^2)(1-\cos\theta)}\right) \quad (2.\ 14)$$

$$h\nu' = \frac{h\nu}{1+(h\nu/m_0c^2)(1-\cos\theta)} \quad (2.\ 15)$$

The probability of Compton scattering per absorber atom depends on the number of electrons available as scattering targets and therefore increases linearly with Z.

The differential scattering cross section, σ, is predicted by the Klein-Nishina formula [2]:

$$\frac{d\sigma}{d\Omega} = Zr_0^2\left(\frac{1}{1+\alpha(1-\cos\theta)}\right)^2\left(\frac{1+\cos^2\theta}{2}\right)\left(1+\frac{\alpha^2(1-\cos\theta)^2}{(1+\cos^2\theta)[1+\alpha(1-\cos\theta)]}\right) \quad (2.\ 16)$$

where $\alpha = h\nu/m_oc^2$ and $r_0 = 2.818 \times 10^{-13}$ cm is the classical electron radius. With this expression the most probable scattered angle can be calculated and then the energy of the scattered photon.

PAIR PRODUCTION

The pair production is an interaction between a photon and a nucleus. As a result, the photon disappears and an electron-positron pair is created. This effect occurs for photon energies above 1.022 MeV. If the photon has energy greater than 1.022 MeV, the excess of energy is converted into kinetic energy, which is shared between the positron and the electron. The electron is quickly thermalized, while the positron annihilate after slowing down in the medium, producing two photons with energy of 511 KeV. The energy of the pair electron-positron is [2]:

$$E_{e^-} + E_{e^+} = h\upsilon - 2m_0c^2 \quad (2.\ 17)$$

where E_{e-} is the electron energy, E_{e+} is the positron energy, $h\nu$ is the incident photon energy and $2m_oc_2$ is 1022 KeV.

There is not a simple expression for the probability of pair production per nucleus, but it is approximately proportional to the square of the absorber atomic number and it increases sharply with energy.

RAYLEIGH SCATTERING

In addition to the Compton scattering, there is the coherent scattering also known as Rayleigh scattering. This process neither excites nor ionizes the atom, and the original photon retains its original energy after scattering. Because virtually no energy is transferred, this process is often neglected. However, the direction of the photon is changed.

The probability of coherent scattering is only significant for low photon energies, typically below a few hundred keV, and it is most prominent in high-Z absorbers. The average deflection angle decreases with increasing energy.

2.1.3 Interaction of Neutrons with matter

The neutron was discovered in 1932 by Chadwick as a fundamental particle released in nuclear reactions and fission processes, characterized by the absence of charge and a mass number of 1.

Neutrons are uncharged particles and do not interact with atomic electrons when they pass through the matter, they interact only with atomic nuclei. The nuclear force associated to these atomic interaction is very short ranged, which means the neutrons have to pass very close to the nucleus for an interaction occurs. The neutron interactions are extremely weak electromagnetic forces unlike photon and charged particle interactions. When a neutron approaches a nucleus, it does not have to go through a Coulomb barrier, like charged particles, as a result the probability (cross section) for nuclear interactions is higher for neutrons than for charged particles. The small size of the nucleus compared to the atom leads to a low probability of neutron interactions and consequently they can travel considerable distances in matter without interacting.

The neutron energy determines the type of interaction with matter. The energy range can be from a few eV to the order of MeV. According to their energy, neutrons are classified as Cold, Thermal, Epithermal, Fast, Medium Energy or High Energy neutrons. Figure 2. 5 summarize the energy range and the predominant interaction process. In this work, only the Thermal neutrons, with

energies bellow 0.5 eV, will be considered. The dominant interaction for these neutrons is the elastic scattering.

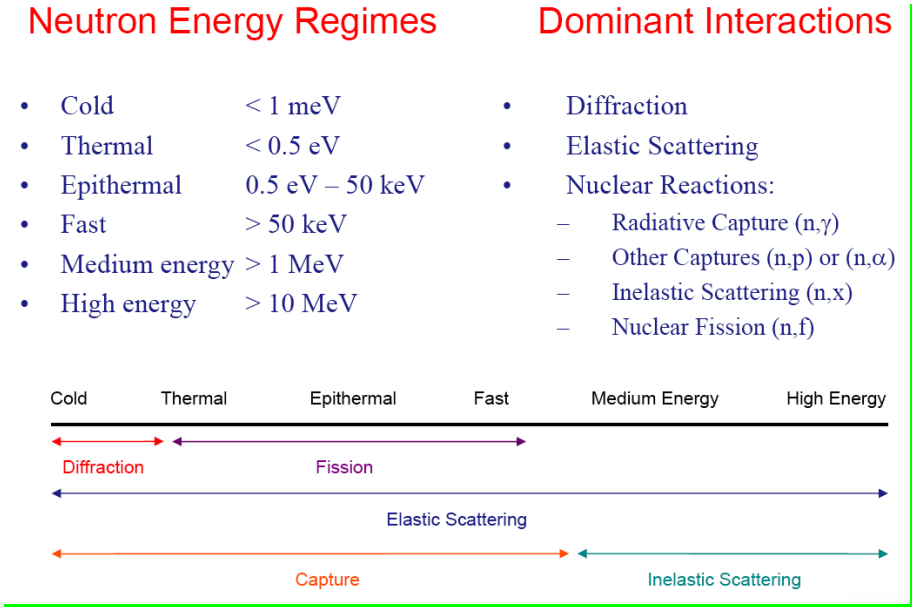

Figure 2. 5- Classification of neutrons according to their energy.

In scattering interactions, the neutron interacts with a nucleus and both particles reappear after the reaction. The scattering collision is indicated as (n,n) reaction or:

$$n + {}^{A}_{Z}X \rightarrow {}^{A}_{Z}X + n$$

The scattering interaction can be elastic or inelastic. In elastic scattering the total kinetic energy of the two colliding particles is conserved and its value is redistributed between the two particles. In inelastic scattering, part of the kinetic energy is given to the nucleus, which goes to an excited state. After the collision the excited nucleus will return to the ground state by emitting one or more γ-rays.

The neutron cross section is defined individually for each type of reaction and isotope. The total cross section, i.e. total probability that a reaction of any type will take place, is given by the sum of the individual cross sections. The cross section value is strongly related to the neutron energy and the atomic weight and atomic number of the target nucleus.

2.2 Charge Transport in Gases

The transport properties of electrons and ions in a gas medium, such as drift and diffusion, are very important characteristics of gaseous detectors. This subject has been a very important research field since the first half of the 20th centu-

ry. The transport properties have been studied in a large variety of gas mixtures. The electric field applied in the detector determines the transport properties of charged particles, therefore is important to optimize it according to the properties of each gas mixture.

2.2.1 Filling Gas

Virtually any gas can be used in gas proportional detectors, as the basic requirement for a detector to work as a proportional counter, the avalanche multiplication, occurs in all gases and their mixtures. However, specific experimental requirements restrict the choice of the gas since several factors need to be taken into account, such as low working voltage, high gain operation, high rate capability, good proportionality, drift and diffusion properties of electrons and ions, and charge collection efficiency.

The noble gases are the suitable choice because the avalanche multiplication occurs at much lower fields compared to complex molecules. This is a consequence of the many non-ionizing energy dissipation modes available in polyatomic molecules. Excited and ionized atoms are formed during the avalanche process. The excited noble gases can return to the ground state only through a radiative process and the minimum energy of the emitted photon is well above the ionization potential of the cathode metal. Therefore, photo-electrons can be extracted from the cathode and initiate a new avalanche very soon after the primary cloud. The argon is the suitable choice, taking into account the expensive price of xenon and krypton. However, a gas counter operated with argon does not allow gains above 10^3-10^4 without entering into a permanent discharge operation due to photon mediated feedback processes. Therefore, Ar based mixtures with CH_4, CF_4, CO_2 are much used. The properties of several gases used in proportional gas detectors are summarized in Table 2. 1 [82].

The behaviour of polyatomic gases is very different, especially when they have more than four atoms. Polyatomic molecules have a large amount of non-radiative excited states (rotational and vibrational) which allow the absorption of photons in a wide range of energy. This is a common property of most organic compounds in the hydrocarbon and alcohol families and of several inorganic compounds like freons, CO_2, BF_3 and others. The molecules dissipate the excess energy either by elastic collisions or by dissociation into simpler radicals. This behaviour is also observed when an ionized polyatomic molecule neutralizes at the cathode, the secondary emission is very improbable. In the neutralization process, the radicals recombine into simpler molecules (dissociation) or form larger complexes (polymerization).

In noble gases, the excited atoms/molecules resulting from the avalanche multiplication process may return to their ground states by the emission of photons, which can interact again with the gas and produce additional charge, usually designated as secondary avalanche process. As a result, the proportionality between the number of primary electrons and the multiplied charge can be lost. This problem can be solved by adding polyatomic gases, such as methane or a few inorganic gases like CO_2 or BF_3. These molecules act as quenchers, absorbing the radiated photons and then dissipating this energy through dissociation or elastic collisions. The quenching efficiency roughly increases with the number of atoms in the molecule. Good photon absorption and suppression of the secondary emission allow gains above 10^6 before discharge. Organic compounds, however, tend to cause aging effects in the detector due to the build-up of polymers in the anode and cathode, which in general are flammable, requiring special safety precautions. Therefore a suitable mixture of counting gas and quencher is essential for an effective and stable operation of gaseous detectors.

The gas properties can change considerably with a little concentration of a second gas whose ionization potential is smaller than that of the principal component. This is the Penning effect and is related to the existence of long-lived or metastable excited states in the main gas. If the excitation energy is larger than the ionization energy of the added component, then a collision between the metastable excited atom and a neutral additive atom can ionize the additive. Because the excitation energy would otherwise be lost without the additive, a greater number of ions pairs will be formed per unit of energy lost by the incident radiation.

The addition of small quantities of electronegative gases allows the achievement of higher gains before the saturation, given their photon quench capability. However, the gas multiplication depends essentially on free electron motion and electronegative gases capture free electrons forming negative ions that can't induce avalanches. To optimize the detector efficiently it is necessary that the electrons do not recombine with gas molecules, therefore only limited amounts of electronegative gases can be used.

A gas detector can operate in sealed or flow mode. Sealed detectors usually are vacuum pumped to the order of 10^{-6} to eliminate the most part of impurities with the advantage of saving gas. The lifetime of the gas can be compromised by contamination from microscopic leaks. One way to avoid the gas deterioration is the use of a purifying system, for example Getters, where some gas impurities can be adsorbed and the lifetime of the gas increases. In flow mode larger gas suppliers are needed. Usually the gas is vented to the atmosphere

when going out of the detector. This limits the type of gas used for economical and environmental reasons

Table 2. 1- Physical properties of gases at 20° C and 760 Torr [82].

Gas	Z	A	Density 10^{-3} (g/cm^3)	E_x (eV)	E_i (eV)	w_i (eV)	$[dE/dx]_{mip}$ (keV cm^{-1})	n_p (cm^{-1}) N.T.P	n_t (cm^{-1}) N.T.P.	Radiation Length (m)
He	2	2	0.178	19.8	24.5	41	0.32	4.2	8	745
Ar	18	39.9	1.782	11.6	15.7	26	2.44	23	94	110
Ne	10	20.2	0.90	16.67	21.56	36.3	1.56	12	43	345
Xe	54	131.3	5.86	8.4	12.1	22	6.76	44	307	15
CF_4	42	88	3.93	12.5	15.9	54	7	51	100	92.4
DME	26	46	2.2	6.4	10.0	23.9	3.9	55	160	222
CO_2	22	44	1.98	5.2	13.7	33	3.01	35.5	91	183
CH_4	10	16	0.71	9.8	15.2	28	1.48	25	53	646
C_2H_6	18	30	1.34	8.7	11.7	27	1.15	41	111	340
i-C_4H_{10}	34	58	2.59	6.5	10.6	23	5.93	84	195	169

2.2.2 Diffusion

The radiation interaction in gaseous detectors trough ionization will produce a large number of low-energy electrons and ions. In absence of electric field, the charges will quickly achieve the thermal equilibrium with the gas assuming its thermal energy distributions. According to the kinetic theory of gases, the average value of the thermal energy is approximately 0,4 eV (3/2 kT) at room temperature assuming, a Maxwellian probability distribution of the energies [13]:

$$F(E) = C\sqrt{E}e^{-E/kT} \quad (2.\ 18)$$

being E the energy, T the temperature in Kelvin, k the Boltzman constant factor and C a probability constant. The average thermal velocity of electrons is about 10^7 cm/s, and of the order of 10^4 cm/s for positive ions [14].

The charged particles resulting from the ionising interaction move about at random, continuously colliding and exchanging momentum, following a Gaussian law [13] .

$$\frac{dn}{n} = \frac{1}{\sqrt{4\pi Dt}} e^{-x^2/4Dt} dx \quad (2.\ 19)$$

Where dn/n is the fraction of charges found in the element dx at a distance x from the origin after a time t and D is the diffusion coefficient.

If the density, *n*, (number of particles per unit volume) is not uniform, the particles from the regions with higher concentration will transfer more momentum in direction of the region with lower concentration. As result a net force

will drive the particles to the regions of lower concentration, with flow of j particles per second across unit area, described by [15]:

$$j = D \bullet gradn \quad (2.\ 20)$$

The electrons, due to their much smaller mass and consequent larger random velocity have diffusion coefficient orders of magnitude larger than ions. The diffusion coefficients D can be derived from the kinetic theory of gases for ions and electrons moving in their own gas [15]:

$$D_{ions} = \frac{1}{3}\lambda_i \upsilon_i \ ((2.\ 21)$$

$$D_{electrons} = \frac{1}{3}\lambda_e \upsilon_e \ (2.\ 22)$$

Were υ is the velocity and λ the mean free path. In the diffusion process, the average mean free path is given by:

$$\lambda = \frac{1}{N\sigma(E)} \quad (2.\ 23)$$

were σ(E) is the energy dependent collision cross section deduced from the Ramsauer of the gas considered and N the number of molecules per unit of volume. At the temperature T and pressure P, N is given

$$N = 2.69 \times 10^{19} \frac{P}{760} \frac{273}{T} molecules / cm^3 \quad (2.\ 24)$$

In the presence of electric field the diffusion process is no longer isotropic which means that a longitudinal component, D_L, and a transverse component, D_T, have to be considered in the diffusion coefficient.

During the diffusion process, ions and electrons can participate in different processes, such as charge transfer, recombination and attachment.

- **Charge transfer**: When a positive ion comes upon to a neutral gas molecule, an electron is transferred from the neutral molecule to the positive ion, reversing the role of each particle. This phenomenon is more important in gas mixtures with different types of molecules, where there is a tendency to transfer the net positive charge to the molecules with lower ionization energy.

- **Recombination:** Some collisions between positive ions and free electrons can result in recombination, being the electron captured by the

positive ion, the latter returning to a neutral charge state. Another recombination process, which is more probable, involves a collision between molecular ions and electrons. This results in the dissociation of the molecule leaving a neutral atom and an excited atom to share the excess of kinetic energy.

- **Attachment:** Some types of gases exhibit a natural tendency to form negative ions by the attachment of the free electron to a neutral gas molecule. The negative ion then shares several properties with the original positive ion, created in the ionization process, but with opposite electric charge. The attachment rate is significant in oxygen and in air since free electrons diffusing in air are quickly converted into negative ions. In opposite, nitrogen, hydrogen, hydrocarbon gases and noble gases are characterised by relative low electron attachment coefficients.

2.2.3 Drift

In the absence of the electrical field the electron-ion pairs created in a gas medium by incident radiation have natural tendency to recombine forming neutral atoms. Under the application of an external electrical field, the resultant electrostatic forces will impose a specific charge flow. The net motion is a superposition of a random thermal velocity and a net drift velocity. The ions move in the electrical field direction, while the electrons move in opposite direction. The drift velocity, v, can be predicted from the relation:

$$v = \frac{\mu}{p} E \quad (2.\ 25)$$

being μ the mobility of the charge particle, E the electric field intensity and p the gas pressures. The ions have mobility fairly constant over wide ranges of electric fields and gas pressure, with no significant differences for positive or negative ions in the same gas. In opposite, the electrons do not have a constant mobility, so its drift velocity has to be measured for different electric field values.

IONS

A cloud of ions under the influence of an electric field will move in the field direction. The average velocity of this slow motion is called the drift velocity,

w^+, which is linearly dependent on the reduced electric field, E/p, up to very high fields. The drift velocity is related to the ion mobility by the follow equation:

$$\mu^+ = \frac{w^+}{E} \quad (2.\ 26)$$

The ion mobility is a characteristic of each ion in a specific gas. The average energy of the ions remains practically constant during the drift, leading to a constant mobility. The Einstein relation correlates the diffusion constant D^+ with the ion mobility if a thermal equilibrium is reached:

$$\frac{D^+}{\mu^+} = \frac{kT}{e} \quad (2.\ 27)$$

The ions moving in a time interval t will diffuse with a probability distribution expressed by the Gaussian law, as explained before, with a standard deviation σ_x given by the equation:

$$\sigma_x = \sqrt{\frac{2kT}{e}\frac{x}{E}} \quad (2.\ 28)$$

Therefore the r.m.s. linear diffusion is independent of the nature of the ions and the gas. Considering the collection of all ions after a drift length x, the time spread, σ_t depends on the ion mobility and thus on the type of ion and the neutral gas, being expressed by the following relation:

$$\sigma_t = \frac{\sigma_x}{w_+} = \sqrt{\frac{2kT}{eu_+^2}\frac{x}{E^3}} \quad (2.\ 29)$$

For a mixture of n different gases, the mobility μ_i^+ of the ion G_i^+ is given by the Blanc's law:

$$\frac{1}{u_i^+} = \sum_{j=1}^{n} \frac{p_j}{u_{ij}^+} \quad (2.\ 30)$$

where p_j is the volume concentration of gas j in the mixture, and u_{ij}^+ the mobility of ion G_i^+ in gas G_j.

Table 2.2 represents the measured values for the mobility of several ions drifting in gases commonly used in gas detector applications.

Table 2. 2: Measured values for the mean free path λ, the diffusion coefficient D and ion mobility μ in different gases [13].

Gas	λ (x10^{-5} cm)	D (cm^2/s)	μ ($cm^2s^{-1}V^{-1}$)
H_2	1.8	0.34	13
He	2.8	0.26	10.2
Ar	1	0.04	1.7
O_2	1	0.06	2.2
H_2O	1	0.02	0.7

ELECTRONS

A cloud of electrons moves in random directions trough the gas. Under the application of an electric field, the centre of the cloud exhibits a slow drift with direction opposite to the field.

The average drift velocity can be derived in first approximation calculating the momentum, in the field direction, achieved by an electron moving along a free path, assuming that the entire momentum is spent in a collision. Since the mean free path is inversely proportional to the gas pressure p, and the electron energy is a function of the reduced field E/p, the drift velocity is also a function of E/p:

$$w = C.\frac{e\lambda_e .E}{mv_r} \propto \frac{E}{p} \text{ (2. 31)}$$

being C a numerical constant between 2/3 and 1 and λ_e the electron mean free path, which is related with the electron mobility, μ_e,

$$\mu_e = C\frac{e\lambda_e}{mv_r} \text{ (2. 32)}$$

The standard deviation σ_x for electron diffusion along an x direction is described by a Guassian Law:

$$\sigma_x = \sqrt{\frac{2Dx}{w}} \text{ (2. 33)}$$

where D is the diffusion coefficient. This is applied only for moderate values of E/p, where one can assume that the electron energy remains practically constant as the electric field augments. The mean collision time is considered constant and the drift velocity increases linearly with the electric field according to:

$$eE\frac{D}{w} = kT \text{ (2. 34)}$$

The standard deviation for electron diffusion is then:

$$\sigma_x = \sqrt{\frac{2kTx}{eE}} \quad (2.\ 35)$$

This expression is often referred as the thermal limit to electron diffusion.

For high electron energies, the behaviour of the molecular cross-section is very different. In some gases the average energy remains thermal up to rather large fields, but there are other types of gases where a small electric field augment, a few V/cm.atm, induce a considerable increase of the electron energy. Thus, the drift velocity and diffusion can be very different in various gases at given values of electric field and pressure. As a result, an accurate knowledge of the electron energy distribution is required for the drift field calculation. This has been already considered by electron transport theories which take into account the field dependence on the increase of the average energy:

$$eE\frac{D}{w} = nkT = \varepsilon_k \quad (2.\ 36)$$

ε_k denotes characteristic energy, is dependent on the reduced field E/P and can be directly measured. The standard deviation can then be written as:

$$\sigma_x = \sqrt{\frac{2\varepsilon_k x}{eE}} = \sqrt{\frac{2\varepsilon_k}{eE/p}}\sqrt{\frac{x}{p}} \quad (2.\ 37)$$

It was assumed that the diffusion is uniform in all directions, which is not really true especially at high fields, and so the longitudinal and transverse diffusion, (D_L and D_T, respectively) should be considered

For a gas mixture the classic approach has some limitations. New mathematic formulation for transport theory is needed to accurately determine the gas mixtures parameters.

The electron drift is responsible for the gas electrical conductivity (σ). The contribution of positive ions can in general be ignored given their small drift velocity. The current density, j, is given by:

$$j=\sigma E \quad (2.\ 38)$$

$$j = new = \frac{ne^2\lambda_e}{mv_r}E \quad (2.\ 39)$$

where ν is the frequency at which electrons hit the gas molecules. The conductivity increases with the electrons concentration, and decreases with the

augment of gas pressure, since the number of obstacles also increase and the mean free path of electrons is lower.

2.3 Gas Amplification

The radiation interaction with the gas produces an average number of free electrons. These electrons constitute the primary electron cloud and travel through the gas under an external electric field with a drift velocity and a mean energy determined by the value of E/p. Given their spread of velocities, a fraction of the electrons acquire enough energy to take part in ionizing phenomena (collisions between the electrons and the atoms/molecules). The average number of ionizing collisions an electron undergoes per unit of drift length in the field direction is defined as the Townsend primary coefficient α. The average distance that an electron has to travel before an ionizing collision takes place is the mean free path for ionization λ. The Townsend coefficient is the inverse of the mean free path. For a given E/p value the mean electron energy is fixed and a constant ionization probability per collision is expected. The mean free path is inversely proportional to the gas pressure p, so the ionization probability will be proportional to α/p.

The collisional ionization is the basis of the avalanche multiplication in proportional counters. Considering an electron liberated in a region of uniform electric field, after a mean free path α^{-1} one electron-ion pair will be produced. The two electrons will continue the drift generating new ion-electron pairs and so on. Figure 2. 6 illustrate the Townsend avalanche process.

If n is the number of electrons at a given position, after a length dx, the increase in the number of electrons will be:

$$dn = n\alpha dx \quad (2.\ 40)$$

Integrating the previous equation:

$$n = n_0 e^{\alpha x} \quad (2.\ 41)$$

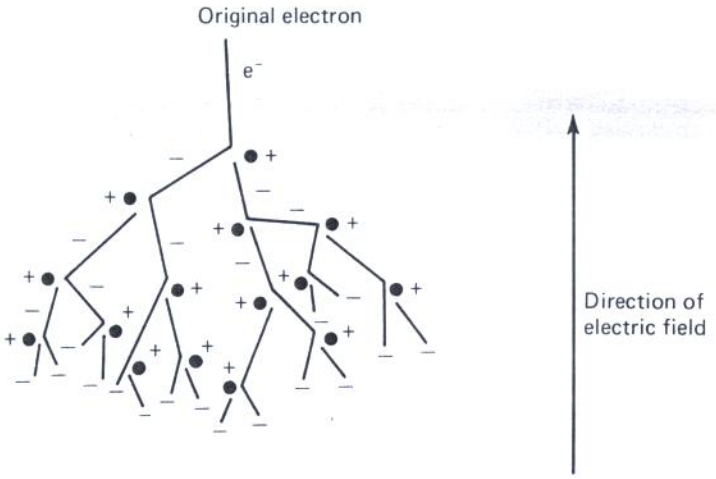

Figure 2. 6- Townsend avalanche process.

The multiplication factor is given by the relation between n, the number of electrons obtained in the ionizing process and n_0 the initial number of electron produced by the radiation interaction with the gas:

$$M = \frac{n}{n_0} = e^{\alpha x} \quad (2.\ 42)$$

For non-uniform electric fields, the Townsend coefficient should not be considered constant and a dependence on the electric field need to be taken into account, α=α(x). Knowing the Townsend coefficient dependence on electric field the multiplication factor can be calculated for any field geometry:

$$M = \exp\left[\int_{x_1}^{x_2} \alpha(x)dx\right] \quad (2.\ 43)$$

The behaviour of the first Townsend coefficient in gas mixtures does not follow a simple rule. As general trend, the addition of a polyatomic gas to a noble gas leads to an increase of the electric field value required for amplification.

The multiplication factor is limited by some effects like secondary processes. The secondary photon emission induces the generation of avalanches spread over the gas volume and space charge deformation of the electric field, which is strongly increased near the front of the avalanche, thus can result in a spark breakdown.

A phenomelogical limit for multiplication before breakdown is given by the Rather condition:

$$\alpha x \cong 20 \quad (2.\ 44)$$

The statistical energy distribution of the electrons does not allow values above the Rather limit if breakdown want to be avoid. Increasing the gap thickness x the Rather limit will be achieved at lower values of α. For a given field strength, the breakdown probability increases with the gap thickness.

An interesting aspect of avalanche is its geometric progression, which assumes the shape of a liquid drop due to the large difference between the drift velocities of electrons and ions, Figure 2. 7. The electrons, lighter than ions, move faster and leave behind a long tail of positive ions drifting slowly towards the cathode. There is a time delay between the initial creation of ion-electron pairs and the formation of the droplet.

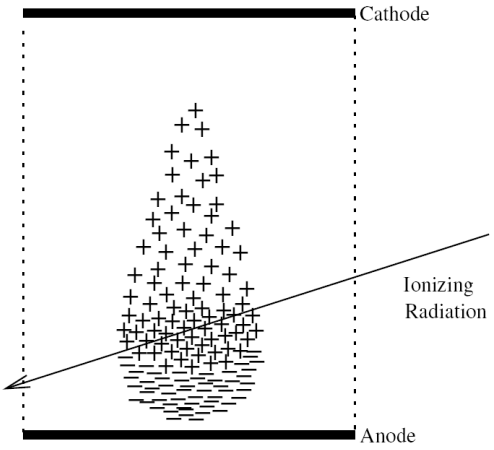

Figure 2. 7- Typical droplet shape of the avalanche in a gas filled detector [16].

2.3.1 Operation Regimes

The gas detectors can be classified according to their voltage region operation. Figure 2. 8 show the relation between the applied voltage region and the type of detector suitable for each operation regime.

REGION I- RECOMBINATION REGION

In this region, the electric field is very low so the electron- ion pair created will move with a slow speed with a significant recombination rate. An electric field augments leads to a decrease of the recombination rate, reaching zero at a certain point which corresponds to the transition for a next region. There is no counter operating in this region.

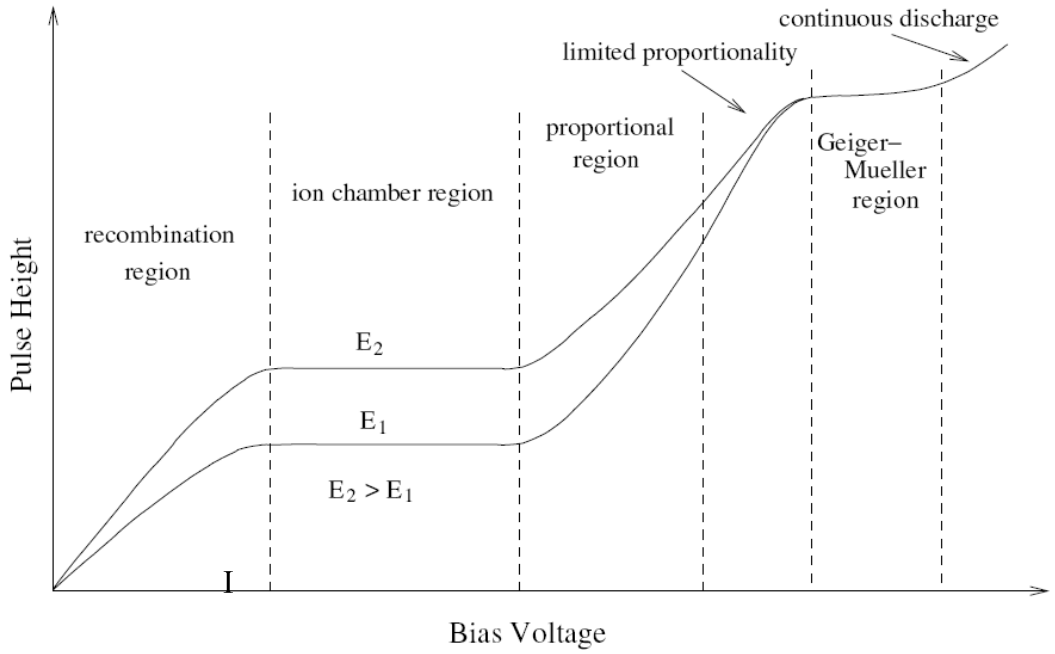

Figure 2. 8 – Variation of pulse height produced by different types of detectors with respect to applied voltage. The two curves correspond to two different energies of the incident radiation [12].

REGION II- IONIZATION REGION

In this region, the recombination rate is zero and all charges created by ionization are collected. There is no multiplication process, the output signal is proportional to the particle energy deposited in the detector. As a result, this region is suitable for particle energy measurements. For example, the photon flux absorbed in the gas.

The signal resulting from ionization is not very large, therefore only strongly ionizing particles, such as alphas, protons, fission fragments and other heavy ions can be detected.

The ionization chamber operates in this region.

REGION III- PROPORTIONAL REGION

The electric field in this region will be strong enough and so primary electrons obtain enough energy to produce additional ionization. The electrons liberated in these secondary ionizations can also acquire enough energy to induce further ionizations and so on, leading to an ionization avalanche. However, the output signal is still proportional to the energy dissipated in the detector. The

proportional counter operates in this region, being suitable for identification and energy measurement.

REGION IV- GEIGER- MULLER REGION

This region is characterized by strong electric field values so that single electron-pair created in the chamber is enough to initiate an avalanche of electron-ion pairs. This avalanche will produce further secondary avalanches until the local E field drops to values that disable additional charge multiplication. Due to positive charge accumulation in the gas volume a strong signal with a shape and height independent of the primary ionization and the type of particle is obtained. The signal depends only on the electronics, so the proportionality is lost.

This is the operation region of Geiger Muller detectors. These detectors are very useful given their simple operation and the very strong signal without pre-amplification. Geiger –Muller detectors can be used for all ionizing radiation types, different levels of efficiency to measure interaction rates. One of the disadvantages is the incapability to distinguish different types of particles. Since the output signal is independent of the particle type and energy, it only provides information about the number of particles.

REGION V- STREAMER REGION

In this region, a single ionizing event initiates a continues discharge in the gas and the device is not a particle detector anymore. No gas counter should operate in this region.

Chapter 3

Electric Field Simulation

In order to predict the electrical field behaviour in the GEM-MIGAS a detector 3D model was developed using the Maxwell Ansoft software [24]. Maxwell 3D simulator is an electromagnetic finite element method solver that can be used for electrostatic problems. It is a computerized solution process where users are only required to specify the geometry and boundary conditions, as well as select the materials properties. Then, a finite element mesh is automatically generated, which can be refined, and the problem is solved to a defined precision error.

A three-dimensional electric field simulation of a GEM-MIGAS detector was performed in order to evaluate the electric field profile in the different regions of the structure. Different electrostatic conditions were undertaken to forecast the detector performance in gas medium

3.1 The Model

The model geometry is depicted in Figure 3. 1 and is based on standard GEM dimensions: a 50 μm Kapton substrate with 5 μm thick copper clad on both sides, bi-conical holes with a diameter of 50 μm in the Kapton and 70 μm in the copper, arranged in a hexagonal lattice with 140 μm pitch. The micro–induction gap was initially set at 50 μm, and after was extended to values between 50 to 300 μm .The drift region thickness was set at 200 μm.

The default mesh created by Maxwell was refined in order to improve the solution accuracy. The mesh used is shown in Figure 3. 1.

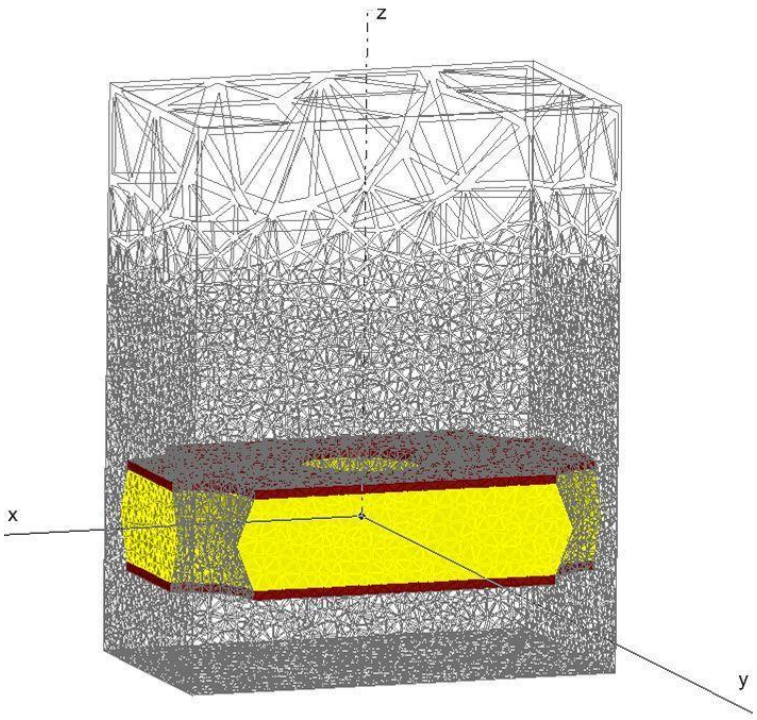

Figure 3. 1- Scheme of the GEM-MIGAS model used for the electric field simulation with the Maxweel 3 D. Mesh used in GEM-MIGAS simulation, manually refined.

3.2 Electric field strength

The first GEM-MIGAS archetype was proposed with an induction region length of 50 μm. This Maxwell 3D model was subject of a more detailed study.

The evaluation of the electric field profile in GEM-MIGAS focus essentially two aspects: simulation of GEM voltage for fixed induction field values and the effect of the induction field for fixed GEM voltages.

The electric field strength was computed along the GEM hole axis (coordinate z, where z =0 corresponds to the centre of the hole), for induction fields E_{ind} in the range 0-100 kV/cm and for different GEM voltages. The drift field E_{drift} was kept at 0.25 kV/cm for all simulations.

3.2.1 50 μm Induction region gap

The electric field behaviour along the GEM hole axis is depicted in Figure 3. 2 as a function of z, for E_{ind} values in the range 0 - 100 kV/cm and for fixed V_{GEM} of 100, 300 and 500 V, respectively in figures a, b and c. A typical 50 μm induction region was considered. The graphs show that, for a fixed GEM voltage, as E_{ind} increases, the maximum electric field strength gradually moves from the hole centre towards the induction region. The maximum electric field value is

reached out of the GEM hole for E_{ind} around 20, 50 and 80 kV/cm for V_{GEM} values of 100, 300 and 500 V, respectively. For high V_{GEM} and low E_{ind} values, the maximum electric field occurs in the channel, so the channel plays the more important role in the charge multiplication process. On the other hand, for low V_{GEM} and high E_{ind} values, the induction gap has the main role in the multiplication process.

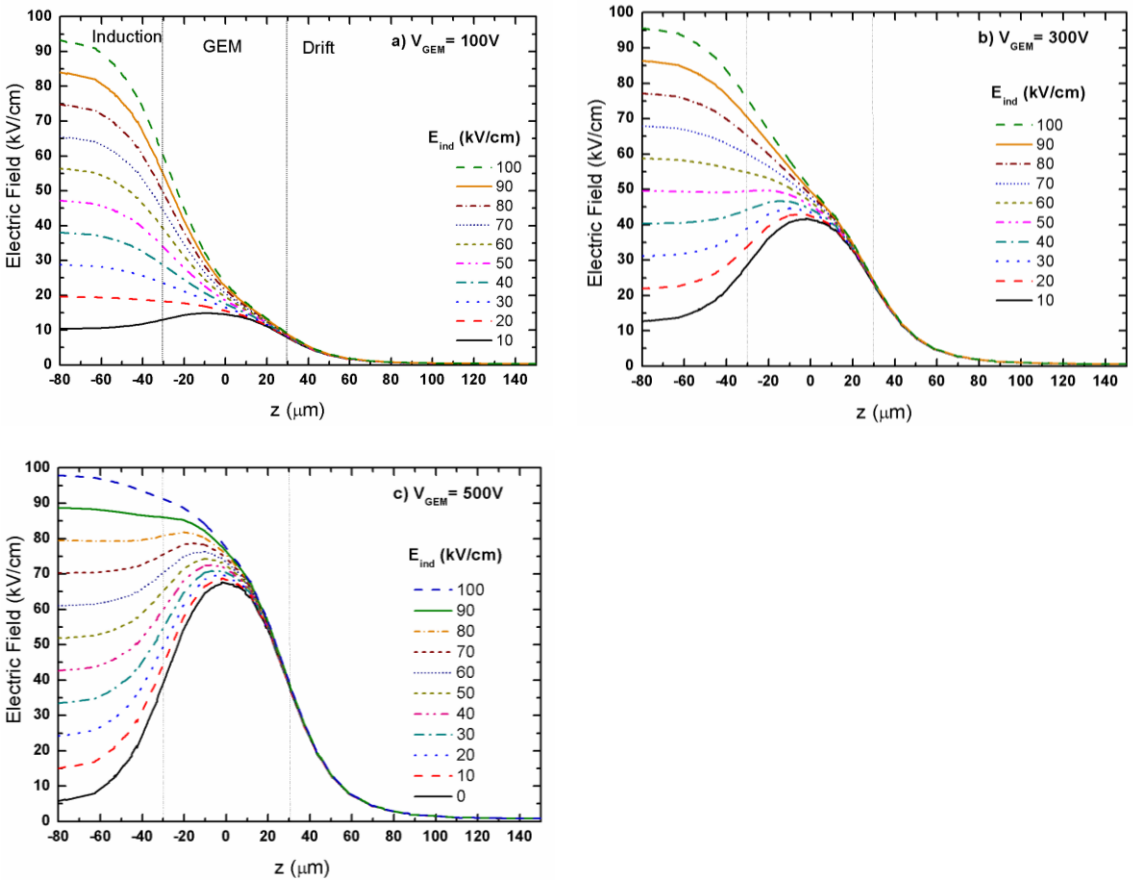

Figure 3. 2- – Electric field strength along the axis of a GEM hole (coordinate z) for induction field values in the range 0-100 kV/cm and for GEM voltages of: a) 100 V, b) 300 V, c) 500 V. The vertical lines indicate the different regions of GEM-MIGAS structure, with 50 μm induction region gap

Figure 3. 3 depicts the electric field strength along the axis of the GEM hole for V_{GEM} values in the range 0-500 V and E_{ind} values of 10, 20, 60 and 80 kV/cm. For low values of the ratio between V_{GEM} and E_{ind}, the electric field has a smooth variation along z, and the maximum value of the electric field is obtained in the induction plane, the induction gap plays the more important role in the multiplication process.

For higher V_{GEM} values, e.g. above 50, 100, 300 and 400 V for E_{ind} values of 10, 20, 60 and 80 kV/cm, respectively, curves start to exhibit a peaked behaviour, where the maximum electric field value is achieved within the GEM holes. It is

evident that, for high values of the ratio between V_{GEM} and E_{ind}, the GEM channel has the more important role in the charge multiplication process. The particular conditions for which the electric field (along the axis of the hole) in the induction gap is approximately uniform were found for V_{GEM} values of about 50, 100, 400 and 500 V for E_{ind} values of 10, 20, 40 and 60 kV/cm, respectively.

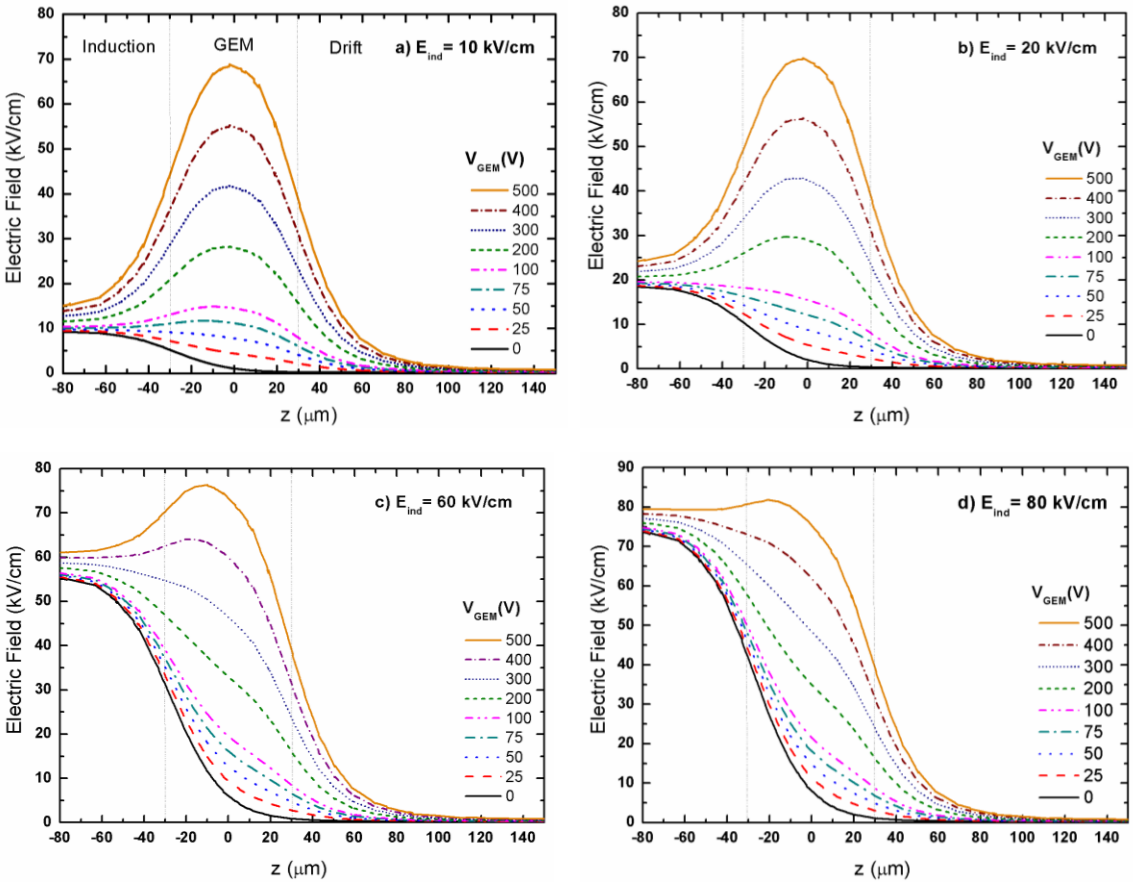

Figure 3. 3- Electric field strength along the axis of the GEM hole (coordinate z) for V_{GEM} values in the range 0-500 V and for E_{ind} values of: a) 10 kV/cm, b) 20 kV/cm, c) 60 kV/cm, d) 80 kV/cm. The vertical lines indicate the different regions of the GEM-MIGAS structure.

3.2.2 100 μm Induction region gap

The electric field behaviour for GEM-MIGAS with a 100 μm thick on the induction region is depicted in Figure 3. 4 for V_{GEM} values in the range 0-500V and E_{ind} values of 10, 20, 60 and 80 kV/cm.

For the lowest E_{ind} configuration, 10kV/cm (a), the electric field has a peaked behaviour for V_{GEM} values above 50 V and the maximum electric field value occurs at z=0 i.e. in the center of the GEM hole. Increasing the induction field to 20 kV/cm, (b), the peaked behaviour stills exists but now for a V_{GEM} value

above 100 V. The position of the maximum field value has a slight shift to the induction region compared to the 10kV/cm situation.

It is evident that the minimal GEM voltages necessary to observe a peaked behaviour increase with E_{ind}, being about 300 and 400V for E_{ind} values of 40 and 60 kV/cm, respectively. For lower voltages, the maximum electric field value occurs in the induction region. For higher E_{ind} values, a slight shift of the position of the maximum electric field is observed towards the induction region.

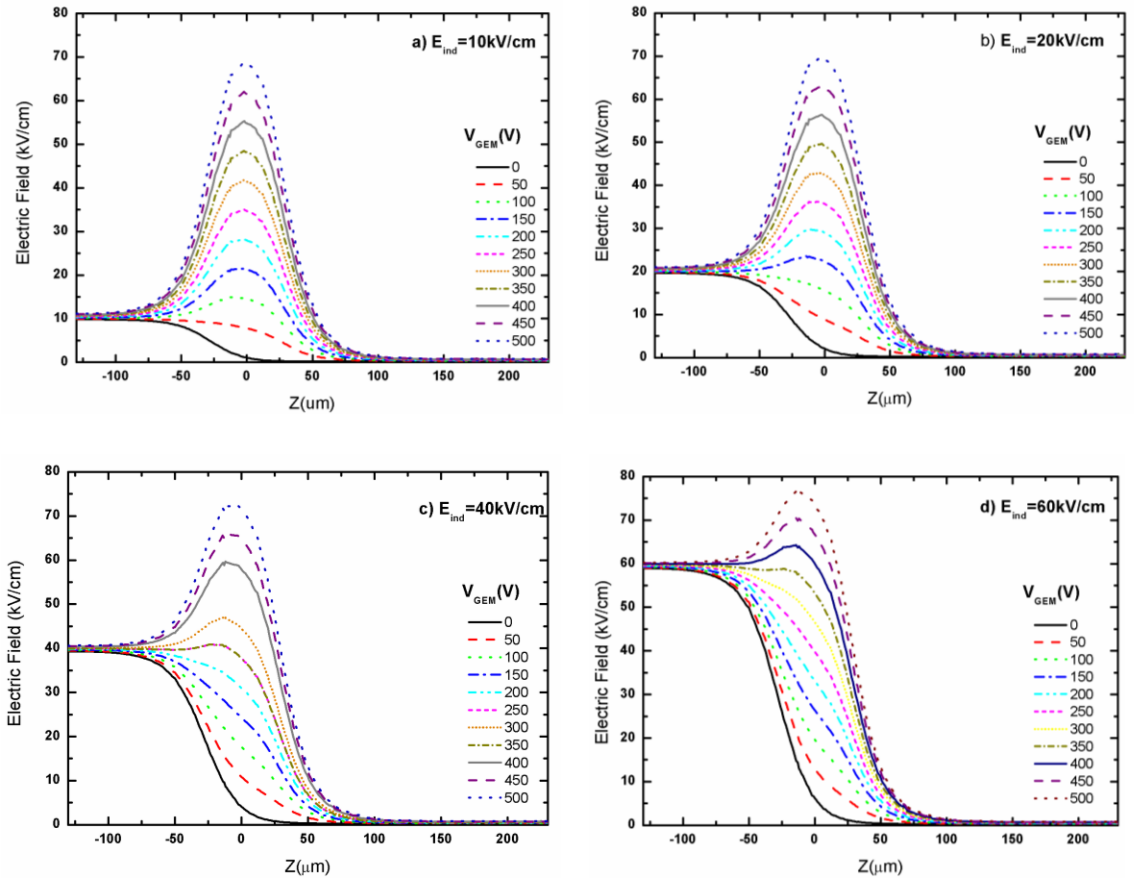

Figure 3. 4- Electric field strength along the axis of the GEM hole (coordinate z) for V_{GEM} values in the range 0-500 V and for E_{ind} values of: a) 10 kV/cm, b) 20 kV/cm, c) 40 kV/cm, d) 60 kV/cm. A 100 μm induction region gap was considered.

3.2.3 200 μm Induction region gap

The electric field behaviour obtained for the 200 μm gap configuration is depicted in Figure 3. 5 for V_{GEM} values between 0 to 500V and E_{ind} values of 10, 20, 40, 60 kV/cm (figure a, b, c and d respectively).

The electric field behaviour is similar to the one described for previous GEM-MIGAS configurations. The electric field curve has a peaked behaviour, achieving its maximum value in the GEM hole, for V_{GEM} values above 50, 100, 300

and 400 V for E_{ind} values of 10, 20, 60 and 80 kV/cm, respectively. The position of the maximum electric field value shifts to the induction region as E_{ind} increases. For low V_{GEM} the electric field has a smooth variation along z, and the maximum value of the electric field is obtained on the induction plane.

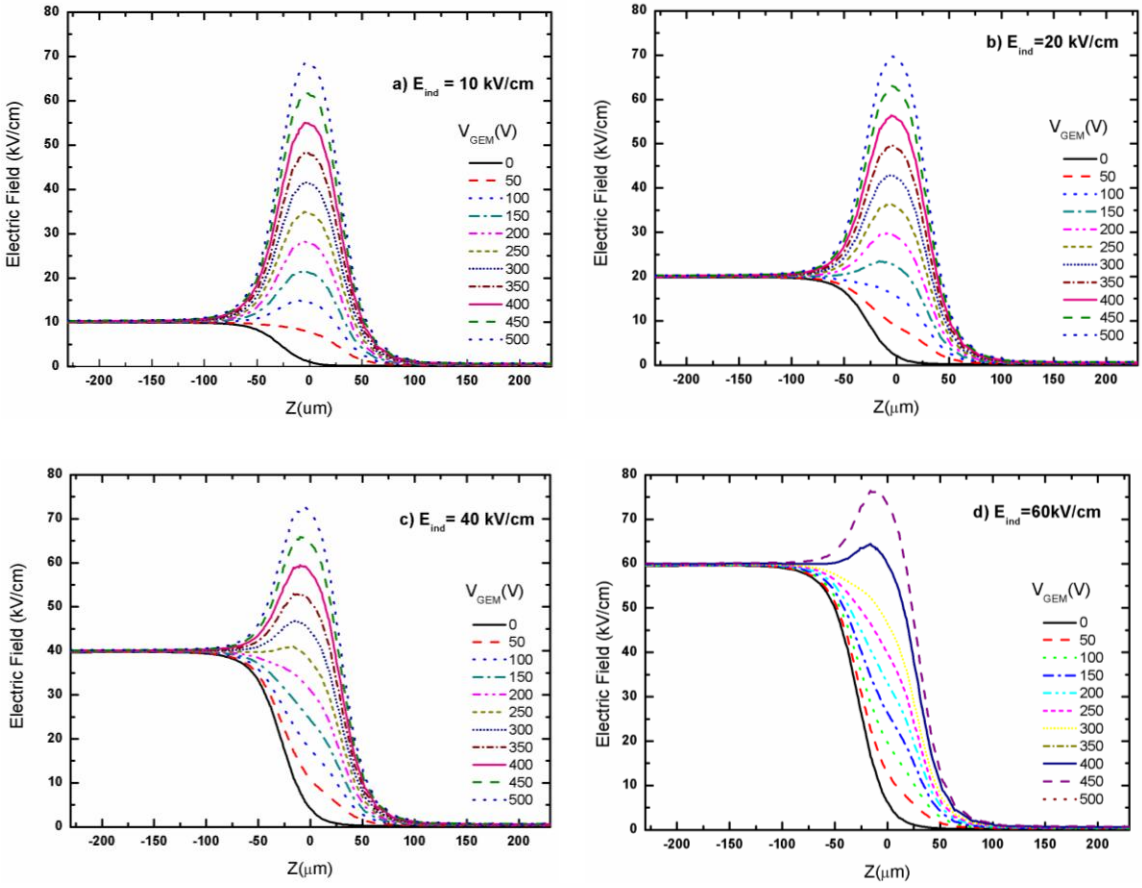

Figure 3. 5- Electric field strength along the axis of the GEM hole (coordinate z) for V_{GEM} values in the range 0-500 V and for E_{ind} values of: a) 10 kV/cm, b) 20 kV/cm, c) 40 kV/cm, d) 60 kV/cm. A 200 μm induction region gap was considered

3.2.4 250 μm Induction region gap

Figure 3. 6 depict the electric field behaviour computed for the 250 μm GEM-MIGAS, for E_{ind} values of 10, 20, 40 and 60kV/cm and V_{GEM} in the range 0-500V.

The electric field behaviour is in agreement with the behaviour observed for the low gap configurations. The peaked behaviour on the electric field curve occurs for V_{GEM} values above 50, 100, 300 and 400 V for E_{ind} of 10, 20, 60 and 80 kV/cm, respectively, where the maximum electric field occurs in the GEM hole. For the opposite conditions, i.e V_{GEM} bellows 50, 100, 300 and 400 V for E_{ind} of 10, 20, 60 and 80 kV/cm, respectively, maximum electric field value occurs in the induction region.

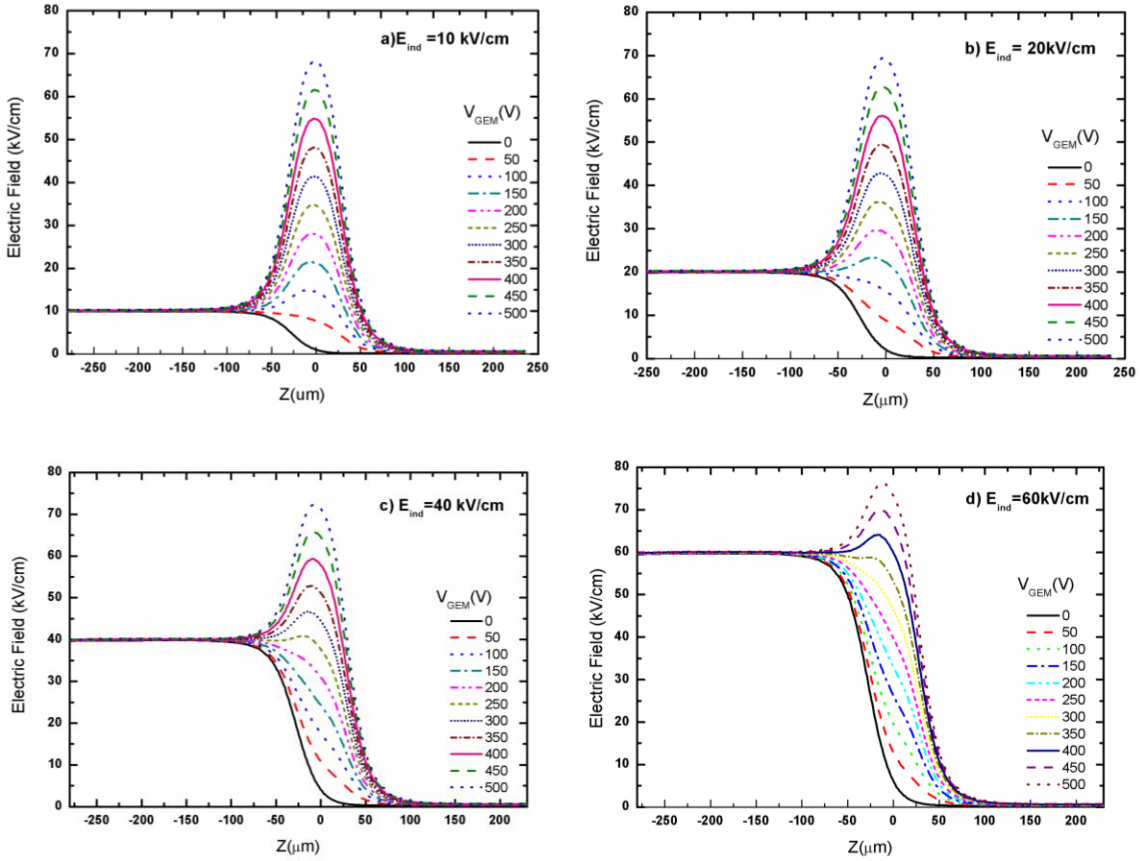

Figure 3. 6- Electric field strength along the axis of the GEM hole (coordinate z) for V_{GEM} values in the range 0-500 V and for E_{ind} values of: a) 10 kV/cm, b) 20 kV/cm, c) 40 kV/cm and d) 60 kV/cm. A 250 μm induction region gap was considered

3.2.5 300 μm Induction region gap

The highest GEM-MIGAS gap evaluated was 300 μm. The electric field behaviour is depicted in Figure 3. 7 for E_{ind} values of 10, 20, 40 and 60kV/cm with V_{GEM} values in the range 0-500 V. The electric field profile follow the behaviour described for the other induction region gaps. As the induction field increases the Gaussian behaviour is less significant and the position of the maximum field value deviates gradually to the induction region.

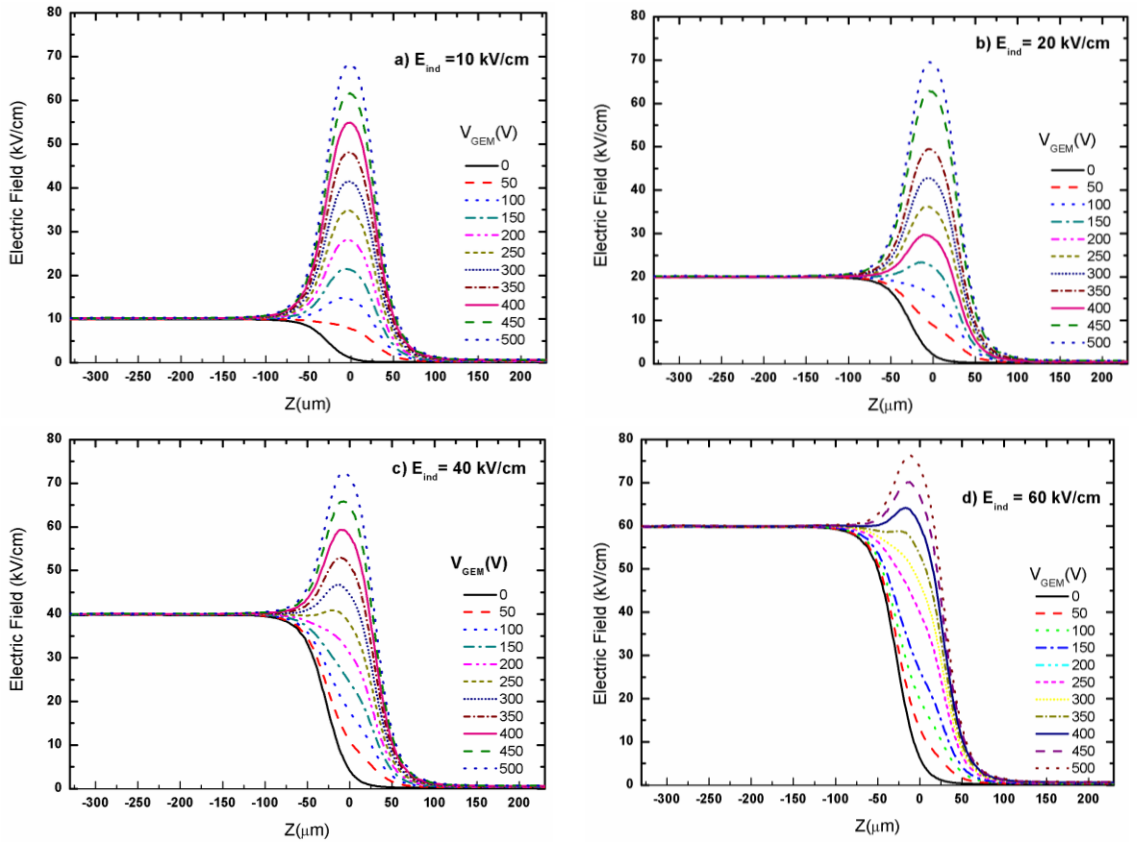

Figure 3. 7- Electric field strength along the axis of the GEM hole (coordinate z) for V_{GEM} values in the range 0-500 V and for E_{ind} values of: a) 10 kV/cm, b) 20 kV/cm, c) 40 kV/cm and d) 60 kV/cm. A 300 μm induction region gap was considered

3.2.6 Synthesis

The electric field profiles depicted for the different induction region thicknesses have a similar behaviour. Figure 3. 8 depict the electric field behaviour in GEM-MIGAS models with different induction region dimensions: 50, 100, 200, 250 and 300 μm.

The electric field strength was computed along the axis of a GEM hole for a V_{GEM}=300 V and induction fields E_{ind} of 10, 20, 40 and 60 kV/cm. The drift field, E_{drift}, was kept at 0.25 kV/cm.

The electric field profile has approximately a Gaussian behaviour for the low induction field configurations, 10 and 20 kV/cm. Increasing the induction field value, the Gaussian behaviour is lost and, for 60 kV/cm the maximum field value is achieved in the induction region.

For low induction field values, the situation E_{ind}=10kV/cm fig. (a), the maximum electric field value occurs practically in the centre of the GEM hole. Increasing the induction field the position where the maximum electric field occurs is gradually shifted towards the induction region.

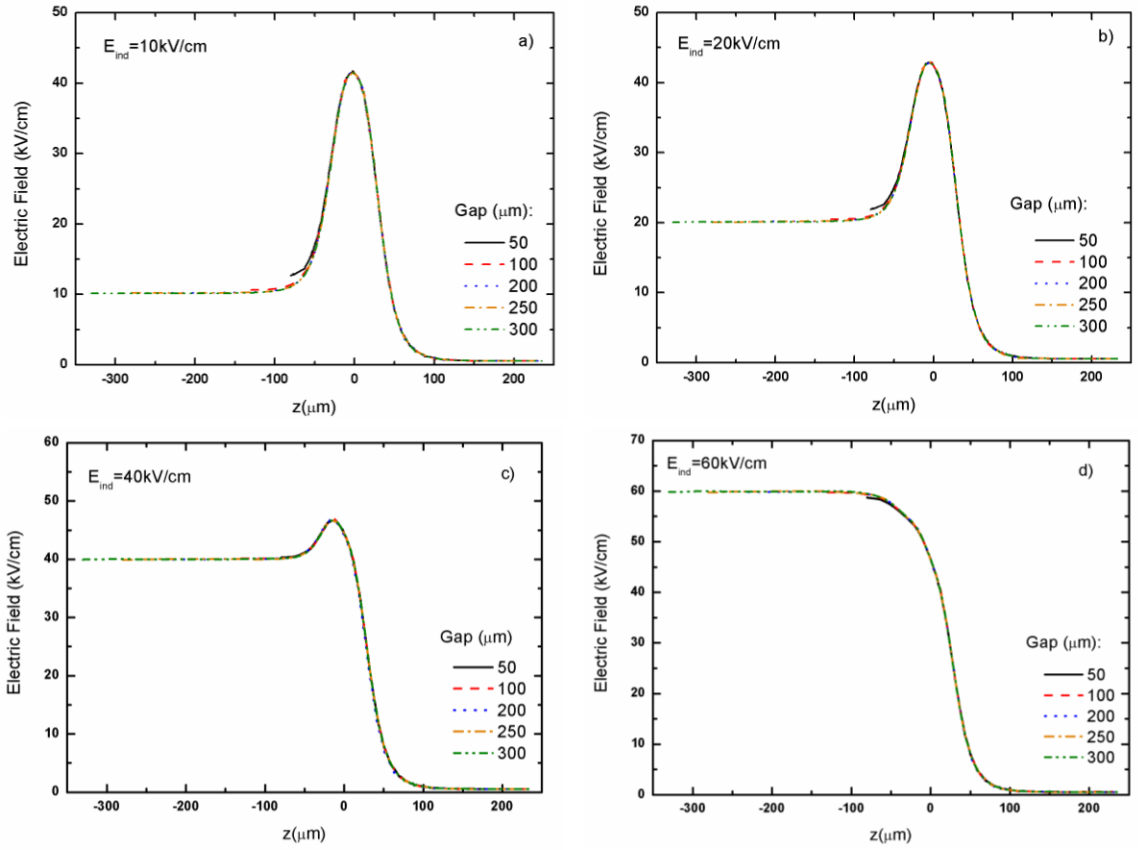

Figure 3. 8- Electric field strength along the axis of a GEM hole (coordinate z) for different induction regions and for E_{drift}=0.25 kV/cm, V_{GEM}= 300 V and induction field E_{ind}: a) 10 kV/cm, b) 20 kV/cm, c) 40 kV/cm and d) 60 kV/cm.

3.3 Electric Field Map

An electric field coloured map, having colours according its intensity, is a visual approach to represent the electric field behaviour, as some aspects are clearly illustrated. An electric field coloured map of GEM-MIGAS for a low induction field value of 5 kV/cm is represented in Figure 3. 9 while Figure 3. 10 represent the same map for a high induction field value of 40kV/cm. In both situations were used 100 and 400 volts across the GEM holes.

The 5kV/cm maps show that an increase of the GEM voltage influences the electric field in the induction region as well as in the drift region. It is observed an augment of the field intensity for V_{GEM}=400V. It's clear the penetration effect of high electric field from the holes in the induction region. At lower V_{GEM} values the influence of GEM voltage in the induction region is very smooth or even absent. The maximum electric field strength occurs inside the channel for both V_{GEM} values.

Analysing the 40kV/cm maps, Figure 3. 10, it is evident that the GEM voltage does not have a big influence on the induction field intensity contrasting to what was observed for E_{ind}= 5kV/cm. The difference of field intensity between the induction region and the GEM hole is not evident for the two different GEM voltages.

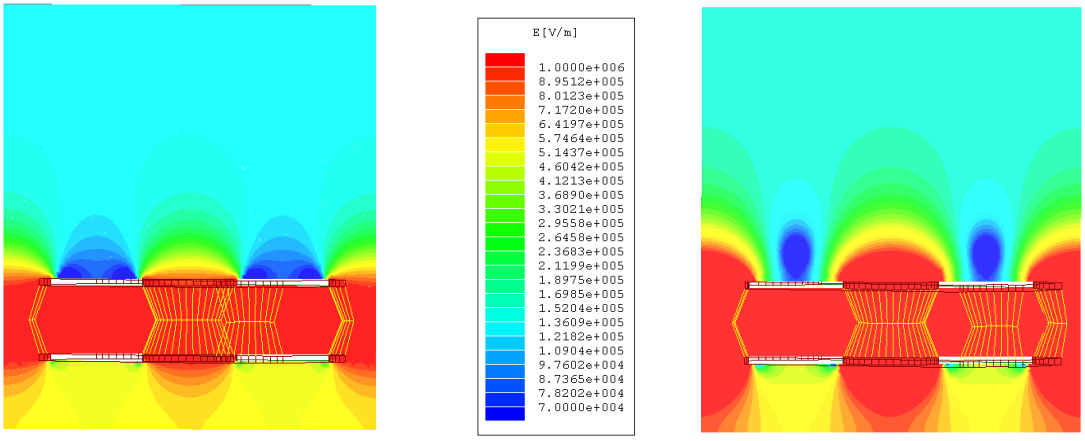

Figure 3. 9- Electric field color map of GEM-MIGAS for an induction field of 5kV/cm and V_{GEM} values of a) 100 V and b) 400V. The scale color represents the electric field intensity

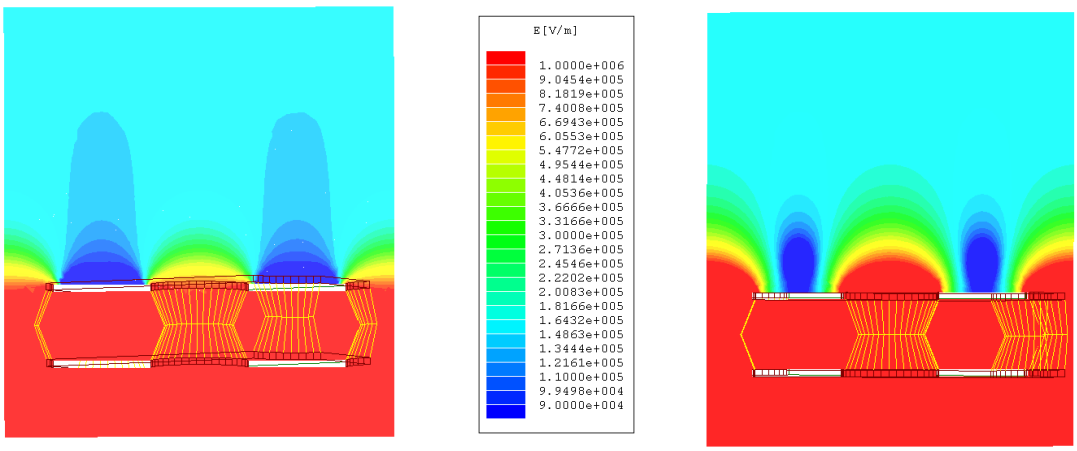

Figure 3. 10 - Electric field color map of GEM-MIGAS for an induction field of 40kV/cm and V_{GEM} of a) 100 V and b) 400V. The scale color represents the electric field intensity.

The electric field frontier lines were represented for the previous situations. These lines indicate the electric field boundaries along the GEM-MIGAS structure. The 5kV/cm induction field case is illustrated in Figure 3. 11 for V_{GEM} values of 100 and 400V, a) and b), respectively. The number of lines directed to the induction region is more significant V_{GEM} voltage of 400V, while for V_{GEM}=100 V a significant part of them are redirected to the bottom GEM electrode. For the E_{ind}= 40kV/cm case, Figure 3. 12 , the electric field in the induction region is practically constant and for that reason there are no lines in the induction region.

As a conclusion, for a low induction fields, the voltage across the GEM has more influence on the induction electric field intensity. For higher induction fields the influence of the GEM voltage is practically negligible and the induction field profile is mainly controlled by the induction field value. For V_{GEM}=100V the increase on E_{ind} from 5 to 40kV/cm leads to a considerable change of the electric field profile.

The induction field also affects the drift field profile, which can be observed comparing the figures of different E_{ind} values for a fixed GEM value, Figure 3. 11 and Figure 3. 12.

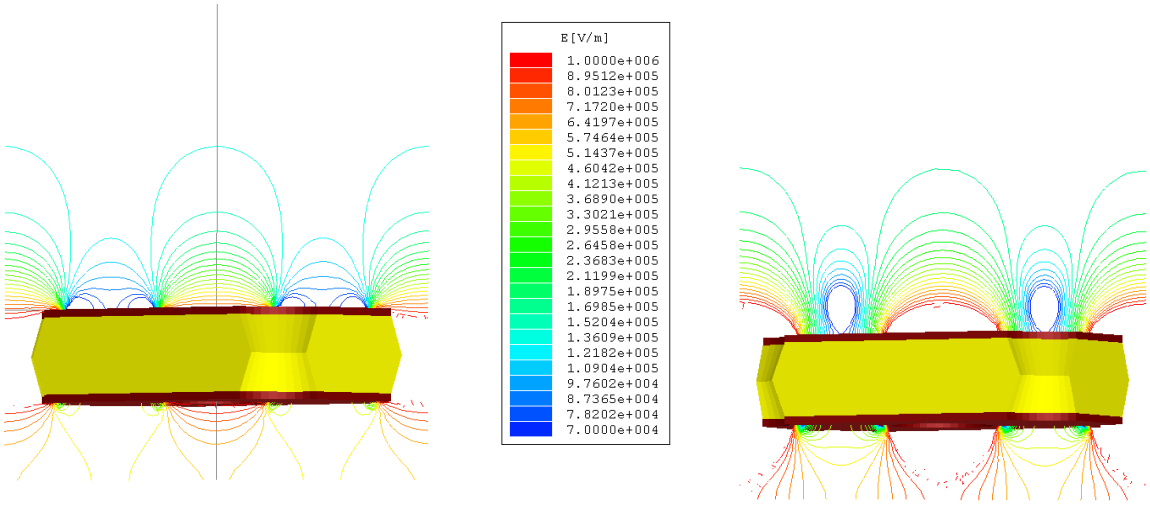

Figure 3. 11- Electric field map of GEM-MIGAS for an induction field of 5kV/cm, and V_{GEM} values of a) 100 V and b) 400V. The scale color represents the electric field intensity.

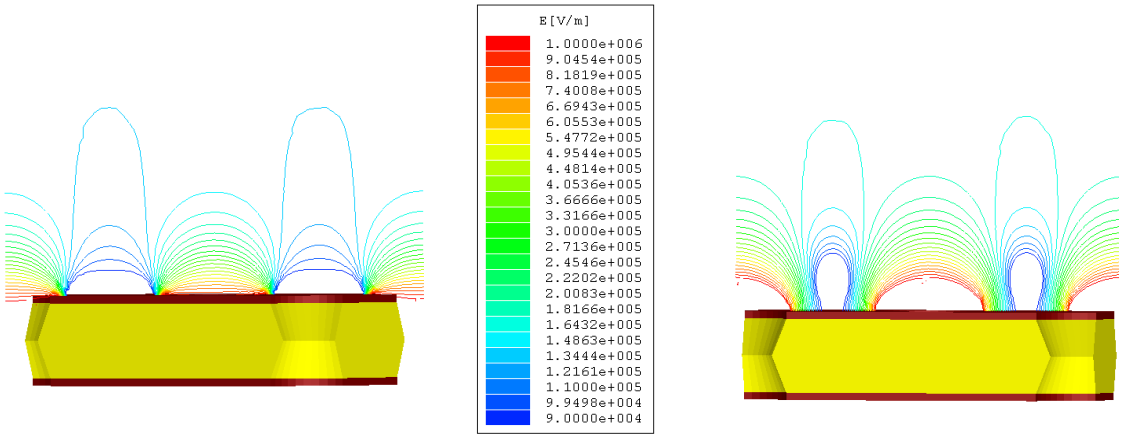

Figure 3. 12- Electric field map obtained for an induction field of 40kV/cm, and V_{GEM} of a) 100 V and b) 400V. The scale color represents the electric field intensity.

The electric field vectors were also represented for the same situations reported before, induction fields of 5 and 40kV/cm Figure 3. 13- and Figure 3. 14-,

respectively. Figure 3. 14- shows that high E_{ind} fields allow the defocusing of the field lines into the holes. Therefore, the representation of the electric field vectors is useful to support the ion back-flow (IBF) measurement that will be the subject of chapter 5. Since ions follow the electric field vector and electrons drift in the opposite direction, this representation is helpful to predict the ion back flow results.

It is clear that for higher induction fields all vectors are directed to the induction plane. This is an advantage for the electron collection efficiency since the majority of the electrons will achieve the induction plane. For lower induction fields the behaviour is different since a few vectors are not pointed to the induction plane but to the bottom GEM electrode, which decreases the collection efficiency in the induction plane, when compared to higher induction field values. In addition, low induction fields lead to an increasing focusing of the field lines into the holes, increasing the transport of the positive ions produced in this region into the holes.

In the lower E_{ind} the V_{GEM} effect is considerably, looking to the figures is evident a change on the vectors direction in the different situations.

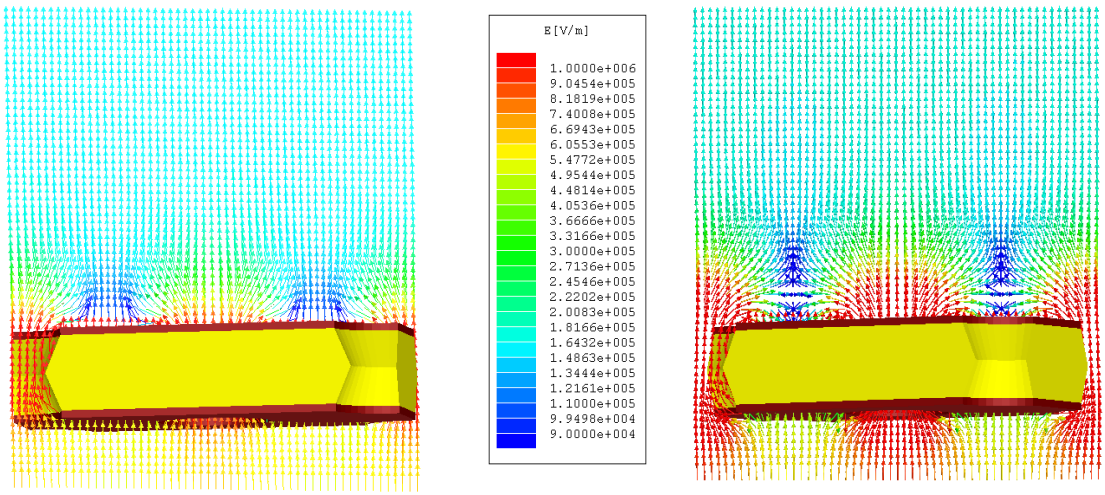

Figure 3. 13- Electric field vector map for induction field of 5kV/cm, for a V_{GEM} of a) 100 V and b) 400V.

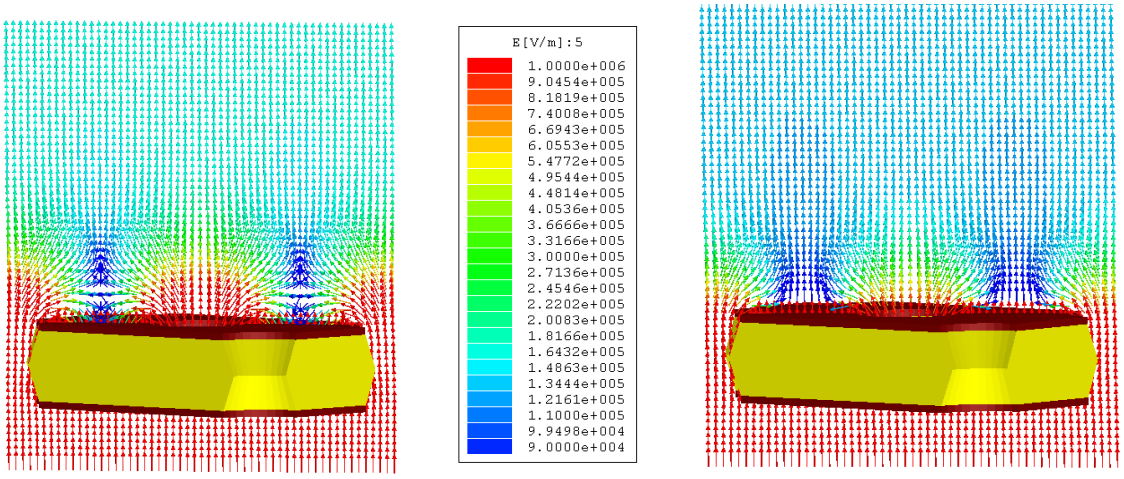

Figure 3. 14- Electric field vector map for induction field of 40kV/cm, for a V_{GEM} of a) 100 V and b) 400V.

3.4 Conclusions

These electric field maps were obtained for the 50 μm GEM-MIGAS model. The difference to the other models is only for the induction region thickness, so the aspects analysed are very similar for all GEM-MIGAS models.

The simulation results are valuable for a first approach to charge multiplication process localization in-between the two amplification regions. This helps to set the electric field values in GEM-MIGAS in order to guarantee a stable operation of the detector through the control of potential secondary effects in the different gas mixtures, resulting in high performance in terms of charge gain and stability.

The electric field vectors representation is useful for the ion-back flow performance. Forecast the electron and ion paths are an advantage on the IBF optimization. Of course, diffusion and drift effects, specific for each gas, need to be taken into account.

Chapter 4

GEM-MIGAS operation in Argon-Methane mixtures

This chapter describes an experimental study of a GEM-MIGAS detector with a standard 50μm induction gap operating in Ar/CH_4 (90/10%) gas mixture, pure CH_4 and Ar. The performance characteristics include the charge gain and the energy resolution for 5.9 keV X-ray, evaluated as a function of induction field and the GEM voltage.

4.1 Introduction

The GEM-MIGAS operation combines the charge amplification properties of GEM [11] and Micromegas [9] in a single device. This results in elevated charge gains, more efficient charge extraction from the GEM-holes and more efficient charge collection by the anode readout. The lower operational voltages in the GEM minimize the sparks rate allowing a longer lifetime of the device.

Studies with GEM-MIGAS in Ar/iso-C_4H_{10} (75/25%) and He/iso-C_4H_{10} (75/25%) penning gas mixtures, performed with 5.9 keV X-rays [25][26], have demonstrated charge gains of about 2×10^4 and 10^5, respectively. The best energy resolution obtained was around 20% and 30%, respectively. The charge multiplication in the induction gap resulted in a gain increase up of 4 to 5 times relative to GEM-mode operation. The response to single-electrons of a GEM-MIGAS in He/iso-C_4H_{10} (85/15%) revealed a charge gain improvement of about 10 times when compared to GEM-mode operation, reaching about 7×10^5 [27]. The good performance obtained in these studies motivated the evaluation of the GEM-MIGAS operation in other standard gases.

The GEM-MIGAS operation will be evaluated in a standard quenched gas mixture of Ar/CH_4 (90/10%), in pure CH_4 and in pure Ar. CH_4 has the advantage of presenting one of the highest photoelectron extraction efficiency, important for gaseous photomultipliers (GPMs) [28], while Ar is useful in

sealed chambers, e.g. for rare-event detection [29]. The performance characteristics include charge gain and energy resolution as a function of GEM voltage for different induction field values using a soft X-rays from a ^{55}Fe source (5.9 keV X-rays).

4.2 Experimental Setup

The experimental setup used for this investigation consists of a gas chamber, where the GEM-MIGAS is assembled, connected to the gas flux system and the electronic chain.

The gas chamber is made of aluminium, has a rectangular shape and a 5 mm diameter window on top made of a 25 μm mylar foil. Inside the chamber are placed 4 teflon pillars, in a square geometry, to support the frames containing the GEM-MIGAS structure as well as the grid frame to establish the drift region. Figure 4. 1 shows two photographs of the chamber used in this experimental work. The Figure 4. 1 a) is an outside view of the chamber, illustrating the window and the in/out connection for the gas flow. An inside view is depicted in Figure 4. 1 b with the GEM-MIGAS structure already assembled and BNC connectors to provide the electrical contacts.

The detector was operated with a constant gas flow rate at atmospheric pressure. Gas tightness is provided by Orings between the cap and the detector body.

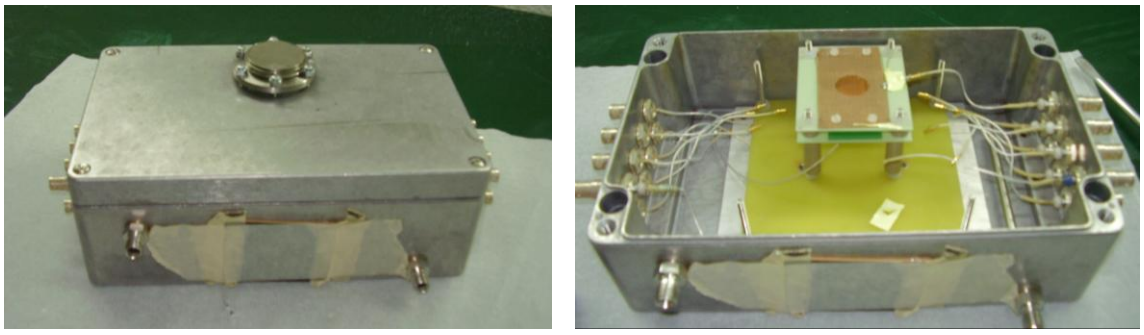

Figure 4. 1- Images of the gas chamber used in this experimental work. a) External b) Internal view.

The drift grid and the top and bottom GEM electrodes, were individually biased by HV power supplies from CAEN, model N471A with current limitation to 50 nA. The HV signal goes through a low pass RC filter before biasing the electrodes. Figure 4. 2 shows a schematic diagram of the GEM-MIGAS detector, with the RC filters used for each electrode.

The drift grid and the GEM electrodes were operated with negative voltage while the micromesh was at ground. The signals from the micromesh were fed

through a Canberra 2006 preamplifier with a sensitivity of 1.5 V/pC. The pre-amplifier output was fed into a Tennelec amplifier (model 243) with shaping time constants adjusted to 0.5 μs. The amplifier output was fed into a Nucleus PCA-II multichannel analyser with 1024 channels.

The HV power supplies, pre-amplifier and amplifier biased is provide by NIM-Bin(EG&G ORTEC).

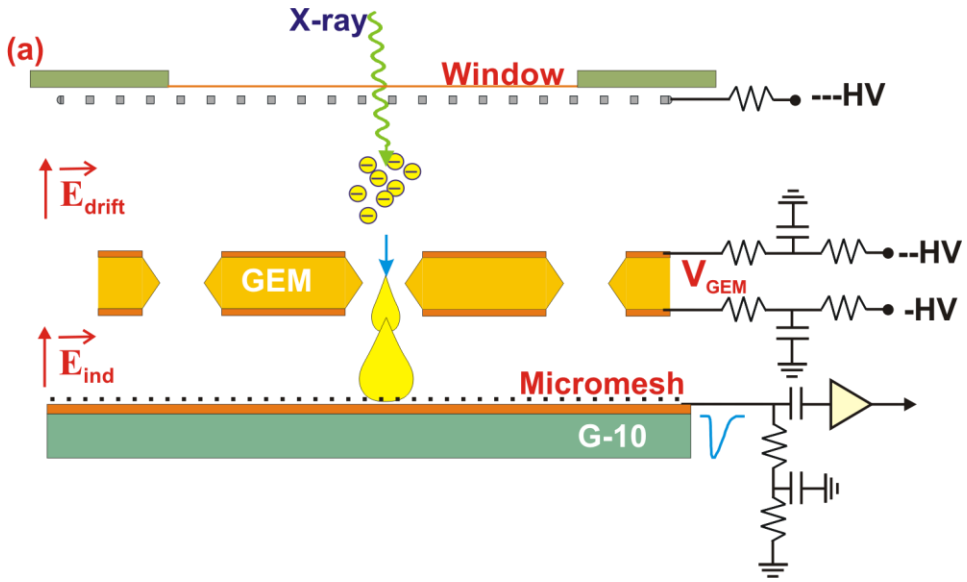

Figure 4. 2- Schematic diagram of the GEM-MIGAS detector, including the RC filters for each electrode.

The pre-amplifier converts the detector charge signal into a voltage signal, allowing the detector signals to be transmitted through long distances. The pre-amplifier works also as an impedance adaptor, since the signals are transmitted by coaxial cables which are characterized by low impedance. The pre-amplifier should be able to actuate over this low impedance without considerable signal losses.

The amplifier provides amplification and formats the signal from the pre-amplifier. The formatting consists of two sequential processes, differentiation and integration, resulting in an output voltage signal with amplitude proportional to the charge collected in the detector.

The low pass RC filters, used to limit the bias current in the presence of sparks, consist of a resistor in series with a capacitor Figure 4. 2. The components used were R=20 Ω resistance and C=10 nF capacitor.

4.2.1 Electronic Calibration

The electronic chain sensibility was calibrated in order to determine the absolute detector gain, using a calibration capacitor instead of the detector. The electronic chain setup used for calibration is depicted in Figure 4. 3.

The anode readout signal follows the electronic chain in the sequence: preamplifier, amplifier and multichannel analyser. The amplifier output signal is digitized by the multichannel analyser (MCA), resulting in a Gaussian pulse height distribution. For charge gain calculation, the channel corresponding to the Gaussian mean value or centroid is taken. The detector gain, Gd, is then determined by the MCA channel and by the charge deposited in the detector by the incident radiation.

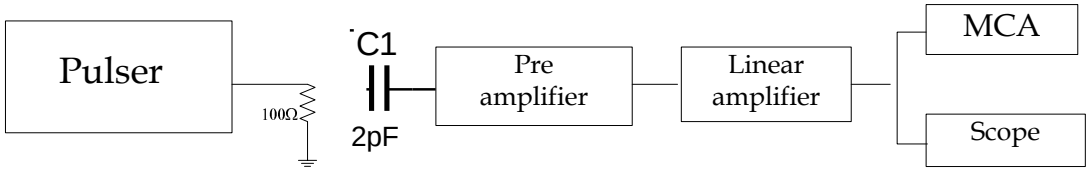

Figure 4. 3- Setup charge calibration scheme.

In the calibration process the detector is replaced by a calibrated capacitor. The calibrated capacitor, C_0= 2pF, is connected to a precision pulse generator BNC, with rectangular pulses characterized by an amplitude Vi, rise time of several tens of ns, fall time of few μs and a frequency of few KHz. The signal from the pulse generator will induce a charge on the capacitor, given by:

$$Q_i = C_0 V_{in} \quad (4.\ 1)$$

The charge signal from the capacitor is driven to the electronic chain, following exactly the same setup described above for the detector signal. The MCA distribution obtained from the capacitor signal is a very narrow peak (2-3 channels) resulting in a precise MCA channel, corresponding to the input signal provided by the pulse generator with fixed amplitude, Vin. Repeating the procedure for different Vin values, and so different Qi values, a calibration curve can be obtained, with the number of charges integrated, $N_{e,total}$, versus MCA channel. Figure 4. 4 depict the obtained calibration curve.

The $N_{e,total}$ is given by the relation:

$$N_{e,total} = \frac{Q_i}{e} = \frac{C_o}{e} V_i = a \times channel \quad (4.\ 2)$$

where e is the electron charge and a the slope parameter from the linear fit to the calibration curve.

The effective charge gain of the detector is given by:

$$G_{\det} = \frac{Ne,total}{Ne,\ primary} \quad (4.3)$$

Where $N_{e,total}$ is the total number of electrons at the anode readout, corresponding to the MCA channel of the centroid of the pulse height distribution, and $N_{e,\ primary}$ is the number of primary electrons produced by the X-ray interaction in the gas.

The number of primary electrons is given by:

$$N_{e,primary} = \frac{E}{W} \quad (4.\ 4)$$

where E is the X-ray energy and W is the average energy necessary to create an electron-ion par in the gas. This value is specific for each gas.

As referred above, $N_{e,total}$ can be given also by the follow relation:

$$N_{e,total} = \frac{channel_{Det}}{channel_{MCA}} \frac{C_0 V_i}{e} \quad (4.\ 5)$$

where $channel_{Det}$ and $channel_{MCA}$ corresponding to the centroide of the distributions obtained from X-ray pulses and BNC pulses, respectively.

Therefore, the effective charge gain of the detector is given:

$$G_{\det ector} = \frac{C_0 V_i}{channel_{MCA}} \frac{W}{E} channel_{Det} = a \frac{W}{E_{RX}} channel_{Det} \quad (4.\ 6)$$

The previous equation defines a calibration factor to calculate the detector gain. It should be noted that, the calibration factor will be adjusted to each gas, according to the respective w -value.

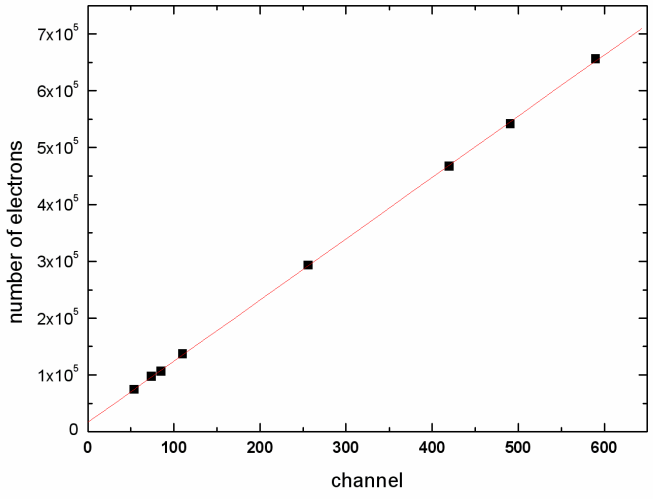

Figure 4. 4- Calibration curve of the electronic chain used in this experimental work.

4.3 Experimental Results

The GEM-MIGAS performance in Ar-CH_4 based mixtures was evaluated as a function of voltage across the GEM holes and the induction field. The amplification dependence on GEM voltage (V_{GEM}) is well known for a large variety of gas mixtures, where the increase of V_{GEM} value leads to an exponential increase of the charge gain. The maximum voltage applied, before the onset of discharges, is related with the gas. The induction field (E_{ind}) augment contributes to an efficient extraction of electrons from the GEM holes and at high E_{ind} values electron multiplication in the induction region is expected.

The MCA pulse-height distributions are fitted to Gaussian distributions, providing the parameters for charge gain and energy resolution calculation taken from the Gaussian centroid and from the full with at half maximum, respectively. Figure 4. 5 a) depicts a typical pulse-height distribution for 5.9 keV X-rays from a ^{55}Fe source obtained for V_{GEM}=350V and E_{ind}=5kV/cm in an Ar/CH_4(90/10) mixture. Figure 4. 5 b) shows the Gaussian fit.

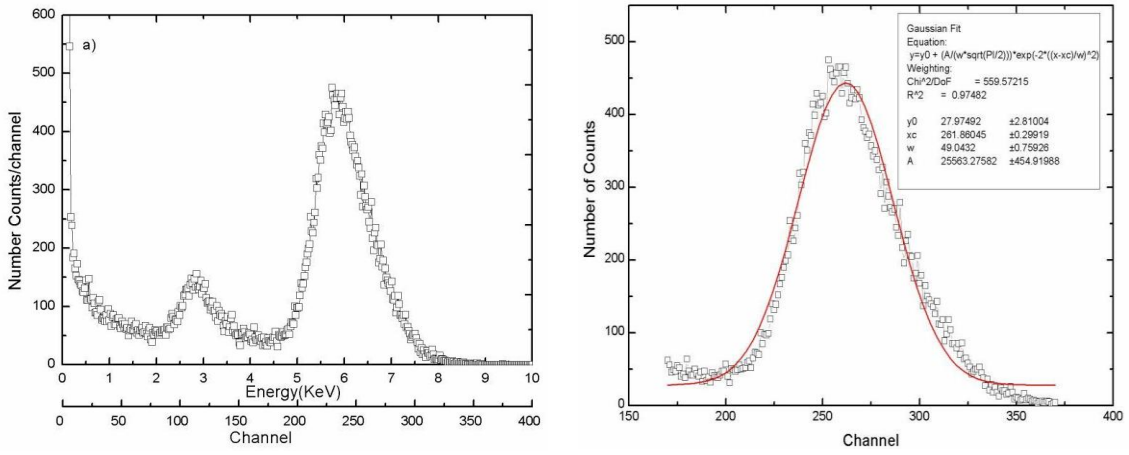

Figure 4. 5- a) Typical pulse-height distribution for 5.9 keV X-rays from a ^{55}Fe radioactive source obtained for E_{ind}=5kV/cm and V_{GEM}=350 V, in an Ar/CH_4(90/10%) mixture. b) Gaussian fit to the distribution to calculate the gain and energy resolution.

4.3.1 Charge Gain

Figure 4.6 depicts the effective charge gains obtained in Ar/CH_4 (90/10%) gas mixture, pure Ar and pure CH_4 as a function of V_{GEM} for several E_{ind} values and as a function of E_{ind} for different V_{GEM} values.

In Ar/CH_4 (90/10%) for the charge gain measurements as a function of V_{GEM}, the maximum GEM values applied before the onset of discharges was around 480V across the GEM, while maximum electric field applied to the induction region was 45kV/cm, Figure 4.6 a. The charge gain curves follow an exponen-

tial behaviour, typical of a proportional avalanche process. For all E_{ind} curves it is a clear a gain increase with V_{GEM}. Analysing the charge behaviour for 5kV/cm on induction field, a gain improvement of about 45 times is obtained, increasing the GEM voltage from 350V to 900V corresponding to gains of 20 and 900, respectively). The gain improvement with GEM voltage increase is more significant for E_{ind}=45 kV/cm, where the gain rises from 60 to 5000 for GEM voltage of 310 and 480 V, respectively. In Figure 4.6 a, it is also observed a gain augment with the induction field. Therefore, the maximum charge gain achieved with P10 was 5×10^3 for V_{GEM} = 480 V and E_{ind} = 45 kV/cm. The charge gain behaviour as a function of E_{ind} for fixed GEM values 350, 400 and 480V, Figure 4.6 b, shows a gain improvement as the induction field increases, which is more evident for lower GEM values. For example, at V_{GEM}= 350 V the increase on gain is about 9 times, from 20 to 180 at E_{ind} values of 5 and 45 kV/cm, respectively. At the highest GEM voltage applied the growth factor was about 7 times, from 700 to 5000, for E_{ind} values of 5 and 45kV/cm, respectively.

The charge gain behaviour as a function of GEM voltage in pure Ar (Figure 4.6 c) reveals a photon-feedback effect for the highest gains, where charge gain growth with V_{GEM} is supra-exponential. This effect is due to secondary avalanches initiated by photoelectrons extracted from the top GEM electrode, as a result of the charge avalanche extension outside the GEM-holes with the consequent emission of avalanche photons (wavelength ~120 nm in Ar) that induce photon feedback**.** It should be noted that the maximum charge gain, without secondary effects, was around 6×10^3 measured for the highest value of E_{ind} (40 kV/cm) for V_{GEM} = 270 V. The maximum charge gain, without secondary effects, decreases as E_{ind} decrease and V_{GEM} augments. The GEM voltage is responsible for the augment of the electric field penetration from GEM-holes towards the gap with consequent augment of the avalanche extension towards the gap (Ar ionization threshold is ~ 4 kV/cm). The charge gain behaviour as a function of the induction field (Figure 4.6 d) shows a gain augment as E_{ind} arises. The few points depicted are due to considerable change on the GEM voltage for the different induction fields.

The charge gain measured in pure CH_4 as a function of GEM voltage for fixed E_{ind} values (Figure 4.6 e) exhibits an exponential behaviour. The highest charge gain was around 3×10^3 for V_{GEM} = 765 V and E_{ind} = 35 kV/cm. The maximum voltages applied were 765 V to the GEM while the maximum electric field that could be applied to the induction gap was 40 kV/cm. A significant charge gain augment with the induction field was observed for fields up to about 20 kV/cm. For higher E_{ind} values, in the 25–40 kV/cm range, the charge gain increase is too small, saturating for the highest E_{ind} values where the charge gain

curves almost overlap. The saturation effect can be also observed in Figure 4.6 f, where it is clear a gain improvement until 20kV/cm on the induction field, after which the gain values remains practically constant. This behaviour can be explained attending to the low multiplication in the induction region, for the applied E_{ind} values. As the induction field increases, the exit electric field at the GEM-holes is reinforced, leading to an enhancement of the electron extraction efficiency from the GEM holes into the induction gap until its saturation. This is observed by the gain curves overlapping. This effect is not visible in P10 and pure Ar due to lower charge multiplication threshold for both gases relative to CH_4, allowing a significant charge multiplication in the induction gap for the electric fields that can be applied to the induction region.

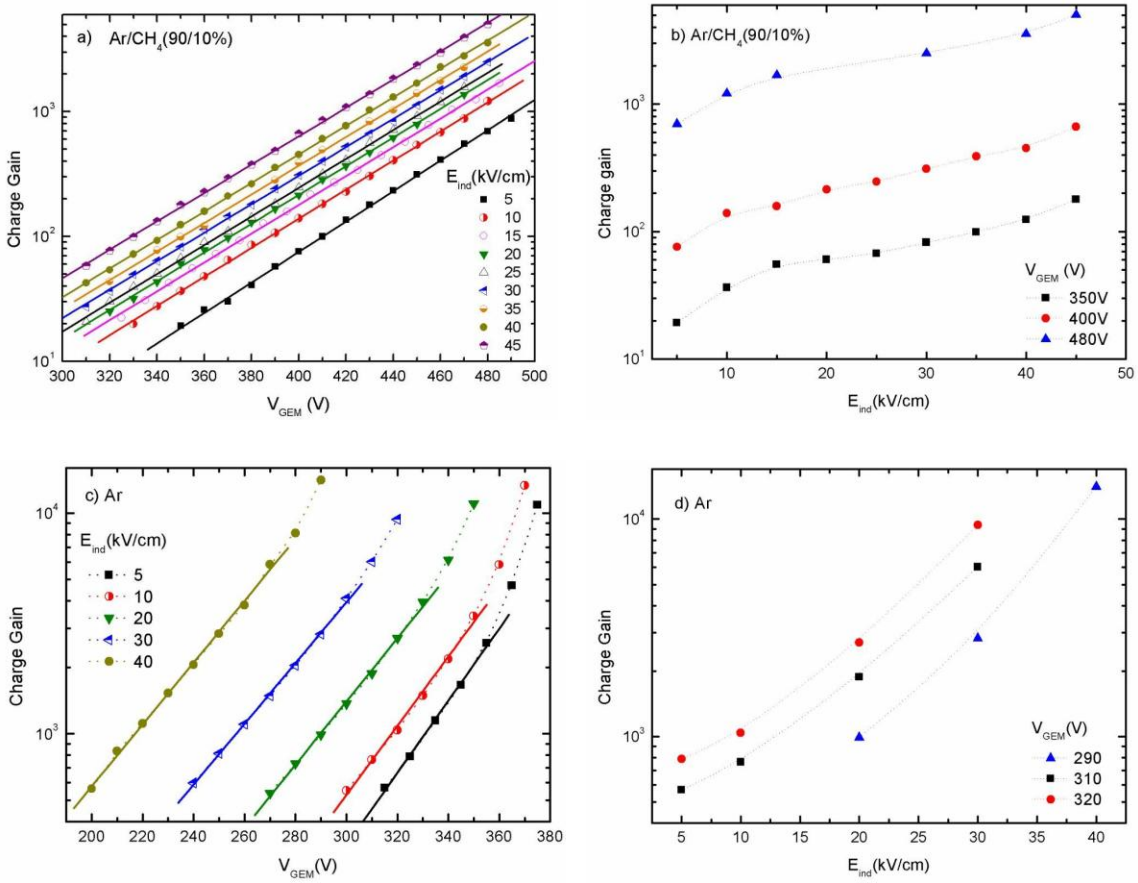

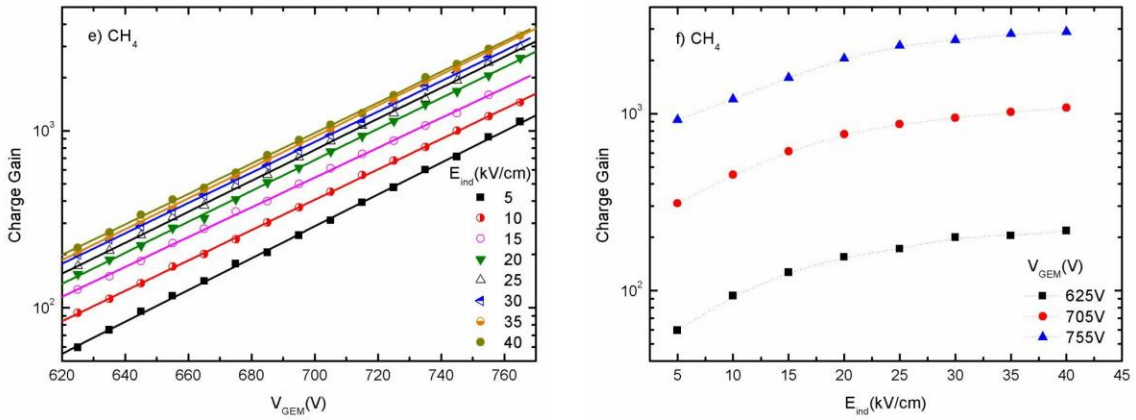

Figure 4.6 - Charge gain as a function of V_{GEM} and as a function of E_{ind}, measured in Ar/CH_4(90/10%), pure Ar and pure CH_4 at 1 bar with 5.9 keV Xrays.

The charge gain values obtained for the different gases doesn't differ significantly, being the highest gain achieved for Argon 10^4, with a slight decrease to 5×10^3 for P10 and 3×10^3 for CH_4.

In P10 the E_{ind} enhance has a most important rule on gain improvement being the best values achieved for the higher E_{ind} applied. In Ar, the gain improvement with the induction field is also evident. However, attending to photon feedback effects the charge gain achieved doesn't increase considerably with E_{ind}. The gain enhancement in CH_4 due to E_{ind} occurs until 20 kV/cm, after this value the curves overlap.

The V_{GEM} influence on charge gain behaviour has the same trend for all gases, where the increase on GEM voltage leads to an exponential increase of the gain augment. The GEM voltage necessary for charge multiplication is higher for CH_4, between 620 and 780 V, decreasing to values in the range of 300 to 500 V for P10 and for values below 400 V in argon. The low GEM voltages in Ar, below 300V, are related to E_{ind} values, being lower as E_{ind} increases. The induction field was in the range of 5 to 45 kV/cm for the three gases.

The comparison of the charge gain obtained for GEM-MIGAS with the reference structures, GEM and Micromegas, in similar conditions, reveals that the gain achieved with GEM-MIGAS operating with P10 is lower than that achieved with Micromegas or triple-GEM structures, which are higher than 10^4 [30][31]. The GEM-MIGAS maximum gain in Ar is better than the one measured for single-GEM structures, about 700 [32]. In pure CH_4, the GEM-MIGAS gain value is higher than the gains reported in the literature for single-GEM and Micromegas, about 70 [33] and 1.5×10^3 [34], respectively.

4.2.2 Energy Resolution

The energy resolution, defined by the Full With at Half Maximum (FWHM) of the pulse-height distribution divided by the respective centroid, was calculated for the conditions established for the charge gain measurements. The parameter FWHM as obtained by adjusting a Gaussian curve to the distribution obtained in the MCA.

Figure 4. 7a) depicts the energy resolution obtained for 5.9 keV X-rays in P10, Ar and CH_4 as a function of GEM voltage for several E_{ind} values and as a function of E_{ind} for different GEM voltages.

The best energy resolution obtained for P10 was approximately 20%, achieved for V_{GEM} in the range of 420 to 450 V and for 10kV/cm in the induction field, Figure 4. 7 a. This value is slightly lower than the threshold for charge multiplication in P10, ensuring a high extraction efficiency of electrons from the GEM holes to the induction gap, while no charge multiplication takes place in the induction gap, avoiding additional fluctuations in the charge multiplication process and leading to optimum energy resolution. The energy resolution behaviour as a function of E_{ind} (Figure 4. 7 b) points out that the increase on E_{ind} value leads to a degradation of the energy resolution, caused by the fluctuations on charge multiplication.

In pure CH_4 (Figure 4. 7 c), the minimum energy resolution of 20% was achieved for GEM voltage in the range of 700 to 765 V and for E_{ind} of 20 kV/cm. Once more, the induction field is inferior to the charge multiplication threshold in CH_4 and the optimum energy resolution obtained is similar to P10. The energy resolution improvement with E_{ind} augment until 20kV/cm is explained by the increase on the extraction efficiency of electrons from GEM holes. For E_{ind} values higher than 20 kV/cm, the electrons extraction efficiency does not cause further improvement of the energy resolution. This can be concluded from Fig. d, where the energy is depicted as a function of the induction field

In pure Ar (Figure 4. 7 e), a minimum energy resolution around 35% was achieved at V_{GEM} around 350 V and E_{ind} of 5 kV/cm, the lower induction field applied. For higher E_{ind} values, the energy resolution degrades, exhibiting a minimum value around 50% for the highest induction field of 40 kV/cm at V_{GEM} of 220 V. The energy resolution degradation of GEM-MIGAS structure with GEM voltage decrease was already detected in [27], being observed an increase of the relative variance of the avalanche gain with the reduction of V_{GEM} and with the increase of E_{ind}. Therefore, it should be expected a deterioration of the energy resolution in the two-multiplication stages when compared to the operation of the device in GEM-mode ($E_{ind} < 4$ kV/cm). In addition, for all the

energy resolution curves it is observed a strong deterioration, beyond its minimum value, with the V_{GEM} augment. This behaviour is attributed to photon-feedback effects.

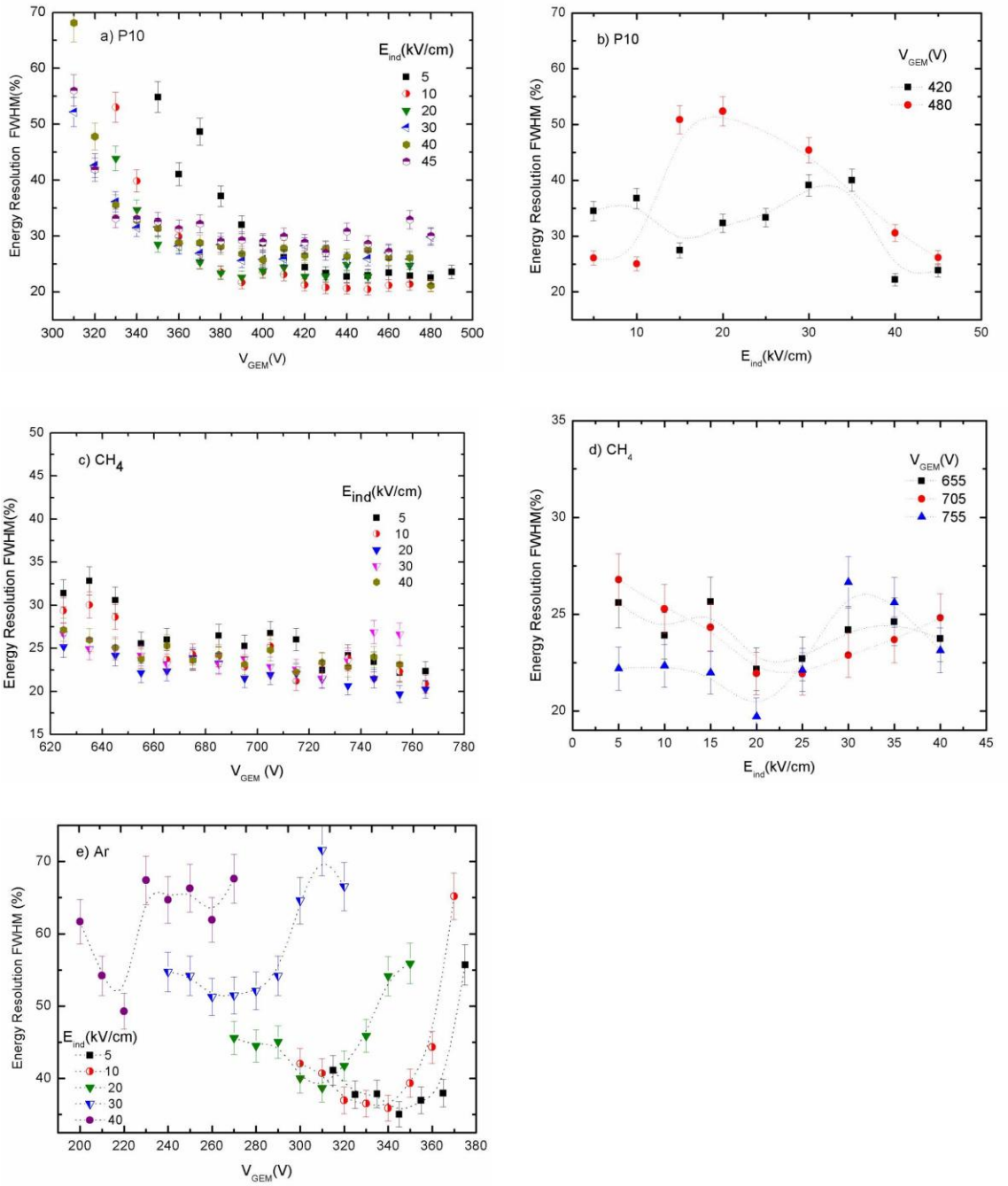

Figure 4. 7- Energy resolution for 5.9 keV X-rays obtained in: (a) P10 gas mixture,(b) pure Ar and (c) pure CH . The dot-lines in Ar are only to guide the eye.

The poor energy resolution achieved in Ar can be explained by the low drift velocity of electrons and the subsequent higher diffusion in the gap, being the charge distributed over a large area of the structure. As a consequence, the non-

uniformities of the structure cause additionally local variations in the charge gain, which leads to the deterioration of the energy resolution.

As expected, the avalanche relative variance in GEM-MIGAS is similar to the single-GEM for induction fields below the gas ionization thresholds. The multiplication in the induction gap will increase the avalanche relative variance contributing to the degradation of the energy resolution.

The behaviour of the energy resolution is similar for P10 and CH_4, improving with GEM voltage augment. The best value obtained was around 20% for E_{ind} values of 10 and 20 kV/cm, respectively. The enhancement of the electrons extraction efficiency from the GEM holes, as well the absence of charge multiplication for lower E_{ind} values, contribute to the absence of energy fluctuations. In argon, the energy resolution was also better for low induction field values, being the best value, 35%, measured for 5 kV/cm on the induction region. However, due to the photon feedback is observed a huge degradation of the values as the V_{GEM} increase.

4.4 Conclusions

The performance characteristics, including charge gain and energy resolution for soft X-rays, of a GEM-MIGAS based detector were investigated in pure Ar, pure CH_4 and in P10 gas mixture. Maximum charge gains of about 10^4, 3×10^3 and 5×10^3 were measured, respectively. The best energy resolutions achieved for 5.9 keV X-rays are 35% for Ar and 20–22% for CH_4 and P10. Table 4. 1 summarizes the maximum charge gain and the respective conditions. The values corresponding to the minimum energy resolution are presented in Table 4. 2.

An important observation is that the maximum gain, without secondary effects, obtained in pure Ar is about 10 times higher than the gain measured in a single-GEM. The charge gains obtained in pure CH_4 and in pure Ar with GEM-MIGAS are higher than the values obtained with single-GEM and Micromegas electron multipliers. The gain measured in P10 is higher than the obtained in single-GEM, but lower relatively to Micromegas. This result was expected attending the two multiplication stages of GEM-MIGAS and due to the efficient electron extraction and collection in the anode readout, which minimizes the loss of electrons to the GEM bottom electrode.

Table 4. 1- Resume of the maximum charge gain obtained and the respective conditions.

	Gain	V_{GEM} (V)	E_{ind} (kV/cm)	FWHM (%)
Ar/CH_4(90/10)	5×10^3	480	45	20
Ar	1×10^4	375	40	35
CH_4	3×10^3	765	35	20

Table 4. 2- Resume of the minimum energy resolution obtained and the respective conditions.

	FWHM (%)	V_{GEM} (V)	E_{ind} (kV/cm)
Ar/CH4(90/10)	20	420-450	10
Ar	35	350	5
CH_4	20	700-765	20

Chapter 5

GEM-MIGAS with different gaps

In conventional GEM-MIGAS structure the induction gap is set around 50 μm. However, thicker gaps may result in higher gains given the avalanche develop through larger distances. On the other hand, the applied voltage to the induction gap has to increase in order to maintain similar electric fields. The charge gain characteristics of GEM-MIGAS will be evaluated as a function of induction gap thickness, using the single electron response method. In the present study, the induction gap was varied between 50 and 300 μm and the GEM-MIGAS was operated in gas flow mode using a He/iso- C_4H_{10} (85/15%) gas mixture.

5.1 Introduction

The charge gain of a GEM is mainly dependent upon the hole diameter [8], its counterpart in the induction region depends upon the induction gap thickness, *d*. A simple parametric charge gain model, similar to the one used with micromegas [85][86], was used to fit the experimental charge gains associated to the GEM-MIGAS induction region [5]. This enabled to demonstrate that the charge gain sensitivity of the GEM-MIGAS is least prone to variations in *d* and to changes in the ambient conditions, i.e. pressure and temperature, when the induction gap is set around 50 μm [35]. In addition, the optimum gap for sustaining the highest charge gains was calculated to be in the 40-60 μm range, for detector operation in He/iso-C_4H_{10} (85/15%) at atmospheric pressure [35]. This model was based on a uniform field approximation in the induction gap. Indeed, this situation is not present under regular operational conditions. Electric field simulations of the GEM-MIGAS device [63] have shown that the maximum electric field intensity is only reached in the induction gap, and not in the GEM holes, for a range of GEM and induction voltage conditions. Therefore,

there is a motivation to evaluate the performance of the GEM-MIGAS with induction gap thicknesses above 50μm. Larger induction gap thicknesses may sustain larger voltage differences, which may lead to higher effective gains. In this work the average charge obtained by GEM-MIGAS is investigated for several gap thicknesses, d, of 50,100, 150, 200, 250 and 300 μm. The GEM-MIGAS single-electron response was investigated as a function of the induction gap voltage, with the voltage across the GEM holes, V_{GEM}, set at 100 V, i.e. no charge multiplication within the holes.

5.2 Experimental Setup

The experimental arrangement for measuring the single electron response as a function of induction field is based on the single-electron response method, and is shown in Figure 5. 1 for the case of d= 50 μm.

The GEM was fabricated in the CERN TS-DEM workshop and consisted of a 50-μm thick copper clad (5 μm in thickness) Kapton foil with 70 /50 μm diameter holes in copper /Kapton patterned at 140-μm hole pitch in an hexagonal distribution. The GEM has an active area of 10×10 mm^2 and is supported on a G-10 frame.

The induction electrode was also fabricated in the CERN TS-DEM workshop. This consisted of a 10×10 mm^2 copper anode onto which insulating pillars of height d, ranging from 50 to 300 μm, were placed at 1 mm intervals. In order to construct the GEM-MIGAS, the anode readout was coupled to the GEM frame so that the GEM was in direct contact with the pillars, thereby defining the induction gap. The drift electrode consisted of a thin quartz disc with a thin coating of indium tin oxide and was mounted above the GEM at a distance of 4 mm.

A Mercury lamp (model UVP 90-0012-01-11SC-1) with a peak emission at 254 nm (≅ 4.88 eV) was used to illuminate the detector drift gap perpendicular to the GEM plane, resulting in a constant flux of photoelectrons emitted from the GEM-top copper electrode, operating as a reflective photocathode (work function ~4.5 eV). For a given operational voltage of the GEM-MIGAS, these photoelectrons were focused into the GEM holes, undergoing multiplication, and then extracted into the induction region for additional multiplication. Count rate in the order of 30 kHz was maintained throughout these measurements.

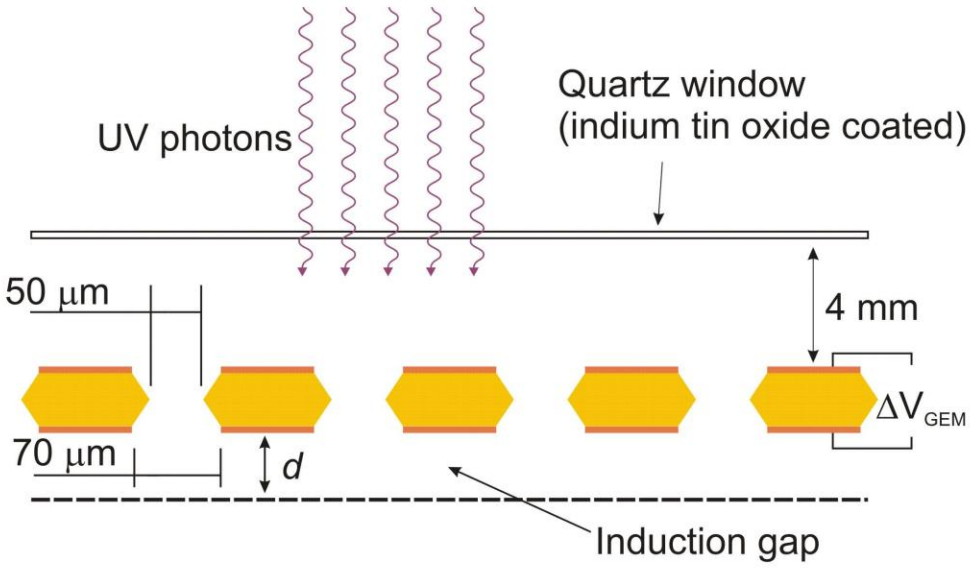

Figure 5. 1- Schematic diagram of the GEM-MIGAS based detector used for this study.

In these studies, He/iso-C4H10 (85/15%) gas mixture was flowed through the chamber. The drift-electrode and the GEM electrodes were operated at negative voltages while the anode readout was held at ground potential and connected electrically to an Ortec charge preamplifier (model 142A). The preamplifier output was then fed into an Ortec shaping amplifier (model 575A) with shaping-time constants adjusted to 0.5 μs. The bipolar output of the shaping-amplifier was in turn fed into an Ortec pulse-height analyzer (model ASPEC-927).

For a given induction gap thickness, the single electron response from the induction gap region was examined as a function of induction gap voltage, *Vind*. The gain contribution from the GEM holes was set to unity. For this purpose, maintaining V_{GEM}=100 V was found to be enough to transfer electrons from the drift region into the induction gap region without undergoing electron multiplication in the GEM holes. The drift field, E_{drift}, was maintained at approximately 0.25 kV/cm.

5.3 Results

Figure 5. 2 shows a typical single-electron response of GEM-MIGAS with the 300 μm induction gap using He/iso-C_4H_{10} (85/15%) for several induction voltages V_{ind}, for a V_{GEM}=100 V and the drift field E_{drift} = 0.25 kV/cm. It is well accepted that the single-electron pulse height spectra in gaseous detectors are predicted by a peaked distribution known as Polya distribution [2], [87]:

$$P(q) = \left[(1+\theta)\frac{q}{\bar{q}} \right]^{\theta} e^{-(1+\theta)\frac{q}{\bar{q}}} \quad (5.1)$$

The Polya distribution is characterized by the parameter q, which represents the number of electrons in an electron avalanche (i.e. the avalanche charge gain), and by an empirical parameter θ, which is related to the first Townsend coefficient and being $\bar{q}$ the average avalanche gain. Thus, by fitting the observed single-electron pulse height distributions to Eq. 5.1, for the different V_{ind}, it was possible to determine the associated average charge gain as a function of induction voltage.

Figure 5. 3 shows the average charge gain as a function of induction voltage V_{ind} for the induction gap thicknesses of 50, 100, 150, 200, 250 and 300 µm, as obtained from the fit of eq.1. As can be seen from these results, the uppermost gains, achieved before the onset of detector electrical instabilities, occur when d is set between 150 to 300 µm. For this region, gains above 10^6 can be reached in the induction gap. The gains obtained for the 50µm gap are similar to those obtained using Micromegas devices with He/isobuthane mixtures, with a relatively small percentage of the quencher gas [88][89][90]. The attainment of high charge gains is attributed to the Penning effect which effectively reduces UV photon feedback processes. This effect involves the transfer of the energy of the excited metastable He atoms (19.8 eV) to ionize the isobutane molecules (10.6 eV).

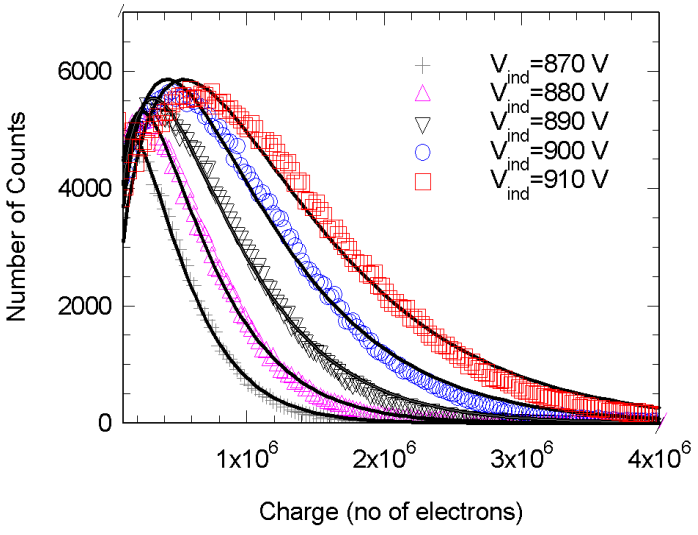

Figure 5. 2 - Single-electron pulse-height distributions measured with the GEM-MIGAS detector with the gap set at 300 µm and using He/iso-C_4H_{10} (85/15%) gas mixture, for several values of induction voltages, V_{ind}. The voltage across the GEM and the drift field were set to V_{GEM} = 100 V and to E_{drift} = 0.25 kV/cm, respectively. Solid lines show Polya fits (Eq. 5.1) to the experimental data, from which the average charge gain was obtained.

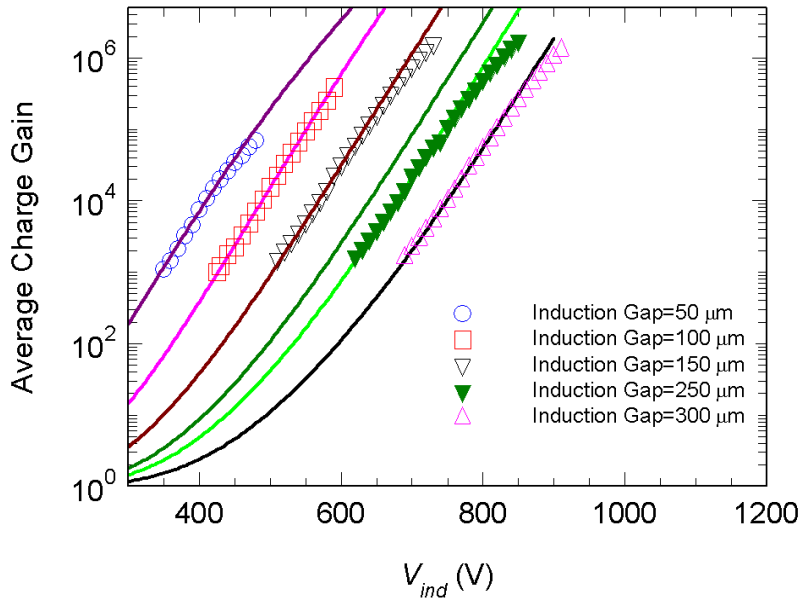

Figure 5. 3 - Average charge gain as a function of induction voltage *Vind* applied across a number of different induction gaps in the He/iso-C_4H_{10} (85/15%) gas mixture. In all cases, V_{GEM} was set to 100 V, ensuring no multiplication in the GEM-holes. Curve fits of the form of Eq. 5.2 were applied to the experimental data (solid lines).

For a given induction gap thickness, the dependence of the average charge gain on V_{ind} can be written as follows [9,10]:

$$\ln \bar{q} = Ae^{-\frac{AB}{V_{ind}}} \quad (5.2)$$

where the parameters $A=\lambda/d$ and $B=W$ are related to the electron mean free path between inelastic collisions λ, and the threshold of potential energy required to cause ionisation by electron impact with the gas atoms/molecules, W. Both parameters A and B (hence λ and W) can be derived, using Eq. 5.2, from the fit of the average charge gain characteristic curve (q versus V_{ind}) as shown in Figure 5. 3.

Figure 5. 4 shows the values of λ and W as a function of induction gap thickness, obtained from the fits. As expected, the W parameter does not depend on the gap thickness, while λ increases linearly with increasing induction gap thicknesses due to the comparatively lower electric fields that exist in wider gaps. In Table 5.1, we present the values of λ and W for the different induction gap thicknesses, as well as the electric field range used for each gap.

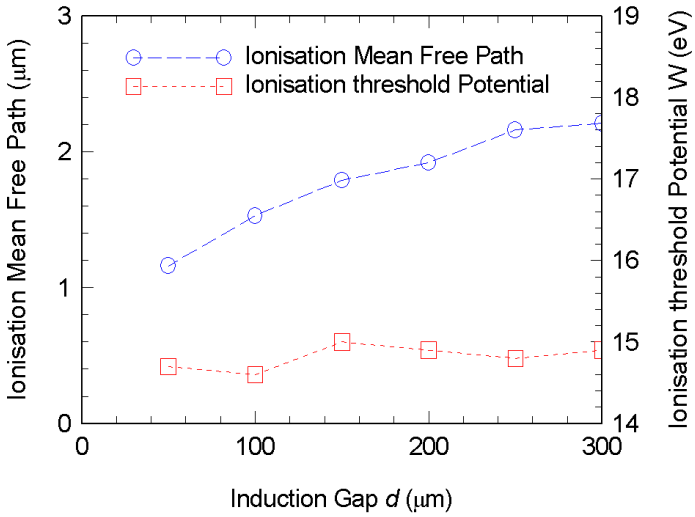

Figure 5. 4 - Ionization mean free path, λ , and ionization threshold potential, *W*, as a function of induction gap thickness in the He/iso-C_4H_{10} (85/15%) gas mixture, at atmospheric pressure.

Table 5. 1- λ and *W* values obtained for the different induction gap thicknesses, and the electric field ranges used in each case.

Induction gap thickness (μm)	E_{ind} (kV/cm)	λ (μm)	*W* (eV)
50	70-95	1.16	14.7
100	40-60	1.53	14.6
150	35-45	1.79	15.0
200	30-40	1.92	14.9
250	25-35	2.16	14.8
300	20-30	2.21	14.9

The knowledge of λ and *W*, combined with the average gain formula shown in Eq. 5. 2 permits an evaluation of the average gain as a function of gap thickness, *d*, for a fixed V_{ind}. For example, for λ and *W* values obtained for the *d*=50 μm curve of Fig.3, λ = 1.2 μm and *W*=14.7 eV, and for the case where V_{ind} = 450V, one can obtain the variation of the gain as a function of induction gap thickness. Figure 5. 5 shows the gain curves as a function of induction gap thickness, using the λ and *W* pair of values shown in Table 1, for the *d*=100, 150, 200, 250 and 300 μm curves of Figure 5. 4. These experimental results confirm the analysis made in ref. [15], namely that the optimum induction gap thickness ranges between 50 and 70 μm for the present detector operation, at atmospheric pressure. This is also seen in Figure 5. 3, where the gain curve obtained for the 50μm gap presents the highest values, even when extrapolated to the whole V_{ind} range studied in this work. However, the physical limit of electric insulation of

the device does not permit to apply the highest V_{ind} to the 50 μm induction gap. Therefore, the highest effective gains can be obtained using induction gaps in the range of 150-300 μm, owing to the higher voltage differences that can be applied to the induction gap. The higher voltage difference that can be established in thicker gaps allows for more energy available from the electric field for electron multiplication, thus achieving higher gains.

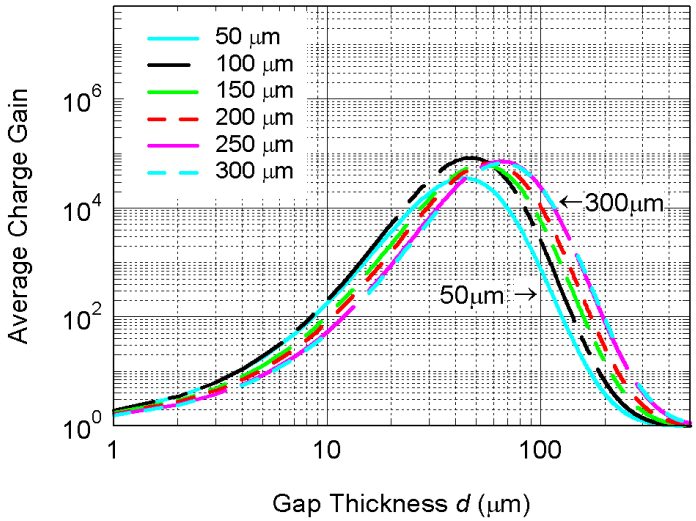

Figure 5. 5 -Average charge gain as a function of induction gap thickness, *d*, in the He/iso-C_4H_{10} (85/15%) gas mixture, as predicted by Eq. 5.2 for V_{ind}=450 V. For each induction gap thickness, the associated λ and *W* values (see Table 5.1) are used to calculate the average charge gain curve.

5.4 Summary

A GEM-MIGAS was successfully operated in the parallel-plate mode using the He/iso-C_4H_{10} (85/15%) gas mixture at atmospheric pressure to measure the charge gain characteristics with the induction gap set to 50, 100, 150, 200, 250 and 300 μm. For this purpose, the voltage difference in the GEM holes was set to 100 V, i.e. without charge multiplication in the holes.

The uppermost charge gains, before the onset of detector's electrical instabilities, occurred when *d* was set between 150 and 300 μm, reaching values above 10^6. The charge gain response agreed well with the classical parallel plate gain formula, in spite of the existence of non-uniform electric fields in the induction gap [63].

Chapter 6

The Ion Back-Flow Measurements

The performance of GEM-MIGAS device will be evaluated regarding the Ion Back-Flow and charge gain for an induction region length between 50 to 300 μm The studies were carried out with a GEM-MIGAS coupled to a semitransparent CsI-photocathode operated in Ar/5%CH_4 gas mixture at atmospheric pressure.

6.1 Introduction

The GEM-MIGAS can exploit the good ion back-flow (IBF) reduction capability achieved in Micromegas [39]. By using strong electric fields in the induction gap, it is expected to achieve an improved reduction of the ion back-flow towards the conversion/drift region and towards the GEM-top electrode, as it was observed in other detectors [40]. Furthermore, the optical transparency of the GEM-MIGAS should be lower compared to a single GEM (typically 10%) [11] and to a Micromegas (typically 50%) [9]. The extension of the electron avalanche into the induction gap allows the spurious UV-photons to be almost concealed from the GEM-top electrode and from the drift electrode.

The ion back-flow quantifies the fraction of avalanche ions that leave the amplification stage of the detector and reach the drift volume. In Gaseous Photomultipliers (GPM), most of the back-flowing ions are collected on the photocathode inducing secondary effects and photocathode aging. In Time Projection Chambers (TPC) the ion back-flow constitutes a slowly drifting space charge reducing the local electric field. The ion back-flow fraction is given by the flux of ions collected in a cathode divided by the flux of electrons collected in the anode. The electron and ion transport properties have an effect on the IBF performance, thus the optimization of the electric field along the different regions of the detector is very important.

The micropattern gaseous multipliers used in photodetectors could reduce the ion back-flow to the photocathode since a large number of ions are neutralized in the multiplier electrodes. However, a fraction of avalanche ions follows the electric field lines through the multiplier holes colliding with the photocathode. In GPMs, the expected reduction of the ion- and photon-feedback effects is an advantage if the multiplier is coupled to a solid photocathode, either in semi-transparent mode or in reflective mode (directly deposited in the top face of the GEM), [41]-[45]. The impact of avalanche ions on the photocathode limits the performance of GPMs, it strongly limits the multiplier gain, damages the photocathode surface and deteriorates its quantum efficiency (QE). Furthermore, the reduction of the ion back-flow towards the conversion/drift region is also important for tracking detectors and TPCs, where the ion back-flow to the drift region modify locally the electric field due to space-charge effects [46] ,[47]. This results in dynamic particle-track distortions, which seriously affects the tracking properties of TPCs in high-multiplicity experiments, e.g. in relativistic heavy-ion physics applications [64].

In this chapter it will be reported the investigation on ion back-flow suppression capability of the GEM-MIGAS with induction gap thicknesses in the range of 50–300 μm. The charge gain and the IBF – defined as the fraction of total avalanche-ions that reach the semitransparent photocathode – were measured for the several thicknesses of the induction gap as a function of electric fields and voltages applied to the electron multipliers. The main motivation of this study is to establish the conditions for achieving the lowest IBF with the GEM-MIGAS. The experimental studies, charge gain and ion back-flow, were carried out in an Ar/CH_4 (95/5%) gas mixture.

6.2 Experimental Setup

The GEM-MIGAS was assembled in a stainless-steel cylindrical chamber connected to a vacuum/gas system. The chamber has a quartz window with a thickness of 5 mm on top and four SHV-connectors on bottom used as feedthroughs. The chamber was pumped down to 10^{-6} mbar and then filled with 1 bar of Ar/CH_4 (95/5%). The gas circulation was maintained by convection through SAES St707 getters, operated at 160ºC. Figure 6. 1 is a photograph of the chamber, with the GEM-MIGAS and the photocathode already assembled.

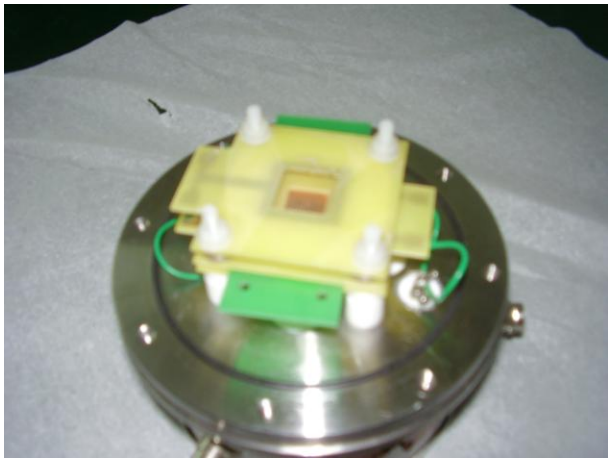

Figure 6. 1- Photograph of the gas chamber used for this experimental work.

A CsI photocathode with a square geometry of 12×12 mm^2 and a thickness of 250 Å, was deposited in a quartz disk with 5 mm thick, in a dedicated vacuum evaporation plant. An aluminium layer of 150 Å was previously vacuum-evaporated on the quartz to provide electric contact. A schematic diagram of the detector is depicted in Figure 6. 2.

The GEM-MIGAS electron multiplier has an active area of 10×10 mm^2. The induction/anode electrode is a copper micromesh deposited on a G-10 board. In this work, micromeshes with different induction gap values, between 50 to 300 μm were used. The drift region is established between the photocathode and the top of the GEM, with a thickness of 4.5 mm.

The detector was illuminated with a continuous UV Hg(Ar)-lamp (model 6035 Newport), collimated to 7 mm in diameter. Attenuators were used on the top of the chamber window to reduce the photon rate, maintaining the currents on the various electrodes below charging-up levels.

The electrodes were individually biased by HV-power supplies (CAEN model N471A) and the current was limited to ~50 nA. Additionally, protection resistors (after an RC-filter) were used in order to limit the bias current to the GEM electrodes in presence of sparks. The photocathode was connected to a grounded digital electrometer (Keithley, model 614) to measure the photocathode current (I_{ph}), while the current on the induction/anode electrode (I_A) was measured with a floating digital multimeter Fluke 175 True RMS, 10 MΩ input impedance, by recording the voltage drop on a 33 MΩ resistor, placed between the power-supply and the electrode, Figure 6. 2.

The gain and IBF were measured as a function of the GEM voltage for different E_{ind} values and a fixed drift field, E_{drift}=0.5kV/cm. These parameters were also measured as a function of E_{ind} for a fixed V_{GEM}=350V and E_{drift} values be-

tween 0.1 and 1kV/cm. Additionally, for the 50 µm configuration, the IBF was measured as a function of E_{drift} for the highest E_{ind} value.

The charge gain, G, is given by the current in the micromesh, I_A, normalized to the primary photocathode current (I_{ph0}),

$$G = I_A / I_{ph0} \quad (6.1)$$

where I_{ph0} is the current measured in the photocathode while applying a voltage to the GEM top, interconnected to the GEM bottom and to the induction electrodes. The ion back-flow ratio, IBF, is given by:

$$IBF = (I_{ph} - I_{ph0}) / I_A \quad ((6.2)$$

where I_{ph} is the total current measured in the photocathode, which includes both the photoelectron and the positive ion currents.

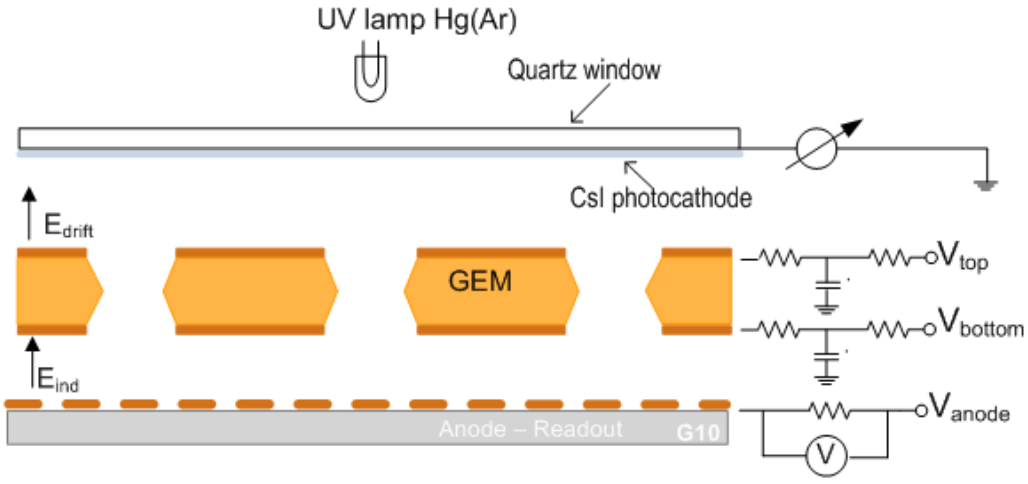

Figure 6. 2- Schematic diagram of the GEM-MIGAS detector used for IBF studies.

6.3 Charge Gain

The charge gain was evaluated as a function of the GEM voltage, the induction field and the drift field for GEM-MIGAS with induction region lengths of: 50, 100, 200, 250 and 300 µm.

6.3.1. 50 µm Induction region gap

The 50 µm thick GEM-MIGAS gain behaviour in Ar/CH_4(95/5%) as a function of GEM voltage is depicted in Figure 6. 3 a) for different induction field values. The drift field was kept constant, E_{drift}=0.5 kV/cm.

The gain behavior with the voltage applied to the GEM has an exponential dependence, achieving the maximum value, around 10^4, for V_{GEM}=425V and E_{ind}=50 kV/cm. The increase on the induction field from 5 to 50 kV/cm leads to considerable gain augment, almost two orders of magnitude. The induction field contribution to the gain improvement can be also observed in Figure 6. 3 b), where the gain is depicted as a function of E_{ind} for V_{GEM} values of 350 and 425 V.

The effect of the drift field on the gain is depicted in Figure 6. 4 c, showing the residual influence of the different drift field on the maximum gain value achieved.

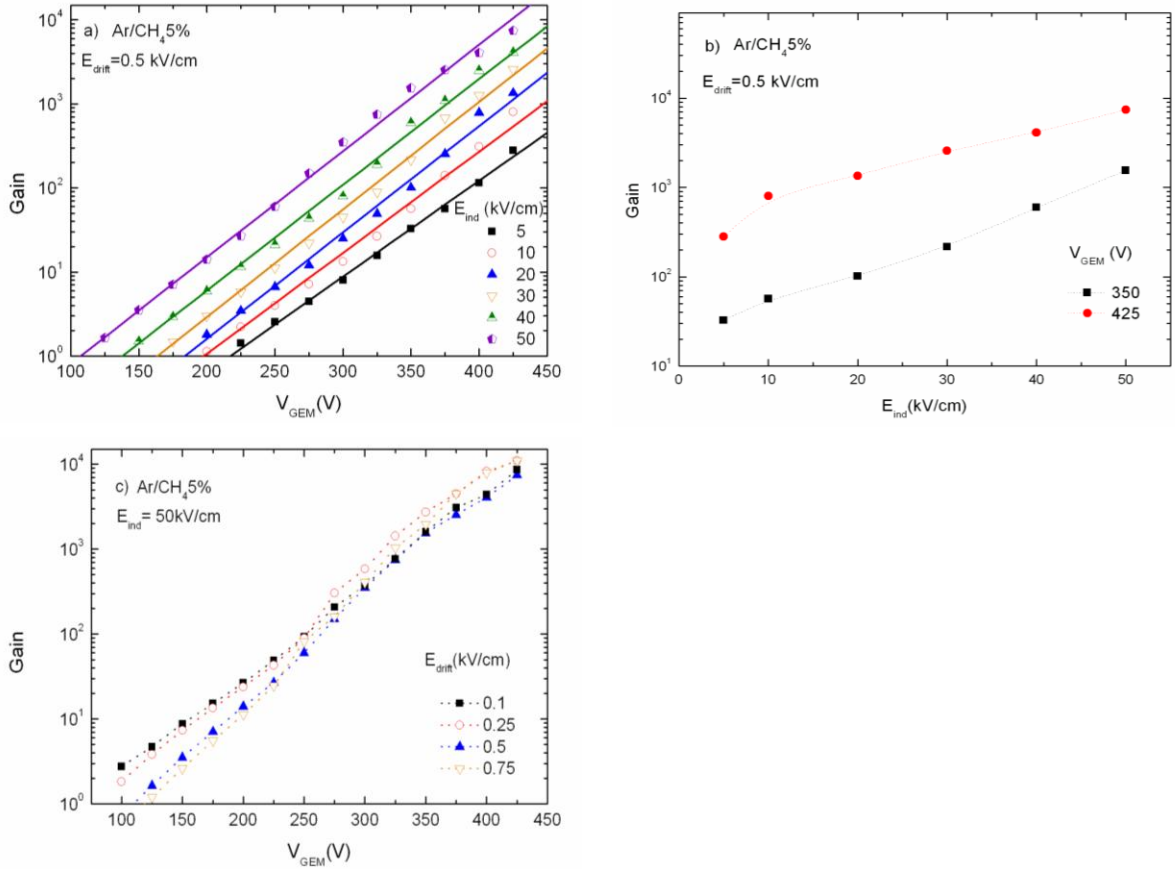

Figure 6. 3 - Charge gain in Ar/CH4 (95/5%) as a function of: a) V_{GEM} for different E_{ind} values (E_{drift}=0.5 kV/cm), b) E_{ind} for V_{GEM} values of 350 and 425 V (E_{drift}=0.5 kV/cm), c) V_{GEM} for different E_{drift} values (E_{ind}=50 kV/cm),.

6.3.2 100 µm Induction region gap

The gain performance obtained for the 100 µm GEM-MIGAS configuration is depicted in Figure 6. 4. In Figure 6. 4 a) the gain is depicted as a function of GEM voltage for different induction fields and E_{drift}= 0.5kV/cm. In figure b) the gain is depicted as a function of E_{ind} for different drift field values: 0.1, 0.25, 0.5, 0.75, 1 kV/cm, for V_{GEM} of 350V.

The gain improvement with the GEM voltage, Figure 6. 4 a), follow an exponential dependence being the highest gain about 2×10^4, for V_{GEM}=425V and E_{ind}=40 kV/cm, the maximum values before the onset of discharges. The augement of E_{ind} from 5 to 40 kV/cm results in a gain increase of two orders of magnitude, from 2×10^2 to 2×10^4 at V_{GEM}=425V.

The relation between the gain and the induction field, for a fixed V_{GEM}=350V, is depicted in Figure 6. 4 b). The maximum induction field applied was 47.5 kV/cm. This increase on E_{ind} allows a slight gain improvement to about 6×10^4, V_{GEM}=350V. A good performance is also obtained by increasing the induction field and keeping V_{GEM} in lower values. This is an advantage to reduce the GEM discharge probability and prolong its life time.

The gain behaviour for different E_{drift} values, Figure 6. 4 b), shows a slight difference in the maximum achieved gain values, varying from 10^4 to 7.0×10^4.

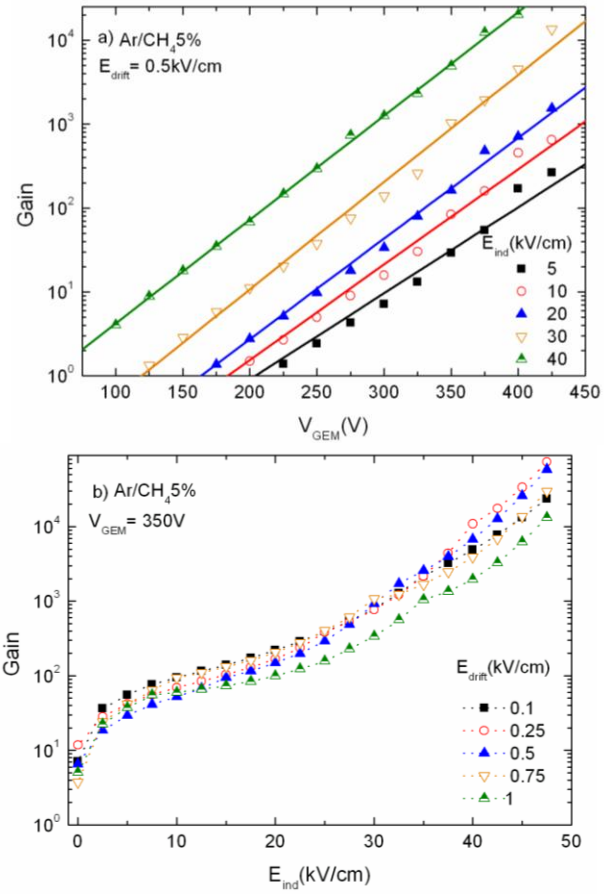

Figure 6. 4 - Charge gain as a function: a) V_{GEM} for different E_{ind} values and for E_{drift}=0.5 kV/cm. b) E_{ind} for different E_{drift} and V_{GEM}=350V, for a 100μm induction gap.

6.3.3 200 μm Induction region gap

The gain measured for the 200 μm GEM-MIGAS configuration is depicted in Figure 6. 5 a) as a function of V_{GEM} for different induction field values and E_{drift}=0.5 kV/cm. The gain increases exponentially with GEM voltage, achieving a maximum value around 2×10^4 for 350V and 30kV/cm, the highest voltages applied before the onset of discharges. The gain increases approximately two orders of magnitude from the lowest to the highest E_{ind} values, 5 and 30kV/cm.

The gain behaviour as a function of E_{ind} is depicted in Figure 6. 5b) for a fixed V_{GEM}=350V and different drift fields. In this set of measurements the little increase on E_{ind} from 30 to 32.5 kV/cm is traduced in a slight improvement of the maximum charge gain to 3×10^4, for V_{GEM}=350 Vand E_{drift}=0.5kV/cm .

The influence of the drift field in the gain performance is not very significant. For E_{drift} values in the range of 0.1 to 1 kV/cm the gain varies between 2×10^4 and 3×10^4.

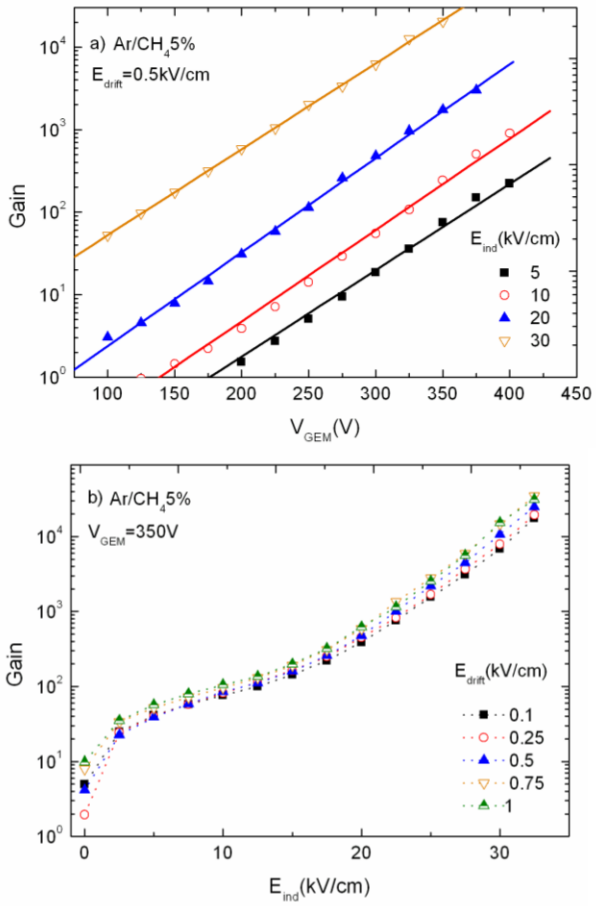

Figure 6. 5 - Charge gain as a function: a) V_{GEM} for different induction field values and E_{drift}=0.1 kV/cm. b) E_{ind} for different drift field values and V_{GEM}=350V, for a 200μm induction gap.

6.3.4. 250 μm Induction region gap

Figure 6. 6 a) depicts the gain as a function of the V_{GEM}, for different induction field values and a drift field of 0.5 kV/cm. The gain improves exponentially with GEM voltage, achieving a maximum value of 1.4×10^4 for the highest E_{ind} value applied, 30 kV/cm, and V_{GEM}=350 V.

The gain dependence on E_{ind} is depicted in Figure 6. 6 b) for several E_{drift} values and a GEM voltage of 350V. The gain improves with increasing induction field values, achieving the maximum value, in the order of 10^4, for the highest E_{ind} value 30kV/cm. The maximum gain is practically constant for the different drift fields applied.

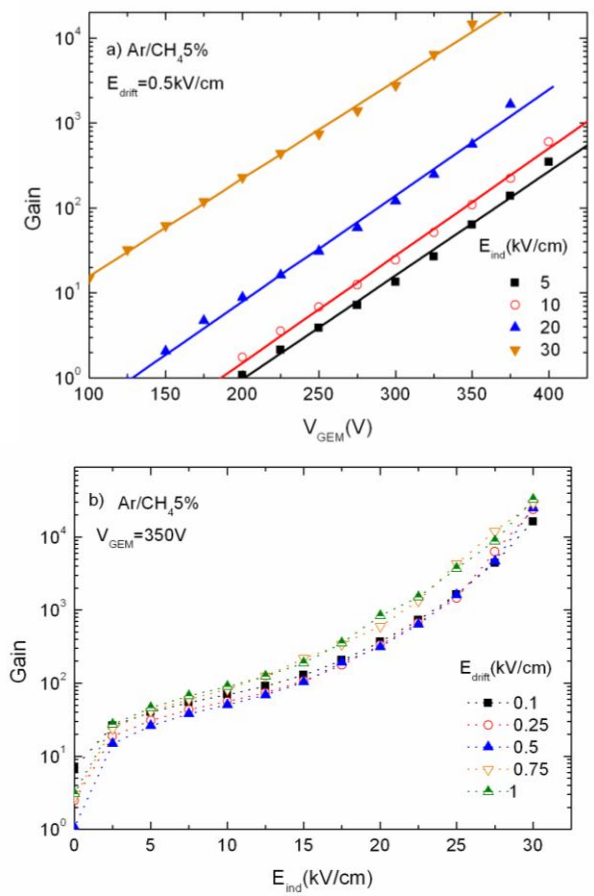

Figure 6. 6- Charge gain as a function: a) VGEM for different induction field values and Edrift=0.5kV/cm, b) Eind for different drift field values and V_{GEM}=350V, for a 250μm induction gap.

6.3.5. 300 μm Induction region gap

For the 300 μm gap configuration, it was not possible to depict the gain behaviour as a function of GEM voltage, given the several instabilities during the GEM-MIGAS operation.

The gain behaviour as a function of E_{ind} is depicted in Figure 6. 7 for different E_{drift} values and fixed V_{GEM}=350 V. The maximum gain measured was of the order of 10^5, obtained for the highest induction field applied, 25 kV/cm and E_{drift}=0.5 kV/cm. The drift field has a considerable influence on the gain obtained, from 4×10^4 at E_{drift}=0.1kV/cm to 7×10^5 at E_{drift}=1kV/cm .

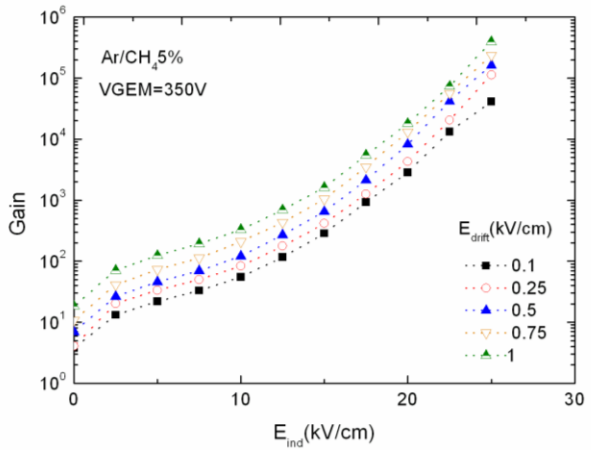

Figure 6. 7 - Charge gain as a function of Eind for different drift field values and VGEM=350V, for the 300μm induction gap.

6.3.6 Summary

In order to compare the results from the different induction region thicknesses and set the main conclusions, Figure 6. 8 shows a compilation of the charge gain obtained for the different gaps as a function of E_{ind}, for V_{GEM}=350Vand E_{drift}=0.5 kV/cm.

The maximum induction field reached before the onset of microdischarges depends on the gap, decreasing as the induction region thickness increases. For the smaller region, 50 μm gap, the maximum E_{ind} value was 50kV/cm, decreasing to 25kV/cm for 300 μm gap.

The induction region enlargement leads to a gain improvement from 10^3 for the 50 μm gap to 10^5 for the gap of 300 μm. Due to the lower induction fields reached for the thicker induction gaps, the higher voltages that can be applied result in more energy available from the electric field for charge multiplication.

The GEM-MIGAS performance concerning the maximum achieved gain compares favourably with the gain achieved in 3- and 4-GEMs configurations [48][49] and in Micromegas [8].

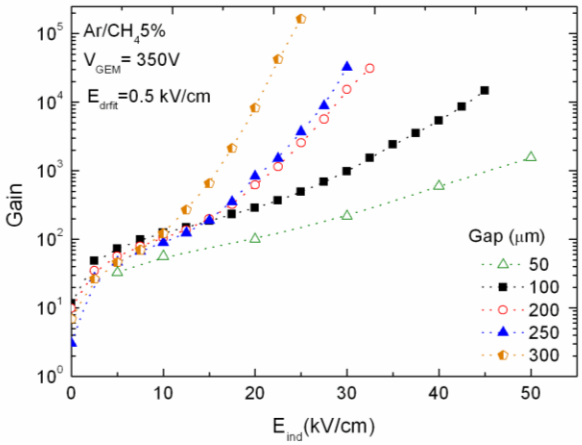

Figure 6. 8 - Effective charge gain as a function of E_{ind} for different induction gap thicknesses in the GEM-MIGAS operated in a Ar/5% CH4 gas mixture at atmospheric pressure.

6.4 Ion back-flow results

The ion back-flow was evaluated as a function of the GEM voltage and as a function of the gain for GEM-MIGAS with induction region lengths of: 50, 100, 200, 250 and 300 µm.

6.4.1 50 µm Induction region gap

The ion back-flow (IBF) measured for the 50 µm induction gap is represented in Figure 6. 9 a) as a function of V_{GEM}, for induction fields in the range of 5 to 50 kV/cm and E_{drift}=0.5 kV/cm. For each E_{ind} value the IBF improves as the voltage applied to the GEM increases, as expected since more ions are captured by the top-GEM electrode. In addition, the E_{ind} increase contributes to a considerable IBF reduction, from ~60% to 16% (at 5kV/cm and 50 kV/cm, respectively) for a GEM voltage of 425V. The increase in E_{ind} reduces the focusing effect of the field lines from the induction region into the GEM holes, reducing the IBF as a result of electron diffusion during the avalanche processes in the induction gap.

In Figure 6. 9 b), the IBF values of figure (a) are depicted as a function of charge gain (measured by varying V_{GEM}), where it is observed an IBF improvement as the gain increase, for the reasons referred above.

The effect of the drift field in the IBF is depicted in Figure 6. 9 c) where IBF is plotted as a function of charge gain (measured by varying V_{GEM}), for E_{drift} values between 0.1 to 0.75 kV/cm, and E_{ind}=50 kV/cm. As observed, IBF improves for lower values of the drift field, achieving 2.5% for E_{drift}=0.1 kV/cm, while at E_{drift}=0.75 kV/cm it is about 20 %. As ion diffusion in gases is low, the ions will follow approximately the field lines and an increasing number of field lines exiting the holes will end up in the GEM-top electrode as the drift electric field is reduced. This allows a decrease on the back-flow of ions to the drift region.

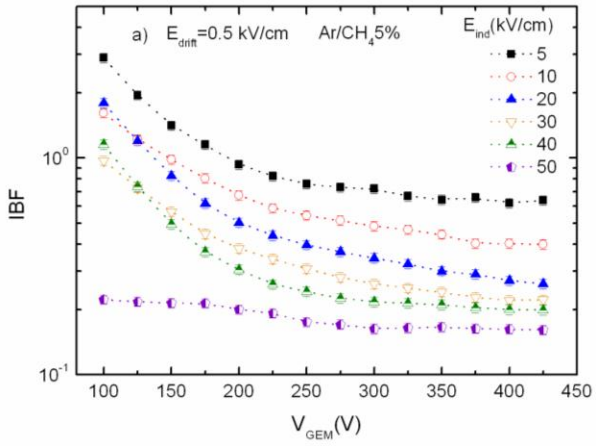

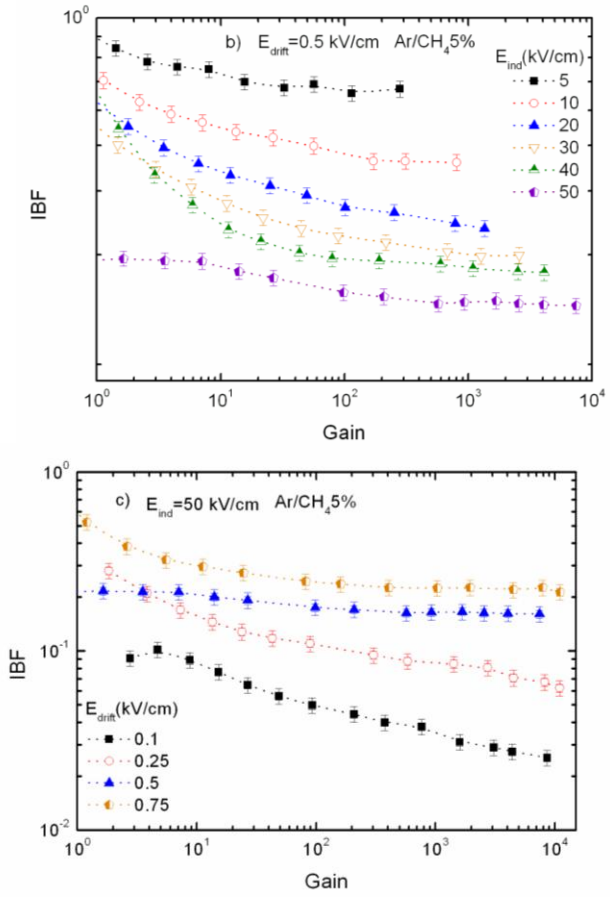

Figure 6. 9 - The ion back-flow ratio for 50 μm induction gap as a function of (a) V_{GEM} and (b) charge gain, both for different E_{ind} values and for E_{drift}=0.5 kV/cm. (c) Ion back-flow ratio for 50 μm induction gap as a function of charge gain for different E_{drift} and for E_{ind}=50 kV/cm. The errors are within the symbols.

6.4.2 100 μm Induction region gap

For the 100 μm GEM-MIGAS IBF is depicted in Figure 6. 10. Figure 6. 10 a) shows the IBF as a function of V_{GEM} for induction fields in the range of 5 to 50 kV/cm and E_{drift}=0.5 kV/cm. As observed, IBF improves as V_{GEM} augments until 250V, remaining practically constant for values above. It is however observed a slight increase for the highest GEM value applied. The increase of the induction field leads to a significant IBF improvement. IBF decreases from values in the order of 70% at 5kV/cm to values in the order of 10% at 40kV/cm. The best value was 11% obtained for E_{ind}=40 kV/cm and V_{GEM}=300V.

In Figure 6. 10 b) IBF is depicted as a function of E_{ind} for different drift fields from 0.1 to 1 kV/cm. In this configuration, the maximum induction field was a little higher, 47.5kV/cm, compared to the 40kV/cm of figure (a). This E_{ind} increase will affect positively the IBF values. For E_{drift}=0.5kV/cm and V_{GEM}= 350V, the lowest IBF value for E_{ind}=47.5 kV/cm was around 9%, which corre-

sponds to an absolute improvement about 3%, relative to the 11% measured for E_{ind}=40kV/cm for the same E_{drift} and V_{GEM} values.

The drift field reduction contributes to a considerable IBF reduction and a value of 1.2% was measured for the lowest E_{drift} value applied 0.1 kV/cm, at E_{ind}= 47.5 kV/cm.

The IBF behaviour as a function of gain is represented in Figure 6. 10 c), for different E_{drift} values and V_{GEM}=350V. It is evident an IBF improvement as gain increases.

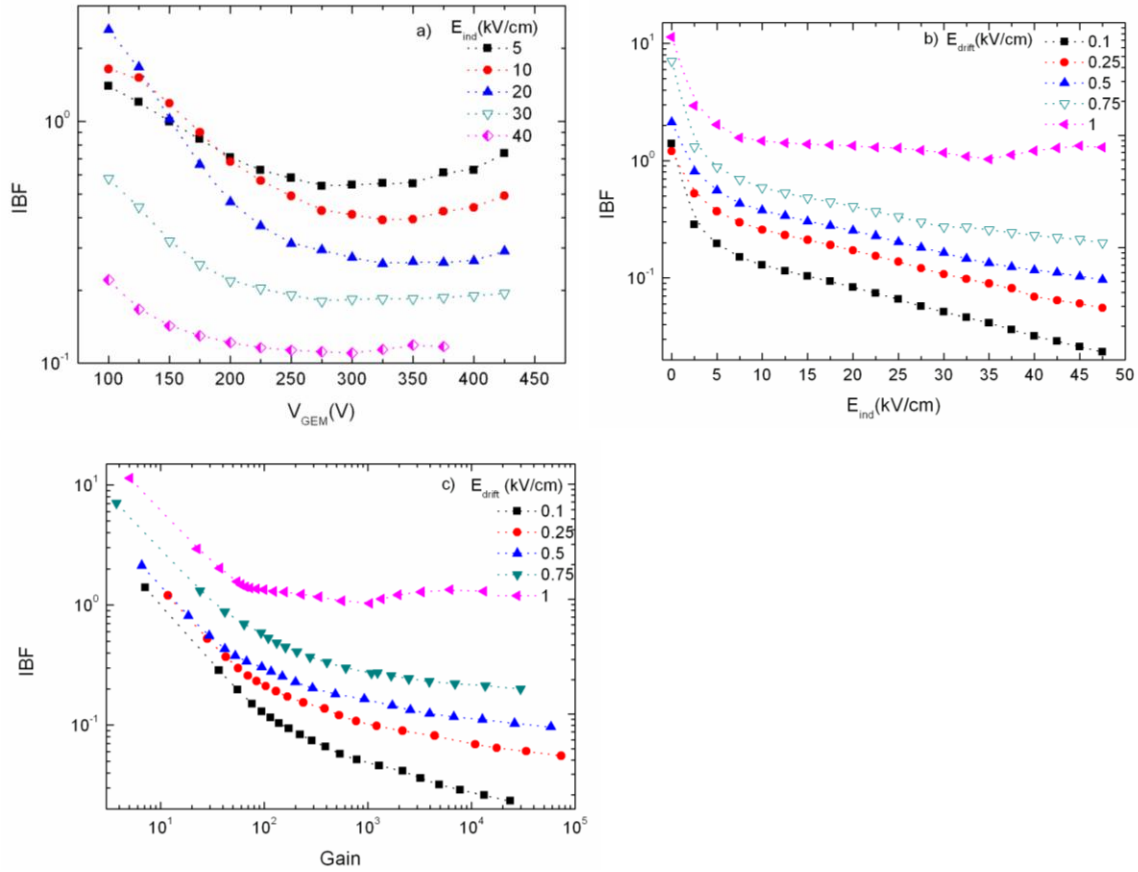

Figure 6. 10 - Ion back-flow for 100 µm induction gap as a function of: a) V_{GEM} for different E_{ind} values and E_{drift}=0.5 kV/cm, b) E_{ind} and c) charge gain, both for different E_{drift} values and V_{GEM} =350 V.

6.4.3 200 µm Induction region gap

The IBF behaviour was studied for the 200 µm induction gap configuration and is depicted in Figure 6. 11.

Figure 6. 11 a) depicts IBF as a function of V_{GEM} for induction fields between 5 to 30 kV/cm and for E_{drift}=0.1kV/cm. The augment of V_{GEM} contributes to an IBF decrease, behaviour observed up to a GEM voltage of 300 V, above which IBF remains practically constant. The induction field effect on the IBF values is

obvious, there is a decrease from values around 9% at 5kV/cm to values of the order of 2% at 30 kV/cm. The best value was approximately 1.6% for V_{GEM}=300V and E_{ind}=30 kV/cm.

In Figure 6. 11 b), IBF is depicted as a function of E_{ind} for V_{GEM}=350 V and different E_{drift} values, in the range of 0.1 to 1 kV/cm. The induction field augment leads to a reduction on IBF, as it was observed in previous graph. The best IBF values correspond to the lowest E_{drift} field configuration, where a value of 1.4% was measured for E_{drift}=0.1 kV/cm. This is a considerable progress, attending to the value of 16% measured for E_{drift}=1kV/cm, or 9% measured for E_{drift}=0.5 kV/cm.

The relation between IBF and gain is depicted in Figure 6. 11 c) for different drift fields. As expected, the minimum IBF value is obtained for higher gains.

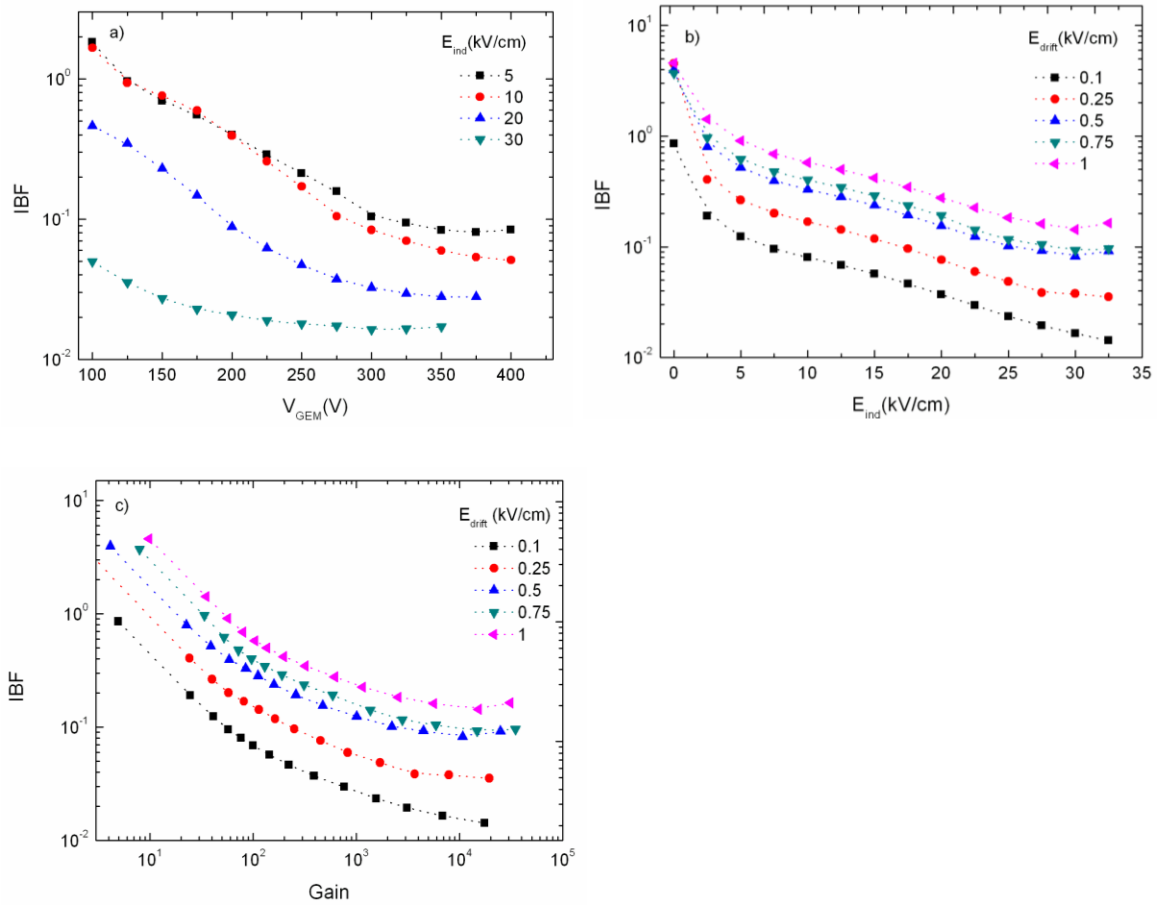

Figure 6. 11 - Ion back-flow for 200 µm induction gap as a function of: a) VGEM for different Eind values and Edrift=0.1 kV/cm; b) Eind and c) charge gain, both for different Edrift values and VGEM =350 V.

6.4.4 250 μm Induction region gap

The IBF results obtained for the 250 μm GEM-MIGAS configuration are depicted in Figure 6. 12. In figure a) the IBF is represented as a function of V_{GEM} for E_{ind} values between 5 to 30 kV/cm and a drift field of 0.5 kV/cm. The best IBF value is about 6 %, achieved for V_{GEM}=350 V and an induction field of 30 kV/cm, which is a good improvement attending to the 48% measured at 5kV/cm for the same GEM voltage.

The IBF measurement for different drift fields, with V_{GEM}=350V, are depicted in Figure 6. 12 b). The decrease on the drift field to 0.1 kV/cm leads to an IBF value of 1.5%.

The IBF behaviour as a function of gain is depicted in Figure 6. 12 c), where it is visible the typical IBF improvement as gain increases.

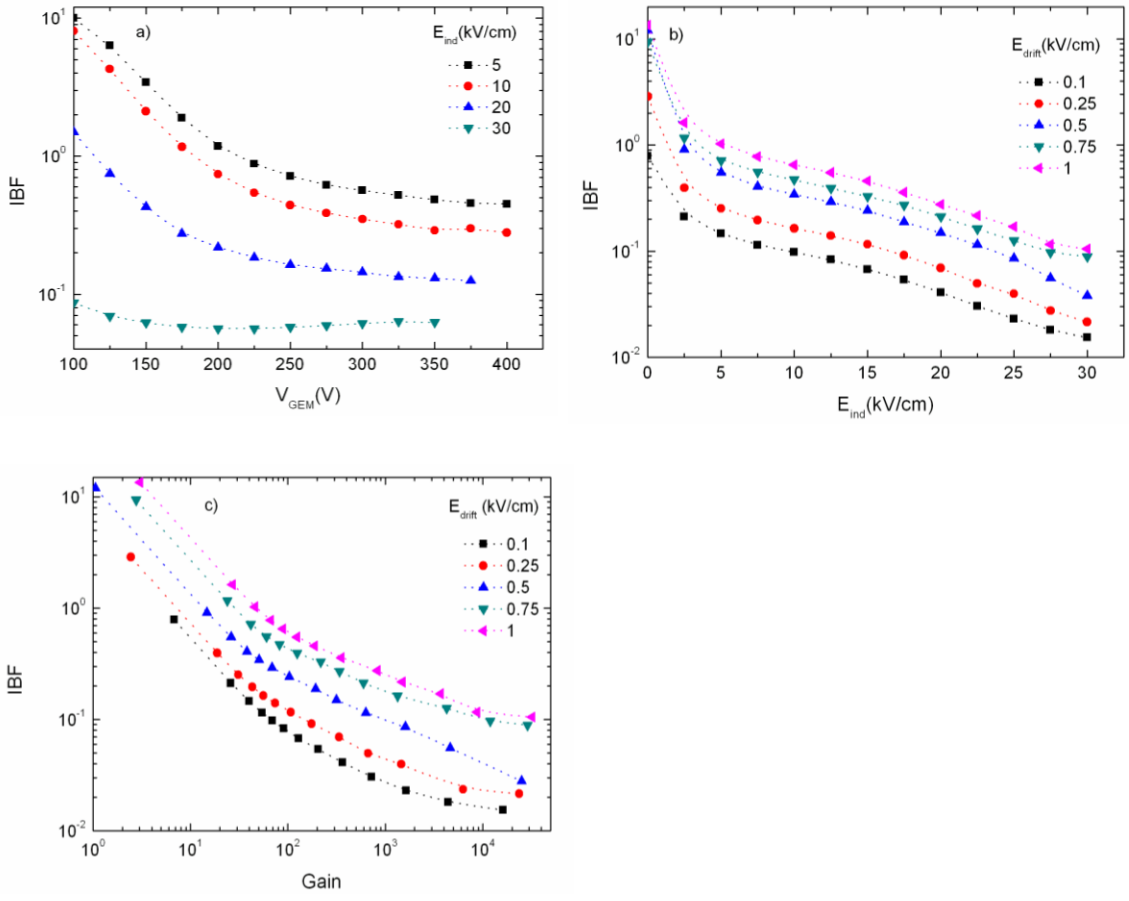

Figure 6. 12 - Ion back-flow for 250 μm induction gap as a function of: a) V_{GEM} for different E_{ind} values and E_{drift}=0.1 kV/cm; b) E_{ind} and c) charge gain, both for different E_{drift} values and V_{GEM} =350 V.

6.4.5 300 μm Induction region gap

The highest induction region length studied was 300 μm. The IBF performance obtained in this case as a function of induction field and gain is depicted in Figure 6. 13 a) and b), respectively, for a fixed GEM voltage of 350V.

IBF improves with increasing E_{ind}, as seen in all GEM-MIGAS configurations studied. The best value was around 1.3% for E_{drift} =0.25kV/cm.

The IBF behaviour as a function of charge gain demonstrates an improvement with gain, like it was observed for the other gaps.

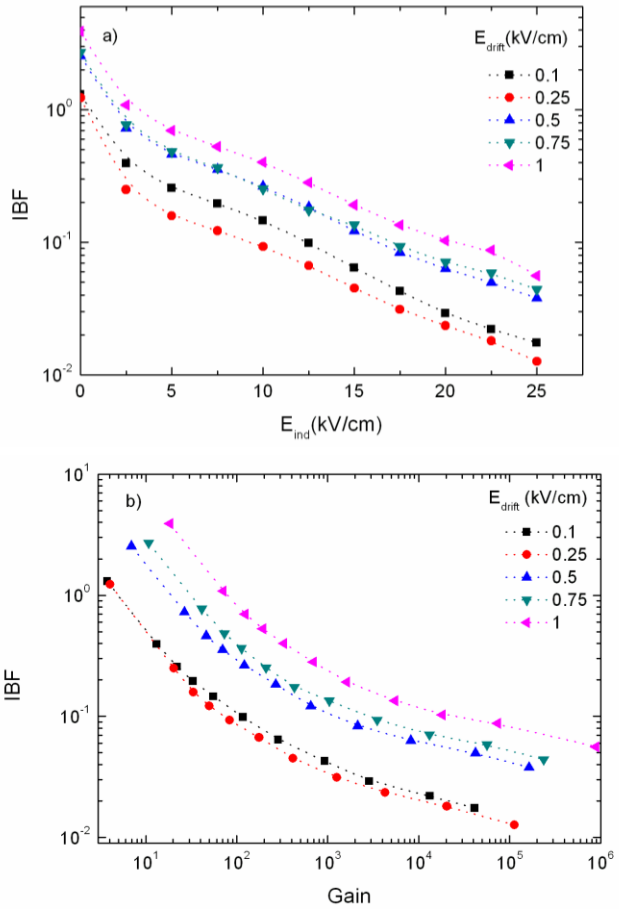

Figure 6. 13 - Ion back-flow for 300 μm induction gap as a function of: a) E_{ind} and b) charge gain, for different E_{drift} values and V_{GEM} =350 V.

6.4.6 Summary

The IBF performance has a similar behaviour for the several induction region gaps, improving with the increase on GEM voltage and induction field. The best IBF values are obtained for the lower E_{drift} configuration. With the increase of the GEM voltage more ions are captured by the top-GEM electrode which contributes to an improvement of IBF. In addition, the induction field augment

contributes to a considerable IBF improvement, since it reduces the focusing effect of the field lines from the induction region into the GEM holes. As a result, IBF is reduced due to electron diffusion during the avalanche processes in the induction gap.

In order to compare the performance of each GEM-MIGAS configuration, a compilation of the IBF behaviour as a function of induction field and gain is presented. Figure 6. 14 depicts the IBF performance as a function of E_{ind} for E_{drift}=0.1 kV/cm (Figure 6. 14 a) and E_{drift}=0.5 kV/cm (Figure 6. 14 b), while in Figure 6. 15 the IBF values of Figure 6. 14 are depicted as a function of charge gain. The induction gaps are in the range from 50 to 300 μm. For all the measurements the GEM voltage was kept constant at 350 V.

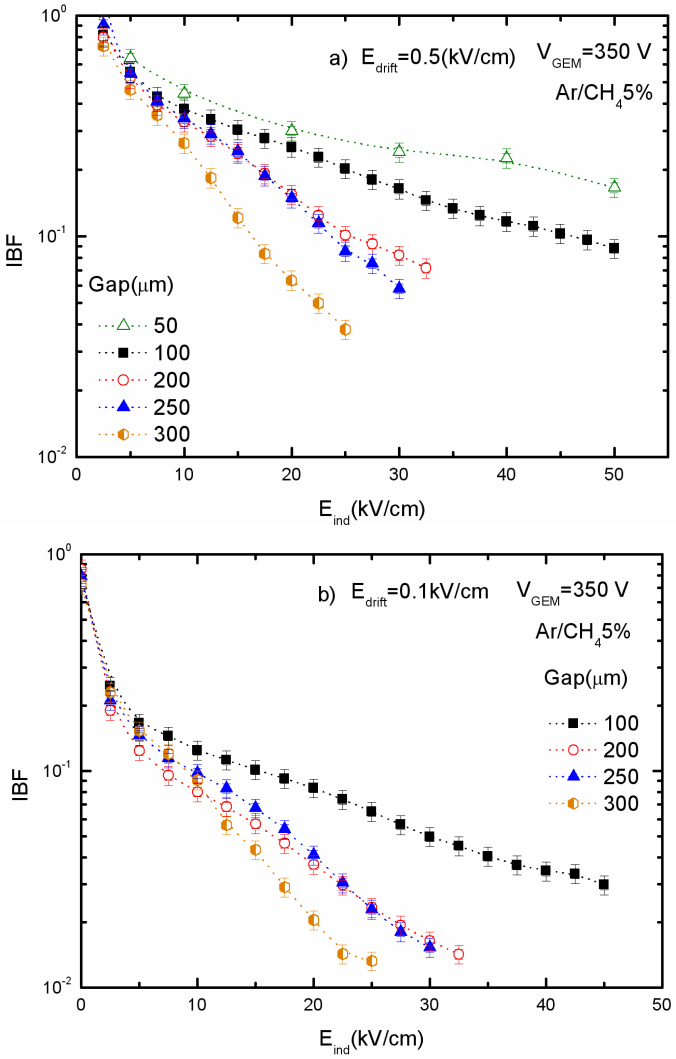

Figure 6. 14 - The ion back-flow, IBF, as a function of Eind for different induction gaps in the range of 50–300 μm and for VGEM=350 V: (a) Edrift=0.5kV/cm and (b) Edrift=0.1kV/cm.

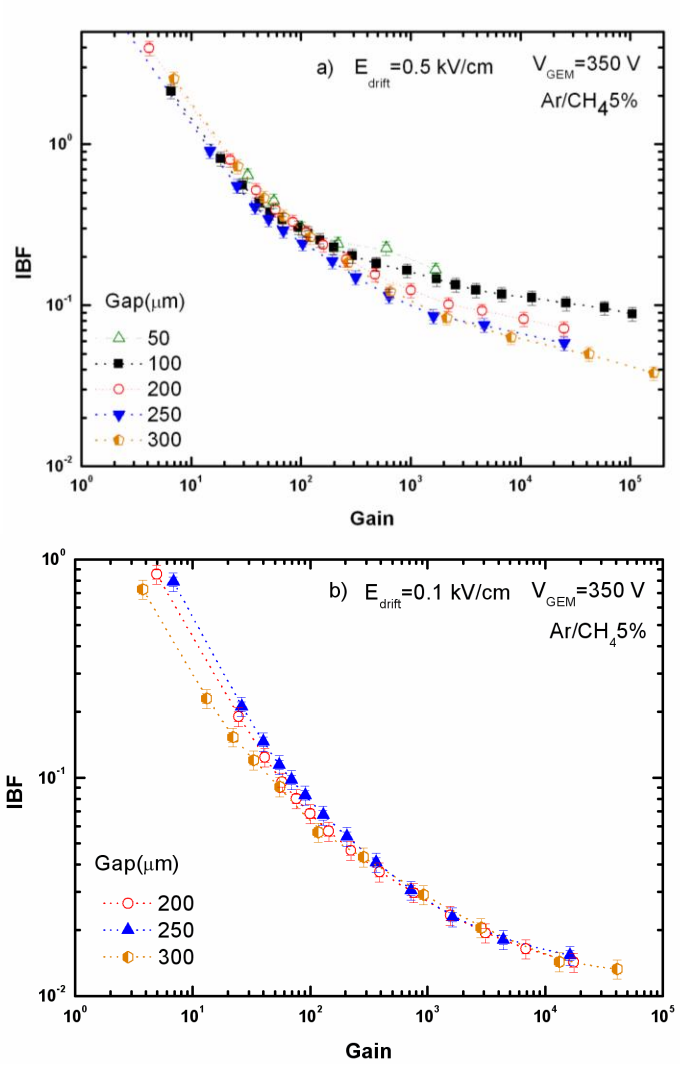

Figure 6. 15 - Ion back-flow as a function of charge gain for different induction gaps in the range 50-300 μm, for V_{GEM}=350 V: a) E_{drift}=0.5kV/cm and b) E_{drift}=0.1kV/cm.

As already mentioned IBF decreases with E_{ind} and gain, for all the gaps. It is also observed an IBF improvement as the gap thickness increases.

For the smaller induction region thickness (50 μm) the best IBF values were about 16% and 3%, obtained for E_{drift} values of 0.5 kV/cm and 0.1 kV/cm, respectively. The increase of the induction region gap allows a considerable improvement of IBF. For the 300 μm gap, it was achieved an IBF of about 4% and 1.5%, for E_{drift} values of 0.5 kV/cm and 0.1 kV/cm, respectively. The IBF enhancement is more accentuated for E_{drift}=0.5kV/cm, where it is noticed a decrease of about four times from the 50 μm gap to the 300 μm gap configuration. For the 0.1 kV/cm drift field configuration the improvement is only about two times. The IBF improvement with increasing induction gap thickness is a consequence of the diffusion of the avalanche electrons and the increase of the charge gain as the induction gap increases. The electron cloud transverse diffusion in Ar/CH4 (95/5%) [30] is about 11 μm and ~39 μm (rms) for the 50 μm

and 300 μm gaps , respectively [91]. The increase in E_{ind} reduces the focusing effect of the field lines of the induction region into the GEM'holes, owing to electron diffusion during the electron avalanche processes in the induction gap, as a consequence the IBF reduces.

The reduction on the drift field will reduce the back-flow of ions to the drift field, since ion diffusion in gases is low, the ions will follow approximately the field lines and an increasing number of field lines exiting the holes will end in the GEM-top electrode as consequence the number of ions that achieve the drift volume decreases.

The values achieved for the 50 μm configuration are similar to the total IBF achieved in a single MHSP [41] and result in a 4-fold suppression of IBF relativel to a single-GEM .

The values obtained for the ion back-flow in GEM-MIGAS are similar to those obtained in a triple-GEM configuration in Ar/CH_4, for E_{drift}=0.5 kV/cm and charge gain ~10^5 [28], and in a Micromegas operating in Ar with 2-3% CH_4 [17]. A 4-GEM configuration achieved an IBF of about 3% for a gain ~10^5 and E_{drift}=0.5kV/cm [29]. One of the best IBF achieved in electron multiplier cascades were obtained from a configuration combining a Flipped-MHSP/GEM/MHSP, with an IBF value of 0.02% at gains ~10^4, for Edrift=0.2 kV/cm [31]. Nevertheless, IBF values of few percent are low enough to allow a safe operation of CsI-photocathodes in GPMs.

Table 6. 1- Resume of the best IBF and gain values obtained for the different GEM-MIGAS configuration.

GAP (μm)	Maximum Gain	Lowest IBF	V_{GEM}(V)
50	11045 E_{drift}=0.75 kV/cm, E_{ind}=50 kV/cm	0.020 E_{drift}=0.1 kV/cm, E_{ind}=50 kV/cm	425
100	30739 E_{drift}=1 kV/cm, E_{ind}=45 kV/cm	0.029 E_{drift}=0.1 kV/cm, E_{ind}=45kV/cm	350
200	34778 E_{drift}=0.75 kV/cm, E_{ind}=32.5 kV/cm	0.014 E_{drift}=0.1 kV/cm, E_{ind}=32.5 kV/cm	350
250	32334 E_{drift}=1 kV/cm, E_{ind}=30 kV/cm	0.015 E_{drift}=0.1 kV/cm, E_{ind}=30 kV/cm	350
300	885647 E_{drift}=1 kV/cm, E_{ind}=25 kV/cm	0.012 E_{drift}=0.1 kV/cm, E_{ind}=25 kV/cm	350

6.5 Conclusions

The GEM-MIGAS performance operating in Ar/CH_4 (95/5%) was evaluated in terms of charge gain and ion back-flow reduction for induction gap thicknesses ranging from 50 to 300 μm.

It was successfully demonstrated that increasing the induction gap of the GEM-MIGAS multiplier from 50 μm to 300 μm higher gains are achieved, gains above 10^5, sufficient for the detection of single electrons with high detection efficiency. The IBF is reduced by a factor of 5, down to the few percent level. The electron diffusion in the gap explains the capability of the GEM-MIGAS to reduce the ion back-flow and its correlation with the gas mixture characteristics, such as electron transverse diffusion and electron multiplication in the induction gap. Minimum IBF values were achieved for the 300 μm gap, 4% for E_{drift}=0.5 kV/cm and 1.5% for E_{drift}=0.1kV/cm.

The values obtained for ion back-flow to the drift volume, in GEM-MIGAS, are similar to those obtained in triple-GEM configurations and in a Micromegas, but are much higher than those obtained in a flipped-MHSP/GEM/MHSP electron multiplier cascade (IBF ~ 0.02% at gains of 10^4 and E_{drift}=0.2 kV/cm).

The IBF measurements demonstrate that the IBF improves with increasing induction field. The advantage of the GEM-MIGAS is the simplicity compared to other cascade configurations, delivering higher gains and similar IBF values. However, the increase in the pulse duration due to the drift of positive ions in the 300 μm induction gap may be a drawback in some applications.

Chapter 7

GEM-MIGAS for Neutron Detection

In this section the GEM-MIGAS performance will be evaluated in order to check its viability as thermal neutron detector.

The work focus the optimization of the induction region thickness and the influence of the GEM parameters on the achieved gain, both performed in pure CF_4 at different pressures. Finally, the GEM-MIGAS configuration with better performance was operated in a CF_4-He mixture.

7.1 Introduction

The development of thermal neutron detectors is important for applications such as nuclear industry, material research, imaging and medical physics. A new generation of neutron gaseous detectors for accelerator based sources (spallation sources) is under development at various laboratories, requiring microsecond time resolution, millimetre position resolution, low gamma sensitivity and count rates up to 1MHz/mm^2. These efforts will lead to the next generation of position-sensitive thermal neutron detectors (see [53][56] and references there in). Gaseous detectors based on micropatterned electron multipliers are good alternatives for this purpose, using ^{3}He gas for thermal neutron detection due to its low gamma sensitivity and high efficiency to neutron capture. Boron Trifluoride ($^{10}BF_3$) can be also used as a detection medium, but its operation at high pressure is problematic due to electron attachment. For high detection efficiency the helium pressure must be increased.

The neutron capture reaction with ^{3}He is:

$$^3He + ^1n \rightarrow ^3T + ^1p + 0.764MeV \quad (7.1)$$

The nuclear interaction of a thermal neutron with an atom of ^{3}He releases 764 keV of energy, which is shared between two ionizing particles, the proton (573 keV) and the triton (191 keV), emitted in opposite directions.

The position resolution of neutron detectors based on ^3He is limited by the range of the reaction products in the gas, the 573 keV proton and 192 keV triton. Since the reaction products deposit their energy in the gas in an asymmetric way, the interaction position can only be determined with a precision directly proportional to their range in the gas [54]. To reduce this range, stopping gases having heavy molecular weight and low gamma sensitivity are added to ^3He to reduce the proton and triton ranges.

Therefore, stopping gases like CF_4 and CH_4 are used at high pressures. They also act as quenchers for He scintillation and provide high electron drift velocities and low electron diffusion [52],[76]. To have a 1 mm thermal neutron position resolution, a pressure of about 2.6 bar is required for CF_4 and CH_4 [76]. Figure 7. 1 shows the proton and tritium ranges for 2.6 bar of CF_4. Figure 7. 2 and Figure 7. 3 depict the energy lost by the proton and the tritium, respectively, for CF_4 pressures of 1 and 2 bars. The use of Ar at high pressure was also proposed [53], with the advantage of having a full noble gas mixture, easy to handle and to purify in a closed system, but requiring higher filling pressures, of the order of 6 bars. Xenon can also be used but it is less attractive because it has relatively high gamma-ray sensitivity.

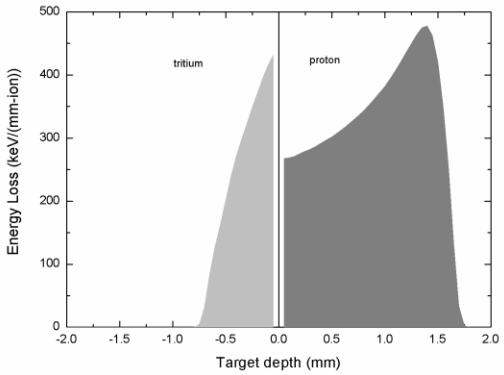

Figure 7. 1- Proton and Tritium Range for 2.6 bar of CF_4.

The MicroStrip Gas Chamber (MSGC) [4] was the first gaseous micropattern detector to be used for thermal neutron detection [52]. The GEM [11] has also been the subject of many studies for neutron detection [54] [76]. High charge gains could not be achieved at high pressures [54] [57][76], but the readout of the scintillation produced in the electron avalanches, using a CCD camera, allowed the development of GEM-based neutron detectors [55][56]. To the best of knowledgement, there is a single citation in the literature of studies with Micromegas [9] operation in CF_4, where the operation above 2.4 bar was not possible [77]. It is expected that higher CF_4 pressure may be feasible using the new

type of bulk Micromegas [67]. Previous studies of a hybrid microstructure, the Micro Hole & Strip Plate (MHSP) [78], which merges the GEM and a MSGC in a single micropattern structure [79], have shown that the MHSP could operate at much high CF_4 pressure (~ 2.6 bar) than using a single conventional GEM [80].

In this work, it is investigated the viability of another hybrid configuration, the GEM-MIGAS, as a neutron gaseous detector with gaps in the 20-250 μm range, in pure CF_4 for the pressure of 1, 2 and 2.6 bar. The influence of the GEM hole diameter in the gain is also evaluated.

The CF_4 properties make it a suitable choice, since it acts as a quenching gas, provides high electron drift velocities, low electron diffusion and it is a good and fast scintillator. The molecules of the stopping gas must have a high collision cross section for fast charged particles, such as the proton or triton. Increasing the CF_4 pressure has several advantages:

- The localization error due to the drift between the neutron interaction position and the centre of the charges is reduced;
- The number of tracks interacting with the detector wall is reduced;
- By concentrating the primary charge cloud in a smaller volume, the dead time of the detector is reduced. As the drift velocity of electrons in He-CF_4 mixtures increases with the CF_4 concentration, increasing its partial pressure contributes also to the dead time reduction.

CF_4 is used for its short attenuation thickness, however it contains Freon impurities which are electronegative and corrosive, so the gas needs to have a very high purity.

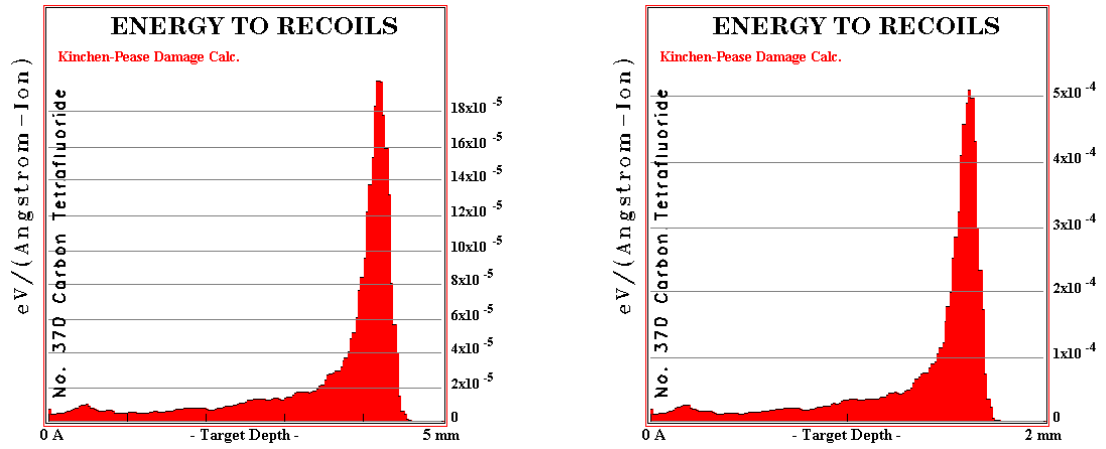

Figure 7. 2- Energy lost by the proton for 1 bar (a) and 2.6 bars (b) of CF_4.

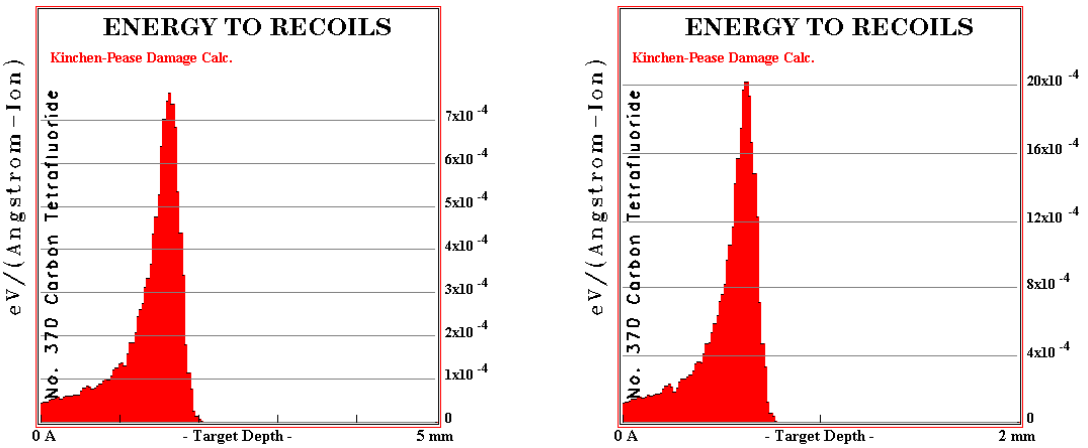

Figure 7. 3 - Energy lost by the tritium for 1 bar (a) and 2.6 bars (b) of CF_4.

Optimization of GEM-MIGAS induction region length:

The GEM-MIGAS performance in pure CF_4 will be evaluated for induction region lenght of 20, 30, 50, 150 and 250 μm for different gas pressures (1, 2 and 2.6 bar) using a standard GEM. The goal is to choose the induction region length with better performance, in terms of charge gain t and operation stability, mainly at high CF_4 pressure.

Calculations relying on experimental data show that the best gains would be achieved for induction gaps around 50 μm [35]. Nevertheless, as the maximum voltages applied to micropattern devices are limited by the onset of discharges, the effective gains achieved in these multipliers are higher for larger induction gaps. For the GEM-MIGAS operating at 1 atm of He-15% isobuthane, the highest charge gains, achieved before the onset of detector instabilities, were obtained for a gap thickness between 150 and 300 μm, reaching values around 10^6 [38]. However, for high pressure operation, the applied voltage increases and it can compromise a stable operation of the structure, due to the increase of the discharge probability.

On the other hand, the optimum Micromegas gap, sustaining highest charge gains with low statistical fluctuations, for atmospheric pressure operation, is well known to lay in the 50 to 100 μm region [35]. Induction gaps greater than 100 μm are suited for low pressure micromegas operation [81], while gaps shorter than 50 μm may achieve higher gains at high pressures [9]. Therefore, the GEM-MIGAS gain was investigated for induction gap thicknesses of 20, 30, 50, 150 and 250 μm, in 1, 2 and 2.6 bar of pure CF_4. These measurements were taken with a type 1 standard GEM with 50 μm hole diameter and 140 μm pitch.

Influence of the GEM Parameters:

The influence of the GEM geometry, on the GEM-MIGAS performance is evaluated for different hole diameters of 50, 40 and 30 μm. Table 7. 1 summarises the different GEM geometries; the standard GEM (50 μm hole diameter) as well as GEMs with hole diameters of 40 and 30 μm.

Table 7. 1- GEM geometrical designs used in this work

GEM Type	Kapton thickness (μm)	Hole Diameter (μm)	Pitch (μm)
1	50	50	140
2	50	40	70
3	50	30	50

A decrease in the GEM hole diameter leads to higher electric fields inside the holes for lower applied voltages. Consequently, higher gains are expected when using smallest GEM hole diameters [54][55][21].

At high pressure it is expected a better performance for the smaller diameter GEM, given that the electron cloud is smaller, which implies lower charge loss from the GEM hole. The electric field threshold for gas multiplication increases for higher pressure, so the high electric field achieved in small hole diameters can be an advantage.

Helium measurements:

The helium measurements will be made using the best GEM-MIGAS configuration, in terms of induction region length and GEM hole geometry. Fixing the CF_4 pressure at 2.6 bar, helium is gradually added in step of 1 bar. Regular helium will be used since the ^3He is expensive and right now is very difficult to buy, however the results obtained with ^4He are valid. Since the tests will be made with X-rays, using regular He does not compromise the validation for a possible application on neutron detection, as the present study are concentrated in the charge amplification gain that can be achieved with this microstructure configuration.

Finally, is investigate the GEM-MIGAS gain for a 50 μm induction gap geometry and a GEM with 30 μm hole diameter, using 2.6 bar of CF_4 added to 1 and 2 bar of helium.

7.2 Experimental Setup

The GEM-MIGAS was mounted inside a stainless-steel cylindrical chamber with a Mylar window, 5 mm thickness, in the top surface and four SHV-connectors on the bottom face, used as feedthroughs. A photograph with the GEM-MIGAS and drift electrode assembled in the chamber bottom face is depicted in Figure 7. 4.

The chamber was connected to a vacuum/gas system and pumped down to 10^{-6} mbar range before filling. The gas circulation was maintained by convection through SAES St707 getters, operated at 110ºC. The detector was irradiated with an X-ray beam from a ^{55}Fe source and collimated to 1 mm in diameter.

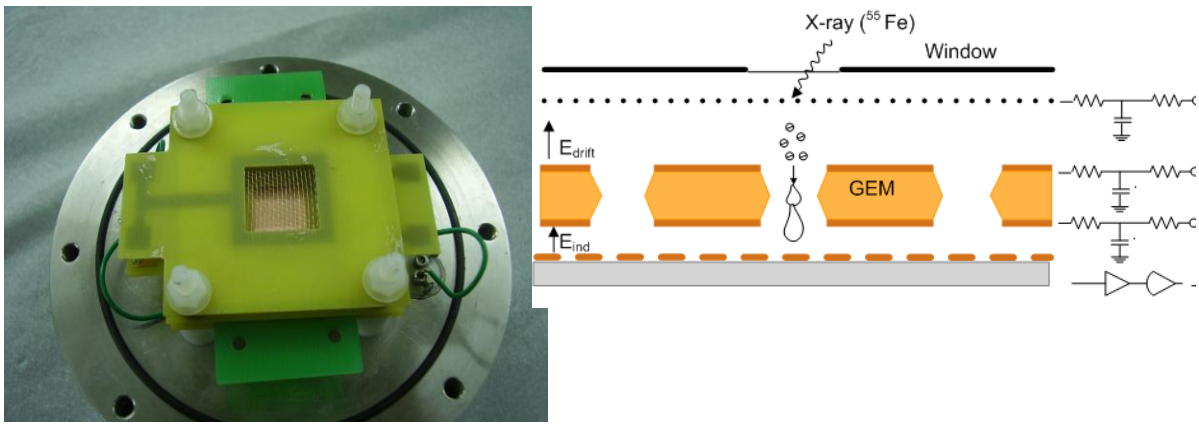

Figure 7. 4- Photograph e of the detector and schematic diagram of GEM-MIGAS detector.

The GEM-MIGAS electron multiplier has an active area of 10×10mm^2. Three different GEM designs were used in these studies, all manufactured at CERN: the standard GEM (50 µm hole diameter) as well as GEMs with hole diameters of 40 and 30 µm (see Table 7.1).

In order to examine the effect of the induction gap thickness on gain, induction gap values between 20 to 250 µm were used.

The drift region, between the top GEM electrode and the grid, has 5 mm thickness. The drift electrode and the GEM electrodes were operated with negative voltages while the micromesh was set to ground. The signals from the micromesh were fed through a Canberra 2006 preamplifier (sensitivity of 1.5 V/pC) and the preamplifier output was then fed into an amplifier (Canberra, model 2025) with shaping time constants adjusted to 0.5 µs. The amplifier output was fed into a Nucleus PCA-II multichannel analyzer.

The electronic chain sensitivity was calibrated for absolute gain determination using a calibrated capacitor directly connected to the preamplifier input as well as to a precision pulse generator (see section 4.2.1). The charge gain was deter-

mined from the obtained pulse-height distributions. A 100% electron transmission through the GEM-holes was assumed and a w-value of 54 eV and 41 eV was taken for CF_4 and He, respectively [82]. To calculate the w value for 2.6 bar CF_4/1 bar He and 2.6 bar CF4/2 bar He gas mixtures we use the empirical model for binary mixtures[83].

7.3 Optimization of GEM-MIGAS induction region gap

The charge gain and energy resolution will be measured as a function of the GEM voltage for fixed induction field value and as a function of the induction field for a fixed GEM voltage. The measurement will be done in pure CF_4 for 1, 2 and 2.6 bar, with induction region gap lengths of 20, 30, 50, 150 and 250 μm..

7.3.1 250 μm Induction region Gap

The charge gain was measured as a function of GEM voltage and is represented in Figure 7. 5 for different induction fields, in the range of 5 to 30kV/cm, and CF_4 pressures of 1, 2 and 2.6 bar. The gain exhibits an exponential dependence on GEM voltage, as expected. The measurements were done also for a configuration where the bottom GEM electrode is connected to the grid, in short circuit (sc), which is an approach to single GEM mode operation, being useful for comparison with the GEM-MIGAS mode. The E_{drift} was kept at 0.5kV/cm for at 1 and 2 bar and at 0.3kV/cm for 2.6 bar pressure.

At 1 bar, the maximum gain is approximately $2.5x10^4$, achieved for the highest induction field value, 30 kV/cm, and a GEM voltage of 775V. For induction fields up to 10kV/cm, the gain is lower than the one achieved for the sc configuration. Only for E_{ind} values above 20 kV/cm the gain exceeds the sc values. The increase of the induction field leads to a gain improvement from $5 x10^3$ to $2.5x10^4$ for 5 and 30 kV/cm, respectively, for V_{GEM}=775V.

The increase of the CF_4 pressure up to 2 bar is followed by an increase of GEM voltage up to about 700V compared to the 550V at 1 bar. The maximum gain was ~$7x10^3$ for V_{GEM}=975V and E_{ind}=20kV/cm, the highest value. For induction fields up to 10 kV/cm, E_{ind} increase is not traduced in a gain improvement compared to the sc configuration. The induction field enhancement from 5 to 20 kV/cm is followed by a slight increase of gain, from 10^3 to $7x10^3$for V_{GEM}=975V.

The sc configuration allows collecting 100% of all electrons from the avalanche. However, this configuration is not desirable for most of the applications where the readout electrode is decoupled from the GEM-bottom electrode (e.g.

to have a 2D readout possibility). For low E_{ind} values part of the electrons produced in the avalanche are diverted to the GEM bottom electrode and the gain is smaller than that obtained with the sc configuration. Increasing E_{ind} the electron collection efficiency in the induction electrode increases and eventually becomes higher than 100% as electron multiplication take place in the induction gap, compensating for the possible loss of electrons produced in the GEM holes and further increasing the total charge gain when compared with the sc operation mode.

The detector operation at 2.6 bar was followed by some instabilities. Only a few measurements were feasible before the structure breakdown. In the first attempt E_{drift} was set at 0.5 kV/cm, with voltages above 2000V on the drift electrode. As a consequence, discharges became evident, compromising the detector operation at this drift field. To overcome this situation the drift field was decreased to 0.3 kV/cm, allowing detector operation for a while. However, after a period of time, discharges started again, the operation of the detector become irreversible. For this CF_4 pressure it was not possible to measure the gain in short-circuit mode given the low signal/noise ratio. The maximum gain achieved was about 400, measured at E_{ind}=10kV/cm and V_{GEM}=1100V. At E_{ind}=20kV/cm, the voltage applied to the GEM before breakdown is lower than at E_{ind}=10kV/cm.

The add up of CF_4 pressure is followed by a GEM voltage increase. At 1 bar the range is 550 to 775V, increasing to values from 700 to 1000V at 2 bar and at 2.6 bar the GEM voltage is between 900 and 1100V. A gain reduction is also observed from 10^4 at 1 bar to 10^3 at 2 bar and only a few hundred at 2.6 bars.

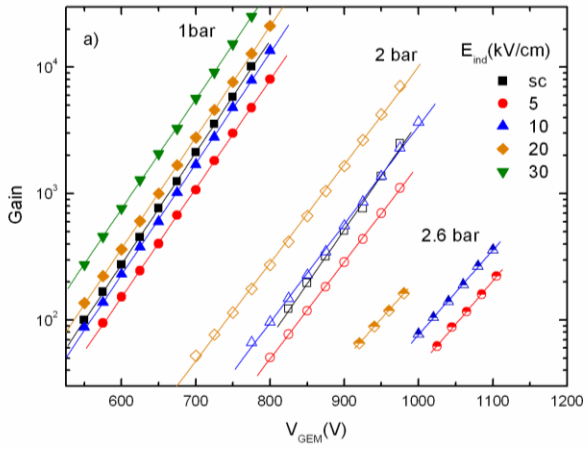

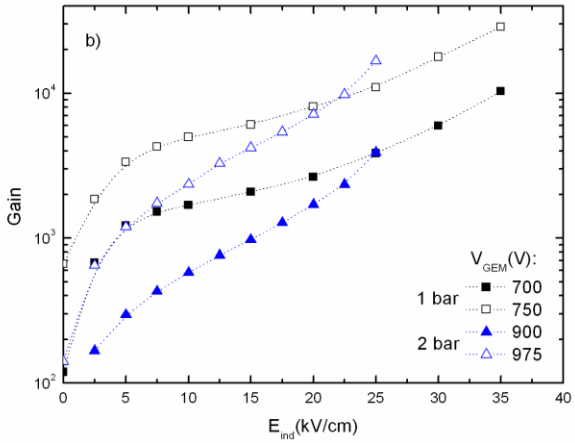

Figure 7. 5- Gain as a function of : a)V_{GEM} for different induction field values and sc mode; b) induction field for different GEM voltages and pressures. E_{drift} was kept at 0.5 k/cm for 1 and 2 bar and at 0.3kV/cm for 2.6 bar.

The gain as a function of induction field for fixed GEM values is depicted in Figure 7. 5 b). At 1 bar the maximum E_{ind} value was 35kV/cm, decreasing to 25kV/cm at 2 bar. It is obvious the gain enhancement as the induction field increases. However, at 1 bar curves show a smooth increase, being the impact of the E_{ind} increase for higher pressures.

The maximum gain values obtained are similar to the previus configuration, $2x10^4$ and $1x10^4$ for 1 and 2 bars , respectively.

The energy resolution, obtained for 5.9 keV X-rays, is depicted in Figure 7. 6 a) as a function of V_{GEM} for induction field values in the range of 5 to 30kV/cm. It is observed an improvement on the energy resolution with the GEM voltage up to the middle of the V_{GEM} range applied. For higher voltages, the energy resolution starts to deteriorate. At 1 bar, the best value was about 22%, achieved for the bottom GEM in short circuit with the grid and V_{GEM}=650V. The increase of the induction field, to values above 5 kV/cm, leads to the deterioration of the energy resolution, exceeding 30%. At 2 bar the best energy resolution was about 35%, measured for the sc configuration and a V_{GEM}=925 V, reaching values above 40% for induction fields higher than 5kV/cm. The best energy resolution at 2.6 bar was also around 35%, measured for E_{ind}=5kV/cm and V_{GEM}=1100V.

In Figure 7. 6 b) the energy resolution is represented as a function of the induction field for fixed GEM voltages, CF_4 pressures of 1 and 2 bar. The energy resolution improves with E_{ind} up to 10 kV/cm and the best values are achieved in the range of 10 to 20 kV/cm. For increasing E_{ind} values, up to 10 kV/cm, the improvement is due to the increase of the electron extraction efficiency from the GEM holes. For values between 10 and 20 kV/cm the electron extraction efficiency is not traduced in energy improvement. For E_{ind} values above 20 kV/cm

the increase of charge gain leads to energy resolution degradation. The energy resolution deteriorates as the CF_4 pressure increase, exhibiting a better performance for the low induction field configurations as well as low GEM voltages.

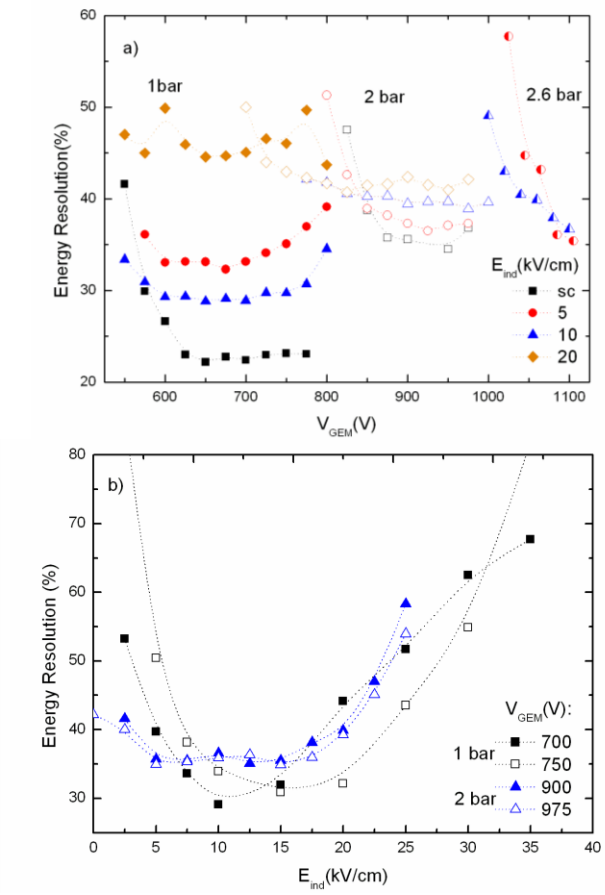

Figure 7. 6- a) Energy resolution at 1, 2 and 2.6 bar as a function of the GEM voltage for different induction field values. b)Energy Resolution as a function of the induction field for diferent GEM voltages and pressures. The E_{drift}=0.5 k/cm for 1 and 2 bars, 0.3 for 2.6 bar.

7.3.2 150 μm Induction region Gap

The charge gain obtained for the 150 μm induction gap geometry is depicted in Figure 7. 7 a) as a function of GEM voltage, for different induction field values. The measurements were performed for 1, 2 and 2.6 bar of CF_4 bars and E_{drift} was kept at 0.5 kV/cm at 1 and 2 bar and at 0.4 kV/cm at 2.6 bar.

As in the last case the short circuit configuration exhibits better performance than compared to the GEM-MIGAS mode for induction field values up to 10kV/cm. Higher E_{ind} values are traduced on gain enhancement.

At 1 bar the maximum gain is 1.2×10^4 for V_{GEM}=720 V and E_{ind}=30kV/cm. The increase of the CF_4 pressure to 2 bar leads to a gain reduction of about one order of magnitude, 10^3 for V_{GEM}=940 V and E_{ind}=20kV/cm. At 2.6 bar the gain obtained is only about 400 for V_{GEM}=1080 V and E_{ind}=10kV/cm.

The charge gain behaviour as a function of the induction field is depicted in Figure 7. 7 b). The maximum E_{ind} at 1 bar is 45 kV/cm, decreasing to 35kV/cm at 2 bar. At 2.6 bar the maximum E_{ind} is about 25kV/cm. The charge gain improve with the induction field enhancement, at 1 bar the best value is $6.2x10^4$, decreasing to $2.8x10^2$ at 2 bar and 865 at 2.6 bar.

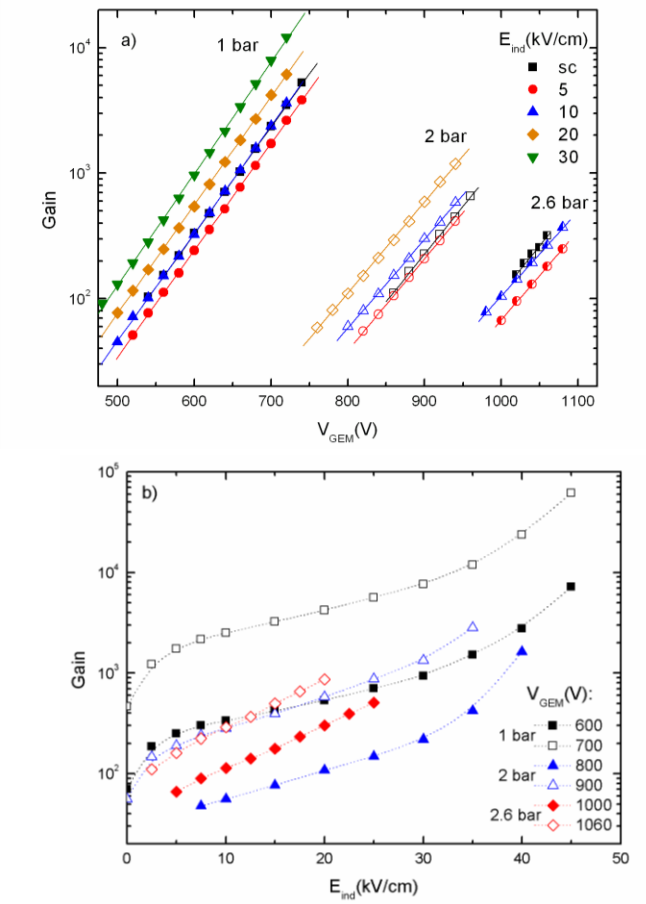

Figure 7. 7- Gain as a function of V_{GEM} for different induction field values a) and as a function of induction field for different GEM values. b) E_{drift}=0.5 k/cm for 1 and 2 bar and 0.3kV/cm for 2.6 bar.

The energy resolution obtained for the 150 µm gap is depicted in Figure 7. 8 a) as a function of V_{GEM}. An improvement on the energy resolution is obtained with increasing GEM voltage. At 1 bar the best values were about 20% for the sc configuration and V_{GEM}=725V. Nevertheless, the energy resolution for the other induction field curves is not very different, varying from 20 to 25 %. The increase on pressure is followed by degradation of energy resolution. At 2 bar the best energy resolution is about 30%, obtained for Eind in the range of 5 to 20 kV/cm. At 2.6 bar the best energy resolution is about 35% for 5 and 10 kV/cm induction fields. For the sc curve the energy resolution is worse as a result of the poor signal/noise ratio. This is more relevant at high pressure.

The energy resolution behaviour as a function of E_{ind}, is depicted in Figure 7. 8 b). It is evident an improvement of the energy resolution as E_{ind} increases, up to a certain value, above which it is observed a deterioration. At 1 and 2 bar, the deterioration occurs for values above 30kV/cm. The 2.6 bar curves are characterized by a smooth variation of energy resolution with E_{ind}. owing to the lower SNR, the energy resolution degradation occurs above higher E_{ind} values, as the pressure increases.

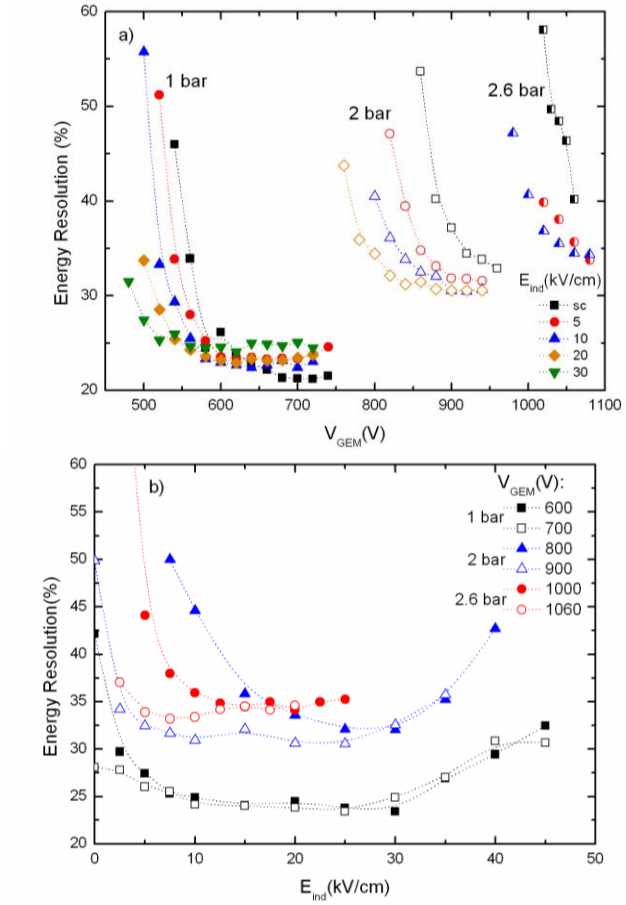

Figure 7. 8 – a) Energy resolution at 1, 2 and 2.6 bar as a function of the GEM voltage for different induction field values. b) Energy Resolution as a function of the induction field for different GEM voltages and pressures. The E_{drift}=0.5 k/cm for 1 and 2 bars, 0.3 for 2.6 bar.

7.3.3 50 μm Induction region Gap

Figure 7. 9 a) depicts the gain as a function of V_{GEM} for diferent induction field values for gas pressure of 1, 2 and 2.6 bar. E_{drift} was kept at 0.5 kV/cm for 1 and 2 bar and at 0.4 kV/cm for 2.6 bar in order to avoid discharges in the drift grid.

The gain increases exponentially with GEM voltage, improving also for high induction field configurations. The E_{ind} value at which the gain exceeds the sc configuration is about 30 kV/cm at 1 bar and 20 kV/cm at 2 and 2.6 bar. At

higher pressures the induction field contribution to the gain improvement is more significant than at atmospheric pressure.

The maximum gain at 1 bar is about 10^4 for V_{GEM}=775 V and E_{ind}=50 kV/cm, decreasing about one order of magnitude for 2 bar pressure, reaching $2x10^3$ for E_{ind}=50 kV/cm and V_{GEM} =990V. At 2.6 bar the maximum gain is approximately 400 for V_{GEM}=1075V and E_{ind} 50kV/cm. As expected, the gain decrease for the higher pressures.

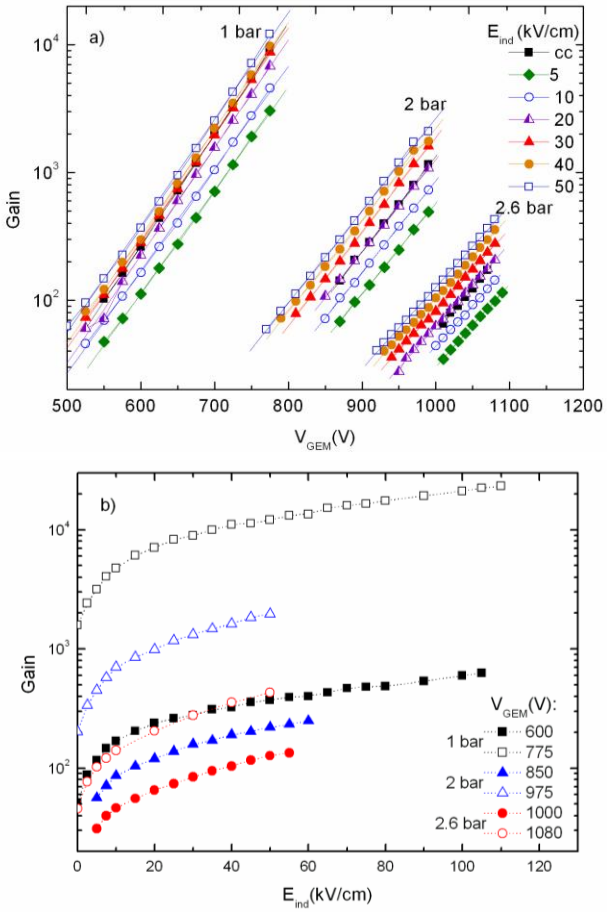

Figure 7. 9- Gain as a function of: a)V_{GEM} for different induction field values and pressures. b) Induction field for different V_{GEM} values and pressures. E_{drift}=0.5 k/cm for 1 and 2 bar and 0.3kV/cm for 2.6 bar.

The gain behaviour as a function of induction field is depicted in Figure 7. 9 b). For E_{ind} values up to 20-30kV/cm it is evident a considerable gain improvement, becoming smooth for higher E_{ind} values. However, the curves exhibit an exponential trend (linear curve in the log graph). For 1 bar, the maximum induction field applied before discharges was between 110 and 120 kV/cm, about 50 kV/cm more than the values applied in previous configuration (150 μm). However, this increase was not traduced in a significant gain improvement, as the highest gain is about 2×10^4. This is a consequence of the

shorter distance that the avalanche has to develop. For CF_4 pressures of 2 and 2.6 bar, the highest E_{ind} values were more or less the same as in the previous configuration. As result, the charge gain didn't improve.

The energy resolution is represented in Figure 7. 10 as a function of V_{GEM} (a) and the E_{ind} (b). The best values were obtained for the sc configuration were: 20, 30 and 40% at 1, 2 and 2.6 bar, respectively. It is observed a considerable deterioration on the energy resolution with increasing pressure.

At 1 bar the energy resolution is similar for all E_{ind} values except for the sc configuration. As observed in the figure (b), the increase of E_{ind} is not traduced on a deterioration of the energy resolution. At 2 and 2.6 bar the energy resolution does not exhibit such a smooth behaviour. There are significant differences for the several induction field values.

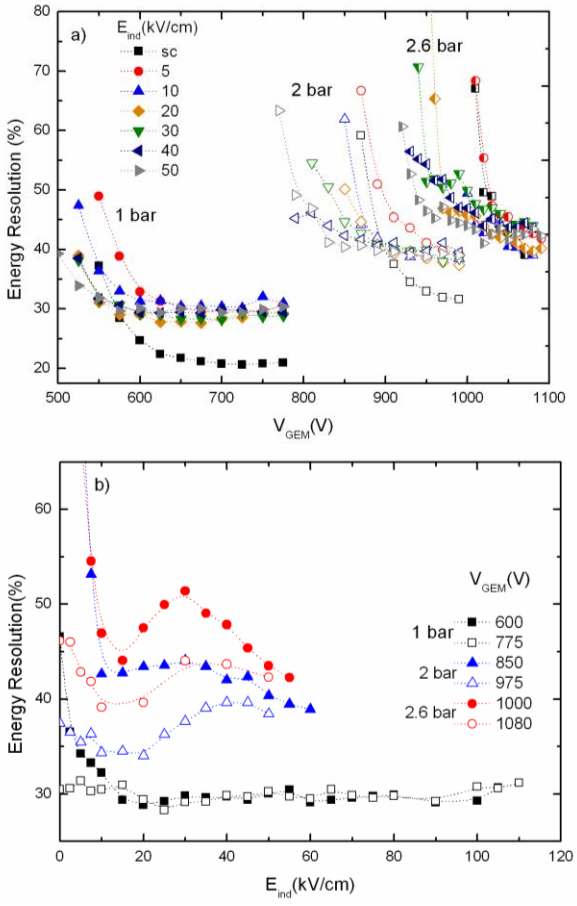

Figure 7. 10 - a) Energy resolution at 1, 2 and 2.6 bar as a function of the GEMd voltage for different induction field values. b) Energy Resolution as a function of the induction field for different GEM voltage and pressures. The E_{drift}=0.5 kV/cm for 1 and 2 bar, 0.3kV/cm for 2.6 bar.

7.3.4 30 μm Induction region Gap

The charge gain performance for the 30 μm induction gap configuration, in pure CF_4, is depicted in Figure 7. 11 a) as function of V_{GEM} for the for several E_{ind} values. The maximum gain measured at 1 bar was about 10^4 (V_{GEM}=800V, sc configuration). The increase on CF_4 pressure to 2 bar leads to a considerable charge gain drop to about 500 (V_{GEM}=950V, sc configuration). For both situations, the sc configuration curve practically match the 30kV/cm induction field curve. The increase of the induction field above 30kV/cm is not traduced in a significant gain augement.

The performance at 2.6 bar is very poor due to the signal/ noise ratio and a leakage current between the bottom-GEM electrode and the grid. Only measurements at 10kV/cm were possible, which correspond to a charge gain of about 200 for a V_{GEM} =1075V.

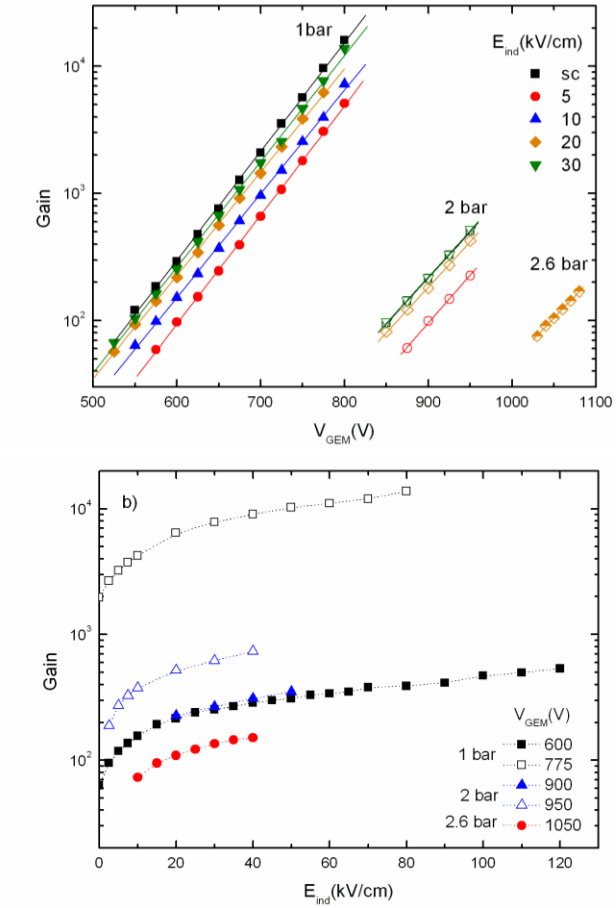

Figure 7. 11 - Gain as a function of: a)V_{GEM} for different induction field values; b) induction field for V_{GEM} values of 700 and 750V. E_{drift}=0.5 kV/cm for 1 and 2 bar and 0.3kV/cm for 2.6 bar.

In Figure 7. 11 b) the charge gain is depicted as a function of the induction field for fixed GEM voltages and pressures. The maximum gain is also in the

order of 10^4 for 1 bar. For 2 and to 2.6 bar the maximum gain values were around 500 e 100, respectively. These values do not present an improvement in spite of the higher induction fields that were reached.

In the 30 μm gap configuration, it was not observed any gain improvement compared to single-GEM mode operation given that the induction field increase is not traduced in a significative gain augment, in opposite to what happens in the sc configuration.

The energy resolution behaviour as a function of V_{GEM} is depicted in Figure 7. 12 a). At 1 and 2 bar the best performance is achieved for the sc configuration, with values around 20% and 30%, respectively. At 2.6 bar the energy resolution is very poor with the best value of the order of 50%. Analysing the energy behaviour, excluding the sc configuration, at 1 bar the energy resolution behaviour obtained for the different induction field curves does not have a significant degradation. At 2 bar the best energy resolution values are between 35 and 40%.

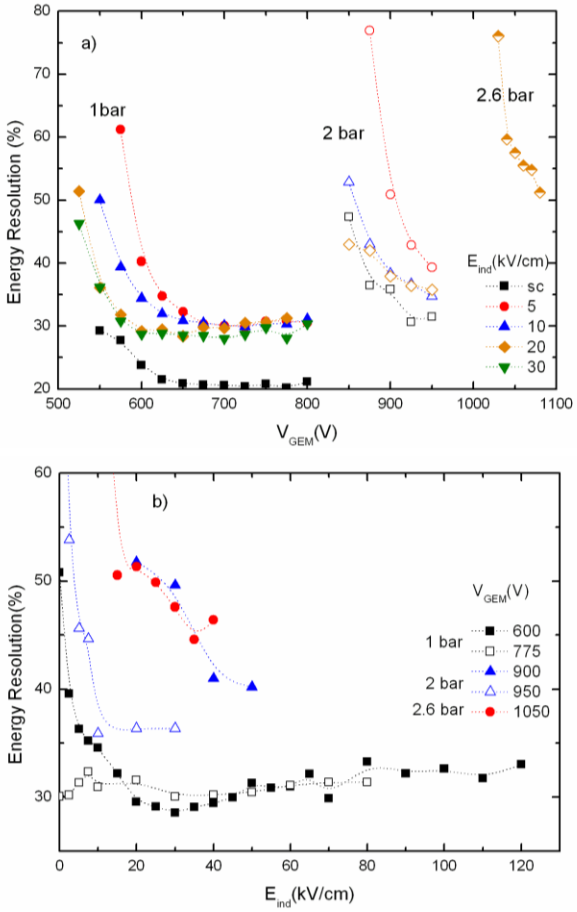

Figure 7. 12 -Energy resolution at 1, 2 and 2.6 bar as a function of the GEM voltage for different induction field values. b)Energy Resolution as a function of E_{ind} for different GEM voltages and pressures. E_{drift}=0.5 kV/cm for 1 and 2 bar and 0.3 kV/cm for 2.6 bar

The energy resolution behaviour as a function of the induction field, depicted in Figure 7. 12 b), is in agreement with the behaviour described above. A good

stability between the results obtained for the 1 bar measurements and a considerable fluctuation for the 2 bar results.

7.3.5 20 μm Induction region Gap

Attending to the poor performance obtained for the 30 μm induction gap, the performance of a 20 μm gap configuration was tested only for 2.6 bar. The charge gain is depicted as a function of V_{GEM} for several E_{ind} values in Figure 7. 13 a). In similarity to what was observed for the 30 μm gap configuration, the increase of E_{ind} is not traduced in a gain improvement compared to the sc configuration. The best value was about 200 measured for sc mode and V_{GEM}=1080V.

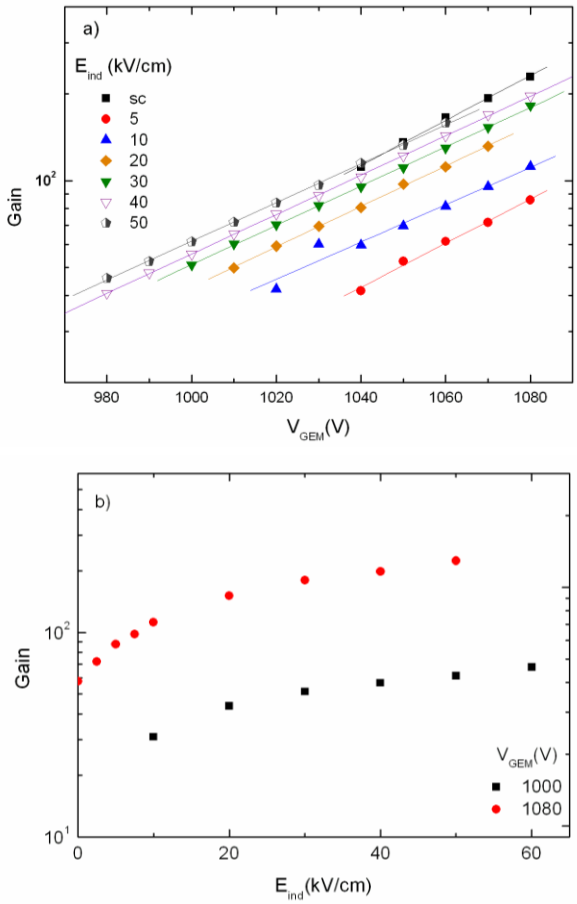

Figure 7. 13- a) Gain as a function of V_{GEM} for different induction field values at 2.6 bar. The sc on the legend means that the bottom GEM and the microgrid were connected. b) Gain as a function of E_{ind} for GEM values of 1000 and 1080V. E_{drift}=0.4k/cm for all measurements.

The charge gain as a function of E_{ind} for fixed GEM voltages is depicted in Figure 7. 13 b). It is shown a slow increase of the charge gain as E_{ind} increases, being the best value of the same order of the one obtained in the previous configuration. This is due to the fact that shallow gaps do not allow a significant

development of the electron avalanche, even for high induction fields, for one electron can produce a reduced number of ionizations in such short distances.

The energy resolution is depicted as a function of GEM voltage in Figure 7. 14 a) and as a function of E_{ind} in Figure 7. 14 b). The best energy resolution obtained was about 35%, the higher GEM voltage of 1080V and an induction field of 30kV/cm.

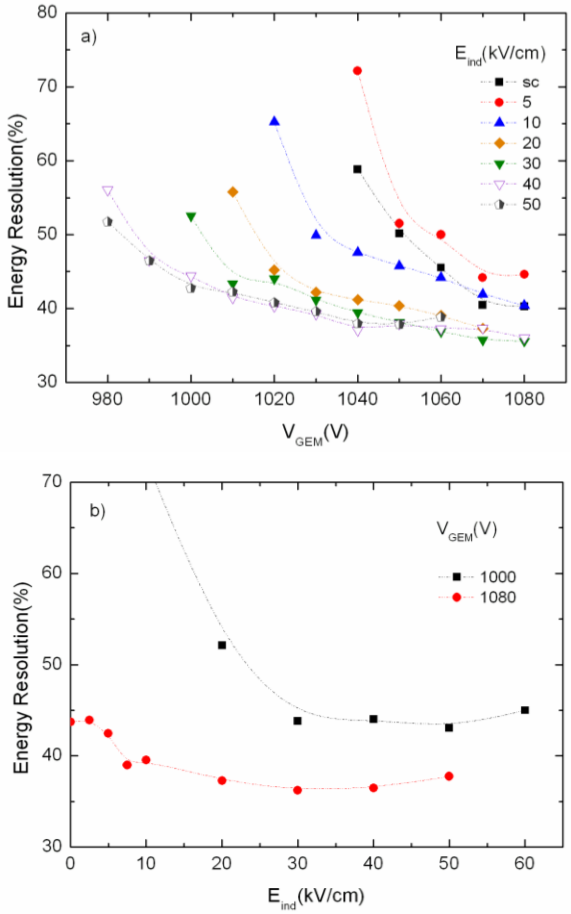

Figure 7. 14- Energy resolution: a) versus V_{GEM} for different induction field values, b) as a function of induction field for GEM values of 1000 and 1080 V

7.3.6 SUMMARY

The influence of the induction region on the GEM-MIGAS performance concerning charge gain and energy resolution was evaluated for gaps in the range of 20 to 250 μm operating in pure CF_4 at pressures of 1, 2 and 2.6 bar. The charge gain behaviour for each CF_4 pressure was compiled for the several induction regions using a fixed GEM voltage at a given pressure.

Figure 7. 15 depicts the charge gain as a function of induction field region for pressures of 1, 2 and 2.6 bar (a, b and c respectively). As seen, for high induction fields the gain increases exponentially with E_{ind} due to electron multiplication in the induction region. For low induction fields, the gain increase with E_{ind} is steeper due to the improvement of the charge collection efficiency by the induction electrode. The results also show that smaller gaps do not have a better gain performance at high pressures. This may be due to the penetration of the very intense electric field present in the GEM holes into the induction gap, which for smaller gaps may extend to the entire region..

Table 7. 2 summaries the maximum gain achieved for each induction region thickness at different operation pressures. At 1 bar of CF_4, the highest gain was about 6×10^4, decreasing one order of magnitude for 2 bar (3×10^3). For 2.6 bar, the maximum charge gain was bellow 10^3. The decrease of the gain with pressure was expected due to intrinsic limits of the GEM, given that increasing the pressure leads to a decrease in the maximum E/p value that can be applied to the induction region.

At 2.6 bar of CF_4 the maximum achieved gain for a gap of 150 μm, only a factor of about 2 higher than that achieved using a 50 μm gap. However, the GEM-MIGAS was unstable for the 150 μm and 250 μm induction gaps owing to higher voltages necessary to create the same field when compared with smaller gaps. Concerning operation stability, and as final goal of this experimental work, it was chosen the 50 μm gap for operation with helium. The objective is to increase the He pressure in the detector, to about 3 bar, which requires an increase of the applied voltage. The 50 μm gap will also make it possible to operate at gains high enough for neutron detection, with lower voltages and consequently better stability.

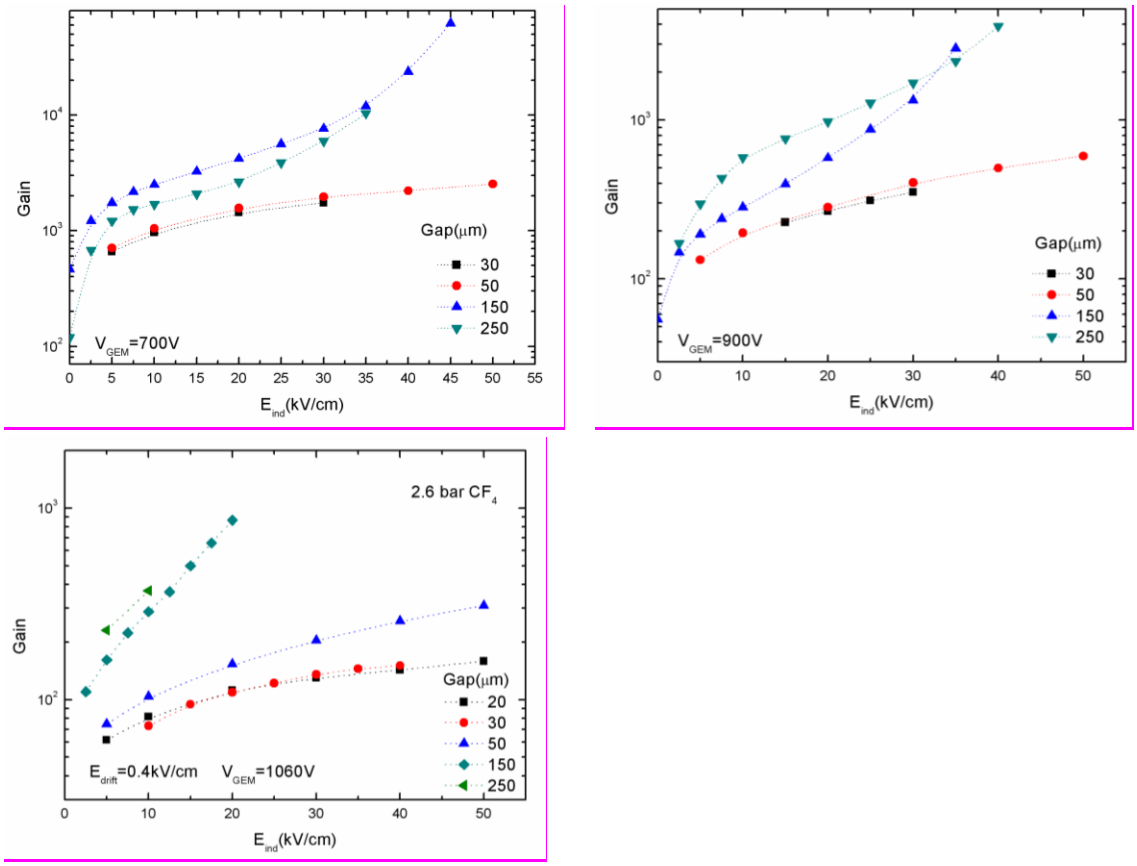

Figure 7. 15 - Gain as a function of induction field for different inductiongaps, obtained at a pressure of 2.6 bar and with E_{drift}=0.4 kV/cm.

Table 7. 2- Maximum gain ahieved with different GEM-MIGAS induction gaps and different pressures.

Gap	1bar	2 bar	2.6 bar
20	-	-	**228** V_{GEM}=1080 V
30	**13864** E_{ind}=30 kV/cm, V_{GEM}=800V	**735** E_{ind}=40 kV/cm, V_{GEM} =950V	**170** E_{ind}=20 kV/cm, V_{GEM} =1080V
50	**23200** E_{ind}=110 kV/cm, V_{GEM} =775V	**2100** E_{ind}=50 kV/cm, V_{GEM} =990V	**430** E_{ind}=50 kV/cm, V_{GEM} =1080V
150	**23700** E_{ind}=40 kV/cm, V_{GEM} =700V	**2830** E_{ind}=35kV/cm, V_{GEM} =900V	**865** E_{ind}=20 kV/cm, V_{GEM} =865V
250	**28636** E_{ind}=35 kV/cm, V_{GEM} =750V	**16663** E_{ind}=25 kV/cm, V_{GEM} =975V	**360** E_{ind}=10 kV/cm, V_{GEM} =1100V

7.4 Influence of the GEM Parameters

The geometric properties of a GEM, such as hole diameter, influence its performance. Studies carried out with different GEM hole diameters, at atmospheric pressure, indicate that there is no advantage in reducing the diameter for values below 60 μm, since low diameters lead to a saturation effect, probably due to the loss of charges by diffusion. Further studies for pressures above the atmospheric demonstrate that the use of small hole GEMs may be an advantage for charge gain improvement since it will be possible to increase the E/p inside the holes, for the same voltage bias..

The influence of the GEM geometry was investigated using different GEM characteristics: hole diameter, thickness and pitch, (see Table 7.1).

7.4.1 GEM 40

The GEM 40 is characterized by a hole diameter on kapton of 40 μm, a pitch of 70 μm and a kapton thickness of 50 μm.

Figure 7. 16 shows the charge gain performance for this GEM geometry. Figure 7. 16 a) depicts the gain as a function of V_{GEM} for different gas pressures. In a first analysis, a lower operational voltage is used compared to the standard GEM. It is practically impossible to differentiate the voltage range for 1 and 2 bar of CF_4. This behaviour was not expected given that the increase of CF_4 pressure is followed by an increase of the GEM voltage. The maximum charge gain obtained at 1 bar is about 10^4 (V_{GEM}=600V, E_{ind}=20kV/cm) decreasing to 10^3 for 2 bar (V_{GEM}=500V, E_{ind}=40kV/cm). The operation of this GEM-MIGAS configuration was not possible at 2.6 bar due to the presence of electrical discharges. The maximum pressure fasible was 2.4 bar. In this case, it is observed an increase of the GEM voltage, as expected, and the decrease of the maximum gain achieved to 600 (E_{ind}=20kV/cm and V_{GEM}=760V).

Figure 7. 16 b) depict the charge gain as a function of the induction field for 1 and 2 bars of CF_4. The charge gain improves with E_{ind} augment and the maximum values are in the order of 10^4.

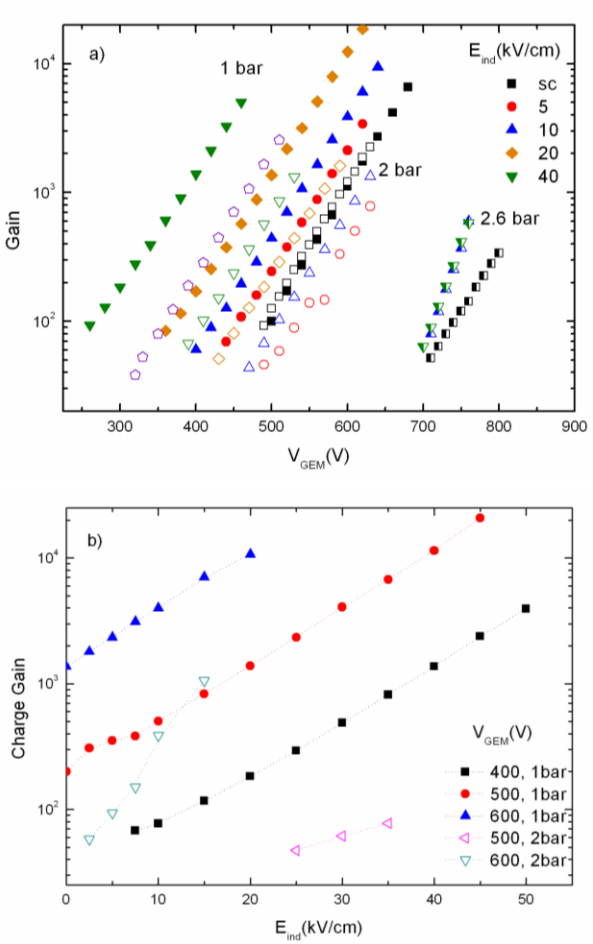

Figure 7. 16 -Gain as a function of : a)V_{GEM} for different induction field values and b) induction field for a V_{GEM} of 700 and 750V. E_{drift}=0.5 k/cm.

The energy resolution is depicted in Figure 7. 17 as a function of the GEM voltage (a) and as a function of the E_{ind} (b). For all CF_4 pressures, the energy resolution improves as the voltage applied to the GEM increases, deteriorating with pressure. The best values were about 25 % at 1 bar, increasing to 30% at 2 bar, and to 35% for the highest pressure of 2.4 bar.

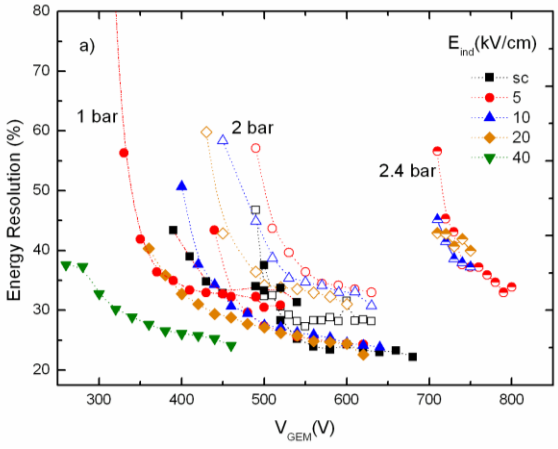

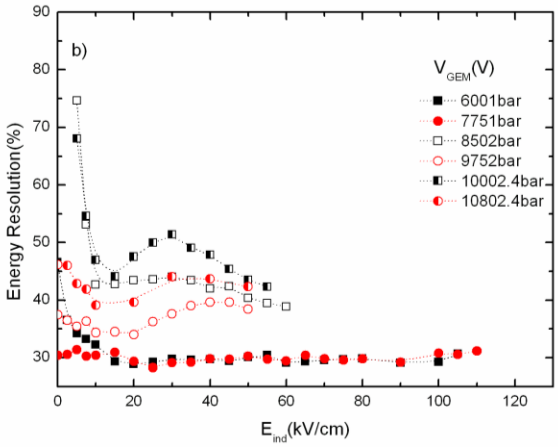

Figure 7. 17 - Energy resolution at 1, 2 and 2.4 bar as a function of the GEM voltge for different induction field values. b)Energy Resolution as a function of the induction field for E_{drift}=0.5 k/cm.

The measurements were performed with two different 40 µm hole diameter GEMs, and both have shown instabilities during the operation, being periodically evident the presence of small discharges even when the voltage applied to the GEM was far from the electric limit. This maybe the cause of the uncommon performance obtained with this GEM configuration, which lead to some instability of the gain and energy resolution measurements. The limitations observed may be related to the quality of this batch of GEMs, the real causes are difficult to evaluate.

7.4.2 GEM 30

The GEM with 30 µm hole diameter has a pitch of 70 µm and kapton thickness of 50 µm. The gain characteristics of GEM 30 geometry are depicted in Figure 7. 18 a), as a function of the GEM voltage, for a different induction fields at 1, 2 and 2.6 bar pressures.

The maximum gain achieved in the GEM-mode was $1x10^4$, $5x10^3$ and $3x10^3$ at 1, 2 and 2.6 bar, respectively. The increase of the induction field is only traduced in a gain augment, compared to the GEM mode operation, for E_{ind} values above 10kV/cm, leading to a three-fold increase in the maximum gain for all the pressures. At 1 and 2 bar, the maximum gain was measured for 50kV/cm on the induction field, reaching values of 3×10^4 and 2×10^4, respectively. For 2.6 bar the highest charge gain was about 7×10^3 for E_{ind}=20kV/cm.

The maximum achieved gain in GEM-MIGAS mode at atmospheric pressure is similar to that obtained with the GEM-MIGAS having a standard 50 µm hole

diameter GEM. However, for 2 and 2.6 bar of CF_4, it is noticeable an improvement of about one order of magnitude.

The gain behaviour as a function of the induction field is depicted in Figure 7. 18 b). For induction field values up to 20 kV/cm, the gain improvement is more significant, being smooth for higher E_{ind} values.

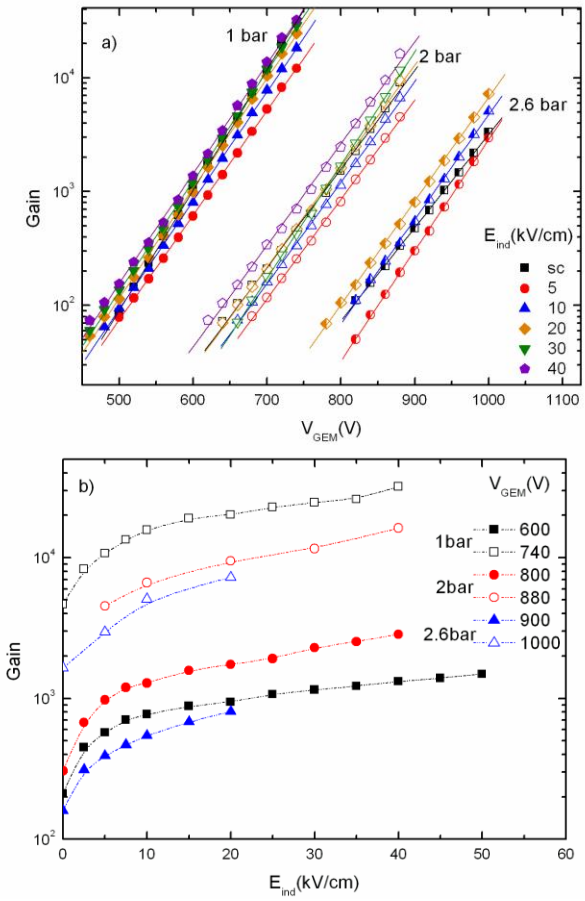

Figure 7. 18- Gain as a function of : a)V_{GEM} for different induction field values; b) induction field for different V_{GEM} values and pressures. The E_{drift}=0.5 k/cm for 1 and 2 bar and 0.4kV/cm for 2.6 bar.

The energy resolution performance was evaluated as a function of the GEM voltage and also as a function of the induction field for the CF_4 pressures of 1, 2 and 2.6 bars as seen in Figure 7. 19 a) and b), respectively. The behaviour is similar to the one observed for the other GEM-MIGAS configurations, improving as the GEM voltage increase and became worst for higher filling pressures. At 1 bar the best energy resolution was between 25 and 30 %, increasing to 30-40 % at 2 bar and to 35-40% at 2.6 bar.

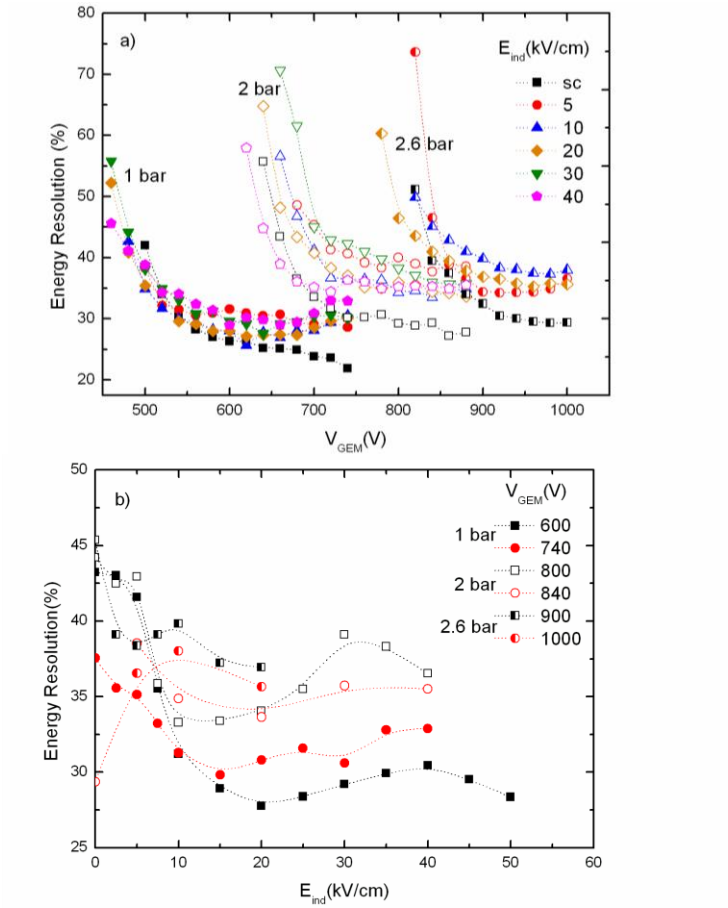

Figure 7. 19 -Energy resolution at 1, 2 and 2.6 bars as a function of the applied voltage on GEM for different induction field values. b) Energy resolution as a function of the induction field. Edrift=0.5 k/cm, for all the pressures.

7.4. 3 SUMMARY

The charge gain performance of GEM-MIGAS was evaluated for GEM hole diameters of 50, 40 and 30 µm. The operation of the 40 µm prototype were followed by several instabilities, for this reason this configuration was not considered for further analysis concerning the influence of GEM hole diameter on charge gain performance.

Figure 7. 20 plots the gain as a function of induction field for a number of different GEM voltages, for 30 µm and 50 µm hole diameter GEMs. The figure shows the benefit of using GEMs with reduced hole diameter for high pressure operation. The gain obtained for the 30 µm hole diameter GEM is one order of magnitude higher than the standard GEM.

The better performance of the 30 µm hole GEM in terms of higher gains at elevated pressure, compared to the 50 µm hole, is attributed to higher electric field strength inside of the GEM channels, which increases as the hole diameter

decreases. As a consequence, the gain increases considerably as the hole diameter is reduced [20]. These results show that reducing the GEM hole diameter is a more efficient way to improve the gain of GEMs in view of their application to neutron detection, instead of selecting standard GEMs that are capable of withstand higher voltages and, thus, reach the needed gains.

The gain improvement working in the GEM-MIGAS mode is limited to a factor of 3-4 (plus another factor of about 3 if an induction gap about 150 μm is used). This way, the main benefit of using a GEM-MIGAS configuration is related to the possibility of using lower GEM voltages, reducing the discharge probability and increasing the life time of the GEM.

Since for neutron detection with He/CF_4 mixtures only gains of a few tens are required, and a CF4 pressure of 2.6 bar is enough to achieve 1 mm position resolution, figures 4 and 5 show the potential of the GEM and/or GEM-MIGAS configuration operating in He/CF_4 mixtures to achieve sub-millimetre position resolution in neutron detection.

As a conclusion, the 30 μm GEM is the one with better performance, especially for high pressure values where the gain does not drop significantly. For this reason, the 30 μm GEM was chosen for the measurements with CF_4/ He mixtures.

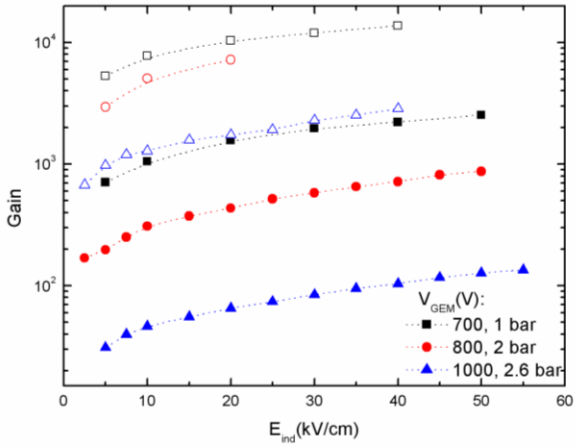

Figure 7. 20 - GEM-MIGAS gain as a function of induction field using type 1 (50 μm) and type 2 (30 mm) GEMs. The filled symbols correspond to the 50μm GEM, while the open symbols are for the 30 μm GEM.

7.5 Measurements with He-CF_4 mixtures

The measurements with a mixture of helium and CF_4 were done for the GEM-MIGAS configuration with 30 μm GEM hole diameter and an induction region of 50 μm, the one with better performance at high pressures. The detector was operated at 2.6 bar of CF_4 mixed with 1 and 2 bar of helium. For He pressures

above 2 bar some electrical instabilities were observed, limiting the detector operation for higher pressures.

The charge gain as a function of GEM voltage for 2.6 bar of CF_4 mixed with He is depicted in Figure 7. 21. The addition of 1 and 2 bar of He to 2.6 bar of CF_4 results in an increase of the GEM voltage of about 100 and 330 V, respectively, to obtain a similar gain. The maximum gain decreases slightly with the addition of He. For pure CF_4, the gain was about 5×10^3, decreasing to 3×10^3 and to 2×10^3 with the addition of 1 and 2 bar of He, respectively.

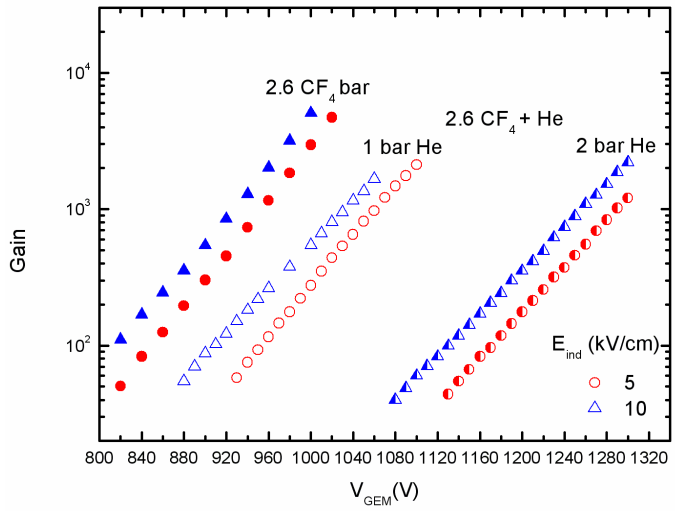

Figure 7. 21 - GEM-MIGAS gain as a function of V_{GEM} for the 30 μm hole diameter GEM. The filled symbols correspond to 2.6 bar of CF_4, the open and half-filled symbols correspond to 2.6 bar of CF_4 added with 1 and 2 bar of He, respectively.

The gain performance is depicted in Figure 7. 22 for GEM-MIGAS operating in 2.6 bar CF_4/1 bar He and 2.6 bar CF_4/2 bar He mixtures, as a function of induction field, for two different V_{GEM} values. As in pure CF_4, the increase of the induction field results in an increase of the maximum gain by a factor of about three.

The augment of He pressure and/or drift region depth is necessary to increase the detection efficiency, which results in a decrease in the achieved gain. However, since the maximum gain at 2 bar of He is almost two orders of magnitude above what is necessary and the decrease in the maximum gain presents a slow decrease with the He pressure, it is expected that a gain high enough can be be achieved as the He pressure increases up to several bar, until the physical limit of the GEM-MIGAS electrical breakdown is achieved.

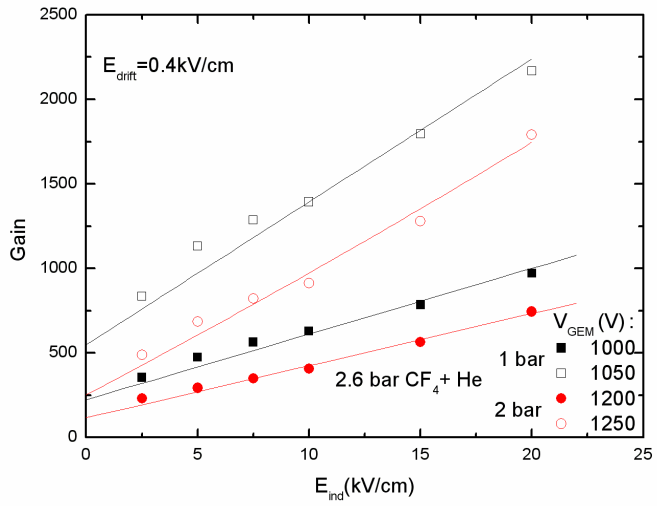

Figure 7. 22- Maximum gain achieved in the GEM-MIGAS as a function of induction field for the 2.6 bar CF_4/1 bar He and 2.6 bar CF_4/2 bar He mixtures and for different V_{GEM} values. The square symbols correspond to 1 bar of He, while the circles are for 2 bar of He

7.6 Conclusions

It was successfully demonstrated that GEM-MIGAS, with 50 µm induction gap and 30 µm hole diameter GEM, is a viable choice to be used in neutron gaseous detectors based in He/CF_4 mixtures. The gain achieved at 2.6 bar CF_4/2 bar He, above 10^3, is large enough for neutron detection, almost two orders of magnitude higher than what is needed.

Higher He filling pressures can be used before the degradation of the gain down to few tens. The investigation of GEMs with different hole diameters shows that the geometrical properties concerning the hole size have a big influence on the gain properties. The electrical field strength increases for narrower holes resulting on gain enhancement. It was also verified that for the 30 µm GEM, the increase on CF_4 pressure is not traduced in a so drastic decrease of gain, in opposite to what happens in the 50 µm GEM, where the increase on pressure leads to an accentuated decrease of gain.

When compared to single-GEM operation, the use of high fields in the induction gap of the GEM-MIGAS may lead to about one order of magnitude increase in gain (e.g. using induction gap thicknesses around 150 µm) and present the possibility of using lower voltages for the GEM biasing, benefitting its operation with reduced discharge probability.

Chapter 8

THICKGEM-MIGAS

The THICKGEM (THGEM) is a gas electron multiplier based on the GEM concept, developed as an amplification of the standard GEM parameters by factors ranging from 5 to 50. Attending to the good performance obtained in some applications, the THGEM will be evaluated as a substitute for the conventional GEM operated with a micromesh readout plane. The investigation concerns the performance of the THGEM coupled to a micromesh readout plane (THGEM-MIGAS) operated in Ar/CH_4 and CF_4, for induction region gaps of 50 and 250 μm.

8.1 Introduction

The investigation of new gas multiplication structures is being done since the introduction of the Microstrip Gas Counter, namely the hole-based multiplication structures. The GEM is the extensively studied hole multiplier. The thick GEM-like (THGEM) structure was developed under the GEM concept [58].

The THGEM is fabricated with Printed Circuit Board (PCB) technology, by a standard drilling and etching process, out of double–clad G-10 plates. The G-10 plates have thickness t of 0.4-3.2 mm and a pitch, a, of 0.7-4 mm. The holes are drilled in the PCB and a chemical etching of copper is made in the rim, with a 0.1 mm distance, around each hole. The chemical etching is essential to reduce considerably the discharges at the hole's rim, resulting in higher applied voltages and higher detector gains. **Erro! A origem da referência não foi encontrada.** shows a microscope photograph of a THGEM with thickness t=0.4 mm, hole diameter d = 0.3 mm, pitch a = 0.7 mm and a rim of 0.1mm.

The THGEM is mechanically an expansion of the standard GEM, with the various dimensions being enlarged by factors ranging from 5 to 50. Although the geometrical dimensions are expanded by large factors, most parameters

concerning its operation, e.g. operation voltage, electric fields, electron diffusion, do not scale accordingly. Therefore, an investigation of the THGEM parameters, as hole diameter, hole spacing and electrode thickness, is required for different applications, at atmospheric and low gas pressures.

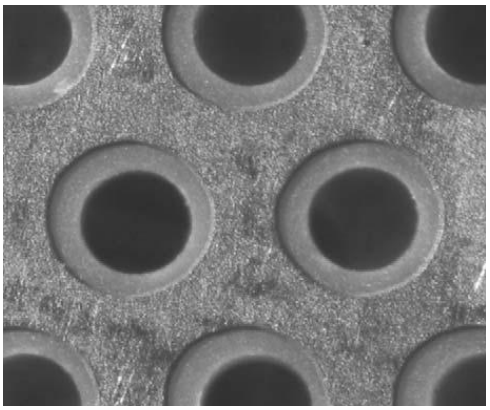

Figure 8. 1- A microscope photograph of a THGEM with thickness t=0.4 mm, hole diameter d = 0.3 mm and pitch a = 0.7 mm. A rim of 0.1mm is etched around the mechanically drilled holes [65].

The THGEM operation principle is similar to the standard GEM, each hole acts as an individual proportional counter. Under the application of a suitable potential across the THGEM a strong field develops within the holes. The electrons released by ionizing radiation in the region above the THGEM drift to the holes due to a drift electrical field action, being multiplied within the holes under high electric field, in the range 25-50 kV/cm. The majority of the electrons generated in the avalanches are transferred to a charge collection electrode or to another amplifying device. Some percent of them are collected by the THGEM bottom electrode, depending on the size and direction of the transfer an induction field.

The avalanche confinement within the holes has the advantage of reducing photon-mediated secondary effects, leading to high-gain operation in a large variety of gases.

Several studies have been performed with THGEM, measuring essential parameters such as effective gain, counting rate response, ion back flow, X-ray energy resolution. In addition, simulations with Maxwell and Garfield have been performed in order to evaluate the suitable electrode geometries and understand the processes involved in the THGEM operation.

A resume study [65], demonstrates that THGEM is an attractive robust and economic electron multiplier, suitable for applications at atmospheric gas pressure. The gain measured was about 10^4 to 10^5 in a single multiplier increasing to 10 - 100 times in a double configuration. The pulse rise-time is in the order of a few ns and the counting rate capability is up to 10 MHz/mm^2 at a gain of 10^4.

The 5.9 keV X-ray energy resolution is about 20%. The IBF is typically below 10%, quite similar to that obtained with a 3-GEM cascade, under similar conditions.

The study indicates that in terms of operation mechanisms and electric field role, the THGEM is quite similar to the standard GEM. The maximum voltage applied across the holes before the onset of sparks does not scale with dimensions, so the field inside the holes is smaller than in GEM. However, due to the larger dimensions, in particular the thickeness, higher gains are obtained. The bigger hole size, larger than the electron diffusion, contributes to a more efficient electron focusing into the holes. Changing the thickness and the hole size the THGEM can be optimized for different operation conditions, for example the operation at very low gas pressures, of the order of mbar.

Attending to the THGEM performance it is important to study the viability of the MIGAS concept with a THGEM instead of a GEM. This evaluation was done only for a few situations. The viability of the THGEM-MIGAS device was investigated using induction region thicknesses of 50 and 250 μm in Ar/CH_4(95/5) and in CF_4 at atmospheric pressure.

8.2 Experimental Setup

The THGEM-MIGAS was mounted inside the stainless-steel cylindrical chamber used in the previous study. The chamber was pumped down to 10^{-6} mbar before filling with CF4 or Ar/CH4 mixture. Gas circulation was maintained by convection through SAES St707 getters, operated at 110ºC. The detector was irradiated with an X-ray beam (from a ^{55}Fe source) collimated to 1 mm in diameter. Figure 8. 1 depicts the schematic diagram of THGEM-MIGAS.

The THGEM-MIGAS electron multiplier has an active area of 10×10 mm2. The THGEM is made of a G-10 plate with a thickness of 0.4 mm, drilled with a hexagonal pattern of holes with a diameter of 0.3 mm and a pitch of 0.7 mm. The copper was etched 0.1 mm around the holes. The readout electrodes are the same described in the previous chapter.

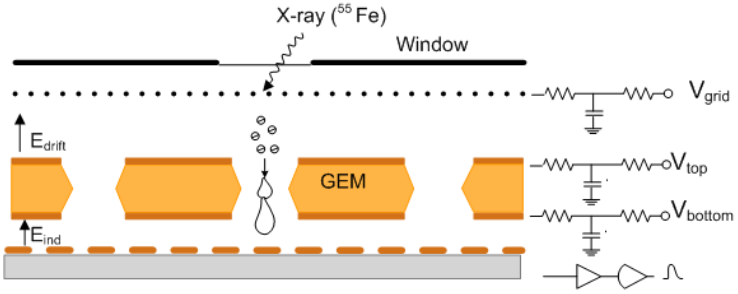

Figure 8. 2- Schematic diagram of THGEM-MIGAS.

The drift region, between the top THGEM electrode and the drift grid, was kept at 5 mm. The drift and THGEM electrodes were individually biased by HV power supplies with the current limited to 50 nA, and operated with negative voltages, while the micromesh of the induction plane was set to ground.

The electronic system associated to this THGEM-MIGAS detector is the same used in the previous studies for GEM-MIGAS.

8.3 Results

The THGEM-MIGAS performance was evaluated at atmospheric pressure operation in Ar/CH4 and pure CF_4, for induction field gaps of 50 and 250 µm. The results include the charge gain behaviour as a function of the THGEM voltage and of the induction field. The THGEM voltage range was also investigated in order to compare with the standard GEM.

8.3.1 50 µm Induction region Gap

The gain results obtained for pure CF_4 for an induction region gap of 50 µm are depicted in Figure 8. 3, as a function of THGEM voltage in (a) and induction field in b).

The charge gain as a function of THGEM voltage follows an exponential behaviour, achieving the maximum value, about 3×10^3, for the highest induction field of 40 kV/cm and for a THGEM voltage of 2760 V. The charge gain as a function of induction field shows an improvement as E_{ind} augments. A gain of about 6×10^3 was obtained for a E_{ind}=45kV/cm and $V_{TH\text{-}GEM}$=2700V.

Comparing with the gain obtained for GEM-MIGAS, 10^4 for V_{GEM}=775Vand E_{ind}=50kV/cm, the difference is residual. The main difference is related with the increase of THGEM voltage compared to the standard GEM.

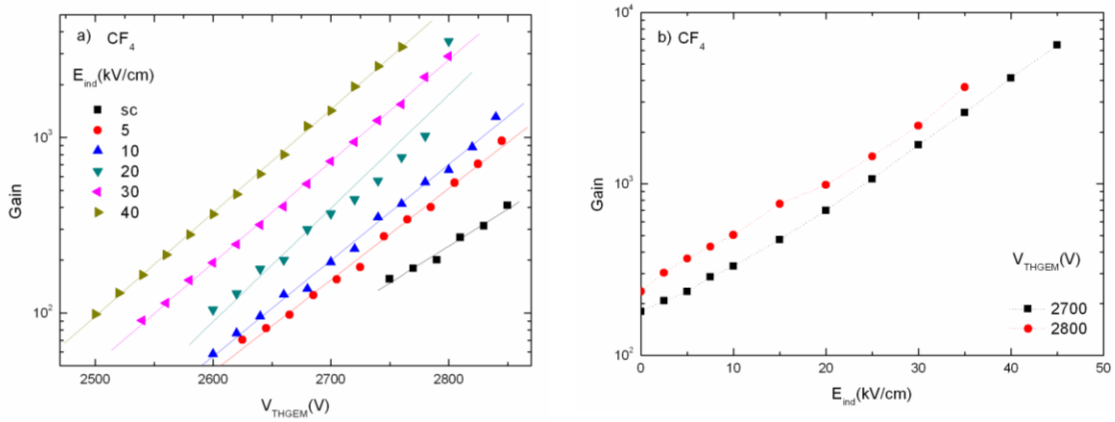

Figure 8. 3- a) Gain as a function of V_{GEM} for different induction field values. b) Gain as a function of E_{ind} for THGEM voltages of 2700 and 2800V . E_{drift} was kept at 0.5k/cm.

The Ar/CH_4 measurements are depicted in Figure 8. 4, where the charge gain is represented as a function of V_{THGEM}, a), and as a function of the E_{ind}, b).

The charge gain increases exponentially with V_{THGEM}, reaching the maximum value of about 3×10^3 for E_{ind}=40 kV/cm and a THGEM voltage of 1125 V. The gain improvement due to the induction field increase is very clear in **Erro! A origem da referência não foi encontrada.** b).

The best charge gain measured for the GEM-MIGAS was about 10^4 for V_{GEM}= 425V and E_{ind}=50kV/cm, which is better than the value obtained for the THGEM configuration. The increase of the THGEM voltage was not as significant as that verified in the CF_4 measurements.

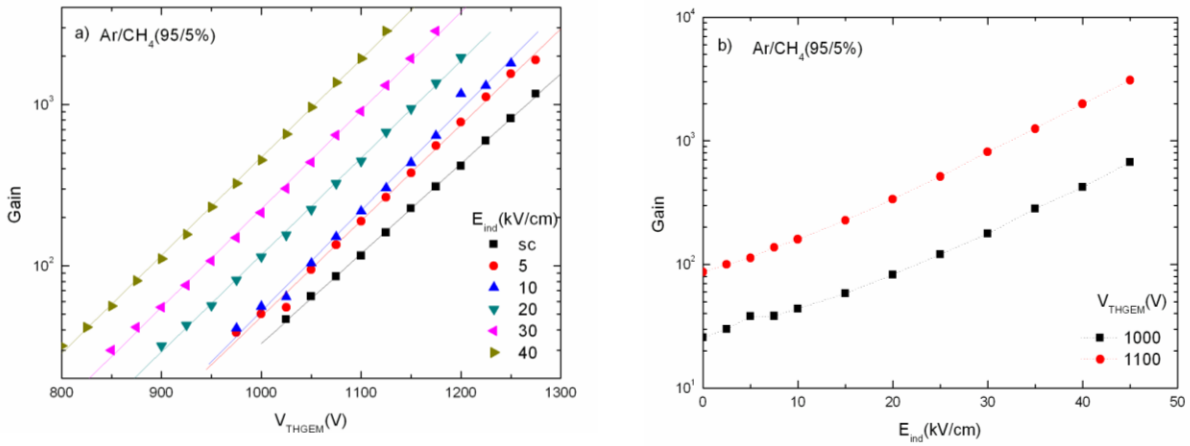

Figure 8. 4- Gain as a function of: a) V_{THGEM} for different induction field values; b) E_{ind} for THGEM values of 1000 and 1100V. E_{drift} was kept at 0.5k/cm.

8.3.2 250 µm Induction region Gap

Using 250 µm as induction region gap the operation of THGEM-MIGAS was not possible in CF_4. Attending to the high voltage required, several discharges developed across the drift electrode, being impossible to apply the voltages required for multiplication.

The measurements made with the Ar/CH_4 mixture are depicted in Figure 8. 5. The charge gain as a function of THGEM voltage, Figure 8. 5a), shows significant differences concerning the THGEM voltage range for each E_{ind} curve, relative to the behaviour observed for the 50 µm configuration where the THGEM voltage range was practically the same for each induction field value. The maximum gain was about 2×10^3, which means that there is no improvement on gain as the induction region gap increases. Compared to GEM-MIGAS, where gains above 10^4 are obtained, the 250 µm gap operation shows no improvement, relative to the GEM-MIGAS configuration.

The gain behaviour as a function of induction field Figure 8. 5b) shows a large increase of gain with E_{ind} which is different from the standard configuration, where the gain improvement due to the induction field has a smooth variation.

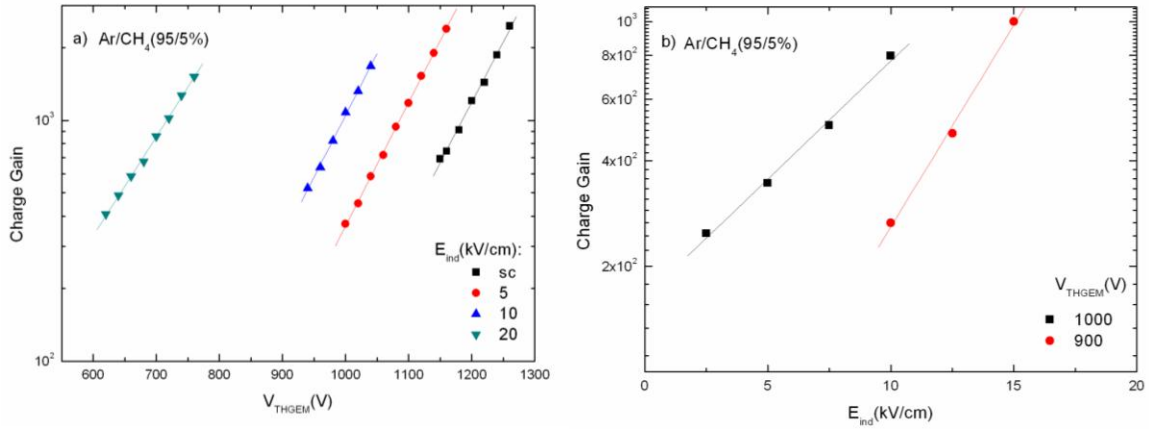

Figure 8. 5- Gain as a function of: a) V_{THGEM} for different induction field values; b) E_{ind} for THGEM values of 1000 and 900V. E_{drift}=0.5k/cm for all measurements.

8.4 Conclusions

The first approach on THGEM-MIGAS studies does not show improvement in terms of charge gain. This can be explained by the extension of the avalanche to the induction gap, since the avalanche is supposed to be larger there is no space for further multiplications. Any improvement compared to the single THGEM operation is due to the improvement on charge efficiency collection. The use of small induction region gaps does not bring any improvement for the THGEM performance. Maybe the use of larger induction gaps, larger than the avalanche penetration shows some benefits.

The high voltage needed for the THGEM-MIGAS compared to the conventional GEM-MIGAS can compromise potential applications on gas detectors.

In a first approach, the THGEM-MIGAS was not characterized for best performance, compared to the standard GEM-MIGAS. Further studies are needed to investigate its performance with more detail

Chapter 9.

Conclusions

The purpose of this work is the development and study of a new electron multiplier, the GEM-MIGAS. This multiplier was developed under the concept a standard GEM assembled with a Micromegas induction region.

Initially, the GEM-MIGAS was introduced combined with an induction region of 50 μm thickness. The operation performance of this configuration, in terms of charge gain and energy resolution, was evaluated in typical gases, Ar and CH_4 as well as for the standard gas mixtures of Ar-CH_4 (90/10%). The highest charge gain of about 10^4 was achieved for Ar, with a slight decrease to 5×10^3 for P10 and 3×10^3 for CH_4. The values obtained for Ar and CH_4 correspond to an improvement compared to single-GEM and Micromegas configurations. The P10 gas mixture has a better performance for GEM-MIGAS than the single-GEM configuration, however worse than Micromegas. The best energy resolutions obtained are about 35% for Ar and 20–22% for CH_4 and P10.

The good performance obtained with the first prototype motivated further developments of the structure by increasing the induction region gap from 50 up to 300μm, expecting that larger induction gap thicknesses may sustain larger voltage differences and consequently lead to higher effective gains. The GEM-MIGAS performance concerning the single electron response, the ion back-flow reduction and the viability for neutron detection were evaluated for the extended gap model.

A GEM-MIGAS prototype was successfully operated in the parallel-plate mode using the He/iso-C4H10 (85/15%) gas mixture at atmospheric pressure to measure the charge gain characteristics with the induction gap set to 50, 100, 150, 200, 250 and 300 μm. The highest charge gains, about 10^6, occurred for induction regions in the range of 150 to 300 μm.

The ion back-flow reduction and charge gain measurements in Ar/CH_4 (95/5%), successfully demonstrated that increasing the induction gap of the

GEM-MIGAS multiplier from 50 μm to 300 μm leads to higher gains, reaching values above 10^5. The IBF is reduced by a factor of 5, being the minimum values achieved for the 300 μm gap, about 4% for E_{drift}=0.5 kV/cm and about 2% for Edrift=0.1kV/cm. The IBF obtained is similar to that obtained in triple-GEM configurations and in Micromegas, but much higher than those obtained in a flipped-MHSP/GEM/MHSP electron multiplier cascade (IBF ~ 0.02% at gains of 10^4 and Edrift=0.2 kV/cm). This amount of IBF is sufficient to operate CSI photocathode with this electron multiplier. The advantage of the GEM-MIGAS is the simplicity compared to other cascade configurations.

The GEM-MIGAS viability for neutron gaseous detectors based in He/CF_4 mixtures was evaluated in terms of the induction region gap and the GEM hole diameter, being demonstrated that the 50 μm induction gap and the 30 μm hole GEM configuration is a viable choice. The gain achieved in 2.6 bar CF_4/2 bar He, above 10^3, is large enough for neutron detection, above 2x103, almost two orders of magnitude higher than what is needed.

In conclusion, in most experimental studies the GEM-MIGAS exhibits a better performance compared to the single-GEM and Micromegas. The GEM-MIGAS structure successfully demonstrated its viability for typical applications of gas detector, with confirmed results and with advantages on its simple structure and easy assembling.

Future work will extend the GEM-MIGAS concept to the THGEM. Preliminary work, performed under this thesis, have demonstrated that the induction region should be thicker than 250um to take full advantage of the induction field to further increase the multiplier gain.

9. References

[1] Salvat, F. *et al*, "*PENELOPE* – A Code System for Monte Carlo Simulation of Electron and Photon Transport".

[2] Knoll G.F., "Radiation Detection and Measurement", John Wiley Sons, Third Edition, Michigan U.S.A., 2000.

[3] Charpak G., Rahm D., Steiner H., "Some developments in the operation of multiwire proportional chambers" ,Nuclear Instruments and Methods A80 (13), 1970.

[4] A. Oed, "Position-Sensitive detector with Microstrip Anode for electron Multiplication with gases", Nuclear Instruments and Methods in Physics Research A263 (351)1988.

[5] Meinschad, T. K., "GEM- A Novel Gaseous Particle Detector", CERN- Thesis - 2005-037.

[6] Oed A., "Micro pattern structures for a gas detectors", Nuclear Instruments and Methods in Physics Research A 471 (109) 2001.

[7] Fabio Sauli., "Micro pattern gas detectors", Nuclear Instruments and Methods in Physics Research A 477 (1) 2002.

[8] Giomataris Y., Rebourgeard Ph. , Robert J.P., Charpak G., "Micromegas: a high-granularity position-sensitive gaseous detector for high particle-flux environments", Nuclear Instruments and Methods in Physics Research A 376 (29) 1996.

[9] Giomataris Y., "Development and prospects of the new gaseous detector "Micromegas", Nuclear Instruments and Methods in Physics Research A 419 (239) 1998.

[10] Charpak G., Derré J., Giomataris Y., Rebourgeard Ph., "Micromegas, a multipurpose gaseous detector", Nuclear Instruments and Methods in Physics Research A 478(26) 2002.

[11] Sauli F., "GEM: A new concept for electron amplification in gas detectors", Nuclear Instruments and Methods in Physics Research A 386(531) 1997.

[12] Tsoulfanidis N., "Measurements and Detection of Radiation", Taylor&Francis, Second Edition, Washington, U.S.A.,1995.

[13] Sauli F., "Principles of Operation of Multiwire Proportional and Drift Chambers", CERN 77-09, Geneva 1977.

[14] Meinschad, T.K., "GEM- A Novel Gaseous Particle Detector ", Ph dissertation, CERN-Thesis-2005-037, Geneva 2005.

[15] Francis G., "Ionazation Phenomena in Gases", Butterworths Scientific Publications, London , 1960.

[16] Kleinknecht, K., " Detectors for particle radiation", second edition, Cambridge : University Press, 1998 .

[17] Gas Detectors Development-CERN. http://gdd.web.cern.ch/GDD/.

[18] Benlloch J., **A.** Bressan, ***C.*** Biittne, M. Capeh, M. Gruw C, M. Hoch, J.C. Labbe, **A.** Placci, L. Ropelewski, F. Sauli, **A.** Sharma and R. Veenhof , "Development of the Gas Electron Multiplier (GEM)", IEEE Transactions on Nuclear Scince, Volume 45, Nº 3, June 1998.

[19] Sauli F., "Progress with the gas electron multiplier", Nuclear Instruments and Methods in Physics Research A 522(93-98) 2004.

[20] Bouclier R., et all, "The Gas Electron Multiplier (GEM)", IEEE Transactions on Nuclear Scince, Volume 44, Nº 3, June 1997.

[21] Bachmann S., "Charge amplification and transfer processes in the gas electron multiplier", Nuclear Instruments and Methods in Physics Research A 439(376-408) 1999.

[22] Killenberg M. S., "Modelling and measurement of charge transfer in multiple GEM structures", Nuclear Instruments and Methods in Physics Research A 498(369-383) 2003.

[23] Bachmann S. et all, "High rate X-ray imaging using multi-GEM detectors with a novel readout design", Nuclear Instruments and Methods in Physics Research A 478 (2002) 104-108.

[24] MAXWELL, Commercial Finite Element Computation Package, Ansoft Co. Pittsburg,PA, USA

[25] J.A. Mir, R. Stephenson, N.J. Rhodes, E.M. Schooneveld , J. F. C. A. Veloso, J. M. F. dos Santos , "Short Induction gap Gas Electron Multiplier (GEM) for X-ray Spectroscopy", *Nucl. Instrum. Methods Phys. Res.* A, vol. 573, pp. 179-182, 2007.

[26] J.A. Mir, R. Stephenson, N.J. Rhodes, E.M. Schooneveld, H. Natal da Luz, J. F. C. A. Veloso, J. M. F. dos Santos, C.D.R. Azevedo , "Further studies on the gain properties of a Gas Electron Multiplier with Micro-Induction Gap Amplifying Structure (GEM-MIGAS) aimed at low energy X-ray detection", *Nucl. Instrum. Methods Phys. Res.* A, vol. 580, pp. 1372-1377, 2007.

[27] J.A. Mir, J.M. Maia, A.S. Conceição, R. Stephenson, J.D. Lipp, N.J. Rhodes, E.M. Schooneveld, H. Natal da Luz, J. F. C. A. Veloso, J. M. F. dos Santos, "Single-Electron Response Using a GEM-MIGAS Electron Multiplier", *IEEE Trans. Nucl. Sci.*, vol. 55, no.4, pp. 2334-2240, 2008.

[28] A. Breskin, R. Alon, M. Cortesi, R. Chechik, J. Miyamoto, V. Dangendorf, J.M. Maia, J.M.F. Dos Santos," A concise review on THGEM detectors" *Nucl. Instrum. Methods Phys. Res.* A, vol. 598, pp. 107-111, 2009.

[29] A. Bondar, A. Buzulutskov,L. Shekhtman, "High pressure operation of the triple-GEM detector in pure Ne, Ar and Xe", *Nucl. Instrum. Methods Phys. Res.* A, vol. 481, pp. 200-203, 2002.

[30] S.X. Oda, H. Hamagaki, K. Ozawa, M. Inuzuka, T. Sakaguchi, T. Isobe, T. Gunji, Y. Morino, S. Saito, Y.L. Yamaguchi, S. Sawada and S. Yokkaichi, "De-

velopment of a time Projection Chamber using gas electron multipliers (GEM-TPC)", *Nucl. Instrum. Methods Phys. Res.* A, vol. 566, pp. 312-320, 2006.

[31] L. Ounalli, J-M. Vuilleumier, D. Schenker, J-L. Vuilleumie, "Micromegas-TPC development for a rare event detection", 3rd Symposium on Large YPCs for Lower Energy Rare Event Detection, *Journal of Physics: Conference Series*, vol. 65-012017, 2007.

[32] A. Bressan, A. Buzulutskov, L. Ropelewski, F. Sauli, L. Shekhtman, "High Gain operation of GEM in pure argon", *Nucl. Instrum. Methods Phys. Res.* A, vol. 423, pp. 119-124, 1999.

[33] A. Bondar, A. Buzulutskov, F. Sauli and L. Shekhtman," High- and low-pressure operation of the gas electron multiplier" *Nucl. Instrum. Methods Phys. Res.* A, vol. 419, pp. 418-422, 1998.

[34] S. Kane, J. May, J. Miyamoto, I. Shipsey, "A Study of Micromegas with Pre amplification with a single GEM", *Proceedings of the 7th International Conference on Advanced Technology & Particle Physics*, World Scientific , pp. 694-703, 2001.

[35] J.A. Mir, N.J. Rhodes, E.M. Schooneveld, A.S. Conceição, J.M. Maia, J.F.C.A. Veloso, J.M.F. dos Santos, " Evaluation of the optimum induction gap for the GEM-MIGAS", *Nucl. Instrum. Methods Phys. Res.* A , vol.600, pp.640-643,2009.

[36] V.M. Blanco Carballo, C. Salm, S.M. Smits, J. Schmitz, M. Chefdeville, H. van der Graaf, J. Timmermans and J.L. Visschers, " On the geometrical design of integrated Micromegas detectors *Nucl. Instrum. Methods Phys. Res.* A , vol. 576, pp 1-4,2007.

[37] L. Ounalli, J-M Vuilleumier, D. Schenker, J-L Vuilleumier," Micromegas-TPC development for rare event detection", J. of Phys.: Conference Series 65, 012017, 2007.

[38] J.A. Mir, A.S. Conceição, H.Y. Al-Shejni, J.F.C.A. Veloso, J.M.F. dos, "GEM-MIGAS: Charge gain characteristics for the induction gap in the 50-300 microns range", accepted for publication to NIM A.

[39] P. Colas, I. Giomataris, V. Lepeltier, "Ion back flow in the micromegas TPC for the future linear collider", *Nucl. Instrum. Methods Phys. Res.* A , vol.535, pp. 226-230,2004.

[40] D. Mörmann, A. Breskin, R. Chechik, D. Bloch, A. Vasiljev," Evaluation and reduction of ion back-flow in multi-GEM detectors", *Nucl. Instrum. Methods Phys. Res.* A , vol.516, pp. 315-326,2004.

[41] J.M. Maia, D. Mörmann, A. Breskin, R. Chechik, , J.F.C.A. Veloso and J.M.F. dos Santos, "Avalanche-ion back-flow reduction in gaseous electron multipliers based on GEM/MHSP", *Nucl. Instrum. Methods Phys. Res.* A , vol.523, pp. 321-334-,2004.

[42] J. M. Maia, D. Mörmann, A. Breskin, R. Chechik, J. F. C. A. Veloso, J. M. F. dos Santos, "Progress in MHSP electron multiplier operation", *IEEE Trans. Nucl. Sci.*, vol.51, no 4, pp. 1503-1508, 2004.

[43] A. Breskin, D. Mörmann, A. Lyashenko, R. Chechik, F.D. Amaro, J.M. Maia, J.F.C.A. Veloso and J.M.F. dos Santos," Ion-induced effects in GEM and GEM/MHSP gaseous photomultipliers for the UV and the visible spectral range" ", *Nucl. Instrum. Methods Phys. Res.* A , vol.553, pp. 46-52, 2005.

[44] A. Buzulutskov, A. Breskin, R. Chechik, G. Garty, F. Sauli and L. Shekhtman, "The GEM photomultiplier operated with noble gas mixtures," *Nucl. Instrum. Methods Phys. Res.* A , vol.443, pp 164-180,2000.

[45] T. Meinschad, L. Ropelewski and F. Sauli, "GEM-based photon detector for RICH applications," *Nucl. Instrum. Methods Phys. Res.* A , vol.535, pp.324-329, 2004.

[46] D.R. Nygren and J.N. Marx, "The Time Projection Chamber", Physics Today 31 (1978) 46.

[47] P. Némethy, P. J Oddone, N. Toge and A. Ishibashi, " Gated time projection chamber", *Nucl. Instrum. Methods Phys. Res.* A , vol.212, pp.273-280,1983.

[48] A. Breskin, A. Buzulutskov, R. Chechik, B.K. Singh, A. Bondar, L.Shekhtman, "Sealed GEM photomultipliers with a CsI photocathode: ion feedback and ageing" ", *Nucl. Instrum. Methods Phys. Res.* A , vol.478, pp. 225-229,2002.

[49] A. Bondar, A. Buzulutskov, ,L. Shekhtman, A. Vasiljev," Study of ion feedback in multi-GEM structures", *Nucl. Instrum. Meth.* A 496 (2003) 325.

[50] F. Sauli, S. Kappler, L. Ropelewski,"Electron collection and ion-feedback in GEMbased detectors", IEEE Trans. *Nucl. Sci* 50 (2003) 803.

[51] A. V. Lyashenko, A. Breskin, R. Chechik, J.F.C.A. Veloso and J.M.F. dos Santos, F.D. Amaro, "Advances in ion back-flow reduction in cascaded gaseous multipliers incorporating R-MHSP elements", *JINST,10004*, (2006).

[52] J.F. Clergeau, P.Convert,D. Feltin,H. E. Fisher,B.Guérard, T. Hansen, G. Manzin, A. Oed, P. Palleau, "Operation of Sealed Microstrip Gas Chambers at the ILL", *IEEE Trans. Nucl. Sci.*, vol. 48, no.4, pp. 1075-1080, 2001

[53] J.F.C.A. Veloso , F. Amaro,J.M.F. dos Santos, J. A. Mir, G.E. Derbyshire, R. Stephenson, N. J. Rhodes, E.M. Schooneveld, "Application of the Microhole and Strip Plate Detector for Neutron Detection" *IEEE Trans. Nucl. Sci.*, vol. 51, no.5, pp. 2104-2109, 2004.

[54] T. L. van Vuure,C.W.E. van Eijk, F. Fraga, R. W. Hollander,L. Margato, "High-Pressure GEM Operation Aiming at Thermal Neutron Detection" *IEEE Trans. Nucl. Sci.*, vol. 48, no.4, pp. 1092-1094, 2001

[55] F.A.F. Fraga, L.M.S. Margato, S.T.G. Fetal, M.M. F.R. Fraga, R. Ferreira Marques, A.J.P.L. Policarpo, B. Guerard, A. Oed, G. Manzini, T. van Vuure, "CCD readout of GEM-based neutron detectores" , *Nucl. Instrum. Methods Phys. Res.* A, vol. 478, pp. 357-361, 2002.

[56] C. W.E. van Eijk,"Neutron PSDs for the next generation of spallation neutron sources", *Nucl. Instrum. Methods Phys. Res.* A, vol. 477, pp. 383-390, 2002.

[57] H. Natal da Luz, A. S. Conceição, J. F.C.A. Veloso, J. M.F. dos Santos, A.C.S.S.M. Bento, J. A. Mir, L. F. Requicha Ferreira, " Gem operation in CF4: studies of charge and scintillation properties",

[58] R. Chechik, A. Breskin, C. ShalemD. Mormann,"Thick GEM-like hole multipliers: properties and possible applications" ", *Nucl. Instrum. Methods Phys. Res.* A , vol.535, pp. 303-308,2004.

[59] Conceição A.S., "Estudo da Cintilação em GEM's a operar em Xénon", Master Thesis in Instrumentation and Microelectronic, Coimbra University, 2007.

[60] S. Kane, J. May, J. Miyamoto and I. Shipsey, "An aging study of a MICROMEGAS with GEM preamplification", *Nucl. Instrum. Methods Phys. Res.* A, vol.515, pp 261-265, 2003.

[61] J. Benlloch, A. Bressan, M. Capeáns, M. Gruwé, M. Hoch, J.C. Labbé, Placci, L. Ropelewski, F. Saul, "Further developments and beam tests of the gas electron multiplier (GEM)", *Nucl. Instrum. Methods Phys. Res.* A, vol.419, pp. 410-417, 1998.

[62] J.A. Mir, D. Sole, J.D. Lipp, R. Stephenson, J.A. Purton, S.L.P.Savin, A.V.Chadwick, L.O'Dell "Low X-Ray Energy Fluorescence Gas Electron Multiplier (GEM) for XAS Studies", *IEEE Trans. Nucl. Sci.*, vol.54, no6,pp.2637-2641,2007.

[63] A.S. Conceição, J.M. Maia J.A. Mir, L.M.P. Fernandes, J. M. F. dos Santos, "GEM-MIGAS electron multiplier operation in Argon-Methane mixtures", *IEEE Trans. Nucl. Sci.*, vol. 56, no5, pp. 2874-2879, 2009.

[64] S. Roth, "Charge transfer of GEM structures in high magnetic fields", *Nucl. Instrum. Methods Phys. Res.* A, vol.535, pp. 330-333,2004.

[65] C. Shalem, R. Chechik, A. Breskin, K. Micaeli, "Advances in Thick GEM-like gaseous electron multipliers-Part I: atmospheric pressure operation", *Nucl. Instrum. Methods Phys. Res.* A, vol.558, pp. 475-489, 2006.

[66] S. Bachmann, A. Bressan, S. Kappler, B. Ketzer, M. Deutel, L. Ropelewski, F. Sauli, E. Schulte, "Development and applications of the gas electron multiplier", *Nucl. Instrum. Methods Phys. Res.* A, vol.471, pp. 115-119, 2001.

[67] I. Giomataris, R. De Oliveira, S. Andriamonje, S. Aúne, G. Charpak, P. Colas, G. Fanourakis, E. Ferrer, A. Giganon, Ph. Rebourgeard, P. Salin, "Micromegas in a bulk", *Nucl. Instrum. Methods Phys. Res.* A, vol.560, pp. 405-408, 2006.

[68] COMPASS experiment, http://wwwcompass.cern.ch/, February 2011.

[69] H. Raether, Electron Avalanches and Breakdown in Gases, Butterworth, London, 1964.

[70] S. Bachmann, A. Bressan, B. Ketzer, M. Deutel, L. Ropelewski, F. Sauli, A. Bondar, A. Buzulutskov, L. Shekhtman, A. Sokolov, A. Tatarinov, A. Vasil'ev, S. Kappler, E. Schult," Performance of GEM detectors in high intensity particle beams", *Nucl. Instrum. Methods Phys. Res.* A, vol.470, pp. 548-561, 2001.

[71] S. Bachmann, A. Bressan, M. Capeáns, M. Deutel, S. Kappler, B. Ketzer, A. Polouektov, L. Ropelewski, F. Sauli, E. Schulte, L. Shekhtman, A. Sokolov," Discharge studies and prevention in the gas electron multiplier (GEM)" *Nucl. Instrum. Methods Phys. Res.* A, vol.479, pp. 294-308, 2002.

[72] The TOTEM Collaboration, "The TOTEM Experiment at the CERN Large Hadron Collider", *Journal of Instrumentation*, JINST 3 S08007, 2008.

[73] B. Ketzer, "Micropattern gaseous detectors in the COMPASS tracker ",*Nucl. Instrum. Methods Phys. Res.* A, vol.494 pp. 142-147, 2002.

[74] F. A. F. Fraga, L. M. S. Margato, S. T. G. Fetal, M. M. F. R. Fraga, R. Ferreira Marques and A. J. P. L. Policarpo, "Luminescence and imaging with gas electron multipliers", *Nucl. Instrum. Methods Phys. Res.* A, vol.513, pp. 379-387, 2003.

[75] F. Salvat, J. M. Fernández-Varea, J. Sempau, "PENELOPE-2006: A Code System for Monte Carlo Simulation of Electron and Photon Transport", Workshop Proceedings Barcelona, Spain , July 2006, ISBN 92-64-02301-1

[76] R. Kreuger, C.W.E. van Eijk, F.A. Fraga, M.M. Fraga, S.T.G. Fetal, R.W. Hollander, L.M.S. Margato, T.L. van Vuure, "Performance of high pressure Xe/TMA in GEMs for neutron and X-ray detection" ", *IEEE Trans. Nucl. Sci Conf. Record*, vol 1, pp. 457-461, 2001.

[77] P. Jeanneret, J. Busto, J.-L. Vuilleumier, A. Geiser, V. Zacek, H. Keppner, R. de Oliveira, "Performance of a new Micromegas detector, with woven wire mesh, in CF4" *Nucl. Instrum. Methods Phys. Res.* A, vol. 500, pp. 133-143, 2003

[78] J. F. C. A. Veloso, J. M. F. dos Santos, and C. A. N. Conde," A proposed new microstructure for gas radiation detectors: The microhole and strip plate." *Rev. Sci. Instrum.* 71 p. 2371-2376, 2000.

[79] J.M. Maia, J. F. C. A. Veloso, J. M. F. dos Santos, A. Breskin, R. Chechik and D. Mörmann "Advances in the Micro-Hole & Strip Plate gaseous", *Nucl. Instrum. Methods Phys. Res.* A, vol. 504, pp. 364-368, 2003.

[80] H. Natal da Luz, J.A. Mir, J. F. C. A. Veloso, J. M. F. dos Santos, N.J. Rhodes, E.M. Schooneveld, " Micro-Hole and Strip Plate (MHSP) operation in CF4", *Nucl. Instrum. Methods Phys. Res.* A, vol. 580, pp. 286-288, 2007.

[81] *M. Nakhostin,"Performance of a low-pressure Micromegas-like gaseous detector",* Nucl. Instrum. Methods Phys. Res. *A, vol. 598, pp. 496-500, 2009.*

[82] A. Sharma, "Properties of some gas mixtures used in tracking detectors", ICFA 16,1998.

[83] I. Bronic, "The w-Values for Photons and Electrons in Mixtures ofArgon and Alkanes", Radiation Research, vol. 125, pp. 1-5, 1991.

[84] S. Bachmann, A. Bressan, L. Ropelewski, F. Sauli, A. Sharma and D. Mörmann, "Charge amplification and transfer processes in the gas electron multiplier", Technical Report CERN-EP 99–48, 1999.

[85] J.E. Bateman, "Gain stabilisation in proportional counters", Rutherford Appleton Laboratory Report , RAL-TR-98-044 (1998).

[86] J.A. Crowther, ―Ions, Electrons and Ionising Radiation‖, Edward Arnold, London (1959).

[87] J. V'vra, "Photon detectors", Nucl. Instr. and Meth. A 371 (1996) 33

[88] A. Delbart, R.De Oliveira. Derré, Y. Giomataris, F. Jeanneau, Y. Papadopoulos and Ph. Rebourgeard**l.,"**New developments of Micromegas detector", Nucl. Instr. and Meth. A461 (2001) 84.

[89] Derré, et al., ―Fast signals and single electron detection with a MICROMEGAS photodetector, Nucl. Instr. and Meth. A 449 (2000) 314.

[90] J. Va'vra, et al., ―Single electron Amplification in ―Single-MCP+Micromegas+Pads‖ Detector‖, IEEE Trans. Nucl. Sci. 51 (2004) 2262.

[91] F. Sauli, S. Kappler, L. Ropelewski, "Electron collection and ion feedback in GEM-based detectors", IEEE Trans. Nucl. Sci, vol.50, pp 803-808, 2003.